UNIVERSITY OF CALIFORNIA
IRVINE

Measurement of decay parameters of the $\psi'(2^3S_1)$ state of charmonium

DISSERTATION

submitted in partial satisfaction of the requirements for the degree of

DOCTOR OF PHILOSOPHY

in Physics

by

Giovanni Maria Lasio

Dissertation Comittee:
Professor Mark A. Mandelkern, Chair
Professor Jonas Schultz
Professor Dennis Silverman

2003

© 2003 Giovanni Maria Lasio
All rights reserved.

The dissertation of Giovanni Maria Lasio is approved,
and is acceptable in quality and form
for publication on microfilm:

_____

_____

_____

Committee Chair

University of California, Irvine

2003

DEDICATION

Alla memoria di Anna

Contents

List of Figures

List of Tables

Acknowledgements

I would like to thank my advisors, Professor Mark Mandelkern and Professor Jonas Schultz, for their guidance and support during all the time necessary to complete this work. I would also like to thank the members of the E835 collaboration for the realization of a successful experiment, and for creating a productive yet enjoyable working environment at Fermilab. In particular I would like to mention Dr. Keith Gollwitzer and Dr. Giorgos Zioulas; their guidance has been fundamental during my work at Fermilab. I would like to thank also the professors and researchers of the Torino group, in particular Dr. Flavio Marchetto and Dr. Nadia Pastrone for their numerous suggestions during data taking. The time I spent at Fermilab would have not been the same without the professionality and the friendship of many people, among whom I would like to mention Gabriele Garzoglio, Paolo Rumerio, Michelle Stancari, Wander Baldini, Giulio Stancari, Matteo Negrini, Margherita Obertino, Gigi Cibinetto. While at U.C.I. I enjoyed meeting and spending time with numerous people. Many of them also became dear friends; it would take a whole page to mention them all, but I would like to remeber here Jeff, Francesca, Antonello, Silvia and Riccardo. During my last year at U.C.I my dear Jelena has been an unfailing and loving support through mood swings, sleepless nights, bad meals and countless other sources of discomfort. Many apologies to the people I missed. I would like to thank Katjia, an essential source of encouragement and good vibes from Italy; your presence made a big difference. Last, my biggest thanks goes to my family. Without your support this work would have never been possible; this thesis is dedicated to you and to the memory of Anna. Il ringraziamento più grande va alla mia famiglia. Senza

di voi questo lavoro non sarebbe mai stato possibile. Ma e Pa, nonostante la distanza che ci separa siete riusciti a farmi sentire la vostra presenza e il vostro sostegno, come anche Rainer, David, Edi, Gunter, e Anna. Oltre che alla memoria di Anna, questo lavoro è dedicato a tutti voi.

Curriculum Vitae

1995	Laurea Degree in Physics University of Torino, Italy
1997–1998	Teaching Assistant, Department of Physics, University of California, Irvine
1998–2003	Research Assistant, Department of Physics, University of California, Irvine
2000	M.Sc. in Physics, University of California, Irvine
2003	Ph.D. in Physics, University of California, Irvine Dissertation: Measurement of decay parameters of the $\psi'(2^3S_1)$ state of charmonium
	Professor Mark Mandelkern, Chair Professor Jonas Schultz

Publications

M. Ambrogiani et al., Measurements of the magnetic form factor of the proton in the timelike region at large momentum transfer, Phys. Rev. D60, 032002 (1999).

M. Ambrogiani et al., Study of the χ_{c0} $(1^3\mathrm{P}_0)$ state of charmonium formed in $\overline{p}p$ annihilations, Phys. Rev. Lett. 83, 2902 (1999).

M. Ambrogiani et al., Measurement of the branching ratios $\psi' \to e^+e^-$, $\psi' \to J/\psi\pi^0\pi^0$ and $\psi' \to J/\psi\eta$, Phys. Rev. D 62, 032004 (2000).

M. Ambrogiani et al., Study of the $\gamma\gamma$ decays of the χ_2 and χ_0 charmonium resonances, Phys. Rev. D 62, 052002 (2000).

M. Ambrogiani et al., Search for the η_c' charmonium resonance, Phys. Rev. D64, 052003 (2001).

C. Patrignani et al., E835 at Fnal: charmonium spectroscopy in proton-antiproton annihilations, Nucl.Phys. A692, 308 (2001).

S. Bagnasco et al., New measurements of the resonance parameters of the χ_0 state of charmonium, Phys. Lett. B533, 237 (2002).

M. Ambrogiani et al., Measurement of the resonance parameters of the charmonium ground state $\eta_c(1^1S_0)$, Phys. Lett. 566, 45 (2003).

M. Andreotti et al., Interference study of the $\chi_0(1^3P_0)$ in the reaction $\overline{p}p \to \pi^0\pi^0$, accepted for publication Phys. Rev. Lett. (2003).

Abstract of the Dissertation

Measurement of decay parameters of the $\psi'(2^3S_1)$ state of charmonium

by

Giovanni Maria Lasio

Doctor of Philosophy in Physics

University of California, Irvine, 2003

Professor Mark A. Mandelkern, Chair

Fermilab experiment E835 studied the $\psi'(2^3S_1)$ charmonium state formed in $\overline{p}p$ annihilations. The E835 detector is a non-magnetic spectrometer designed to detect charmonium decays with a high invariant mass e^+e^- pair in the final state. This resulted in a new measurement of the branching ratios of the decays: $\psi' \to e^+e^-$, $\psi' \to J/\psi\pi^+\pi^-$, $\psi' \to J/\psi\pi^0\pi^0$, $\psi' \to J/\psi\eta$. The number of events counted in each channel was normalized to the number of inclusive events $\psi' \to J/\psi X$. We found: $B(\psi' \to e^+e^-) = (6.3\pm0.1\pm0.4)\times10^{-3}$, $B(\psi' \to J/\psi\pi^+\pi^-) = (30.3\pm0.5\pm1.8)\times10^{-2}$, $B(\psi' \to J/\psi\pi^0\pi^0) = (17.1\pm0.5\pm1.1)\times10^{-2}$, $B(\psi' \to J/\psi\eta) = (2.7\pm0.2\pm0.3)\times10^{-2}$. We studied the angular distribution of the decay $\overline{p}p \to \psi' \to e^+e^-$ with a fit to the theoretical distribution $1 + \lambda(\psi')\cos\theta_e^*$. The parameter $\lambda(\psi')$ is characteristic of ψ' formed in $\overline{p}p$ annihilation, and was found to be 0.71 ± 0.23.

Chapter 1

Charm quark and charmonium

This chapter presents an overview of the history of the charm quark and the place it occupies in QCD theory. A summary of the theoretical tools used in studying the bound state of a charm and an anti-charm quark ($c\overline{c}$, called *charmonium*) is presented. We then describe some theoretical frameworks for the description of charmonium transitions.

1.1 The charm quark

Before 1974 the quark model, despite having supporting evidence from deep inelastic scattering experiments regarding the proton structure and providing an explanation for the structure of baryon and meson multiplets, was seen by many physicists as not entirely satisfying. The main reasons were that the quark model appeared to violate Pauli's principle, and that free quarks were not observed. The conflict with Pauli's principle is well described by the case of Δ^{++}; the quark model describes this resonance with a valence quark structure (of $l = 0$) $u \uparrow u \uparrow u \uparrow$. Unless color is introduced, this implies a symmetric state of identical fermions; to make $u\uparrow\ u\uparrow\ u\uparrow$ antisymmetric it is necessary that each quark flavor exist in at least 3 (color) states;

more than 3 colors would imply the existence of more than one type of proton, which is not observed. The quark-parton model suggested that the hadron constituents were bound by an interaction whose strength depends on their energy [48]. This energy dependent coupling among hadron constituents was described in more detail by QCD: the strong interaction would confine the quarks inescapably inside the hadron at low energy (*infrared slavery*), while tending to negligible values at high energy (*asymptotic freedom*).

The discovery of the J/ψ was of fundamental importance for QCD, since within this theory it was possible to explain the nature of this new meson. The J was first observed in the summer of 1974 at Brookhaven, by a group led by Samuel Ting. Shortly after, another group at SLAC led by B. Richter announced the discovery of the same particle, calling it ψ, independently from the Brookhaven collaboration. The two groups published their results simultaneously [25][24]. The most unusual characteristics of this new particle were its large mass 3.1 GeV[1] and its long lifetime, of the order of 10^{-20} s, considerably longer than for other hadron resonances. The discovery of another narrow resonance with higher mass (~ 3.7 GeV) than the J/ψ was announced by the SLAC group shortly after [22]. Before 1974 the experimental evidence for fundamental fermions consisted of two doublets of leptons,

$$\begin{pmatrix} e \\ \nu_e \end{pmatrix} \begin{pmatrix} \mu \\ \nu_\mu \end{pmatrix}$$

and three quark flavors (u, d, s). The quark model suggested that the J/ψ was a bound state of a fourth quark called *charm*, or c, and its antiquark $\overline{c}$ [36][15]. Another argument supporting the idea of a fourth quark flavor was the Glashow-Iliopoulos-Maiani (GIM) model [56]. The GIM mechanism leads to the suppression of strangeness changing neutral currents at the first order in the S matrix of the weak interactions,

[1]We use natural units throughout this document, so that $\hbar = c = 1$.

such as in the unobserved decay modes $K_L \to l^+l^-$, $K^+ \to l^+l^-\pi^+$; the GIM model required the c quark to be the $SU(2)$ partner of the Cabibbo-rotated strange quark $s_c = s\cos\theta_c - d\sin\theta_c$ in the weak isospin doublets

$$\begin{pmatrix} u \\ s\sin\theta_c + d\cos\theta_c \end{pmatrix}\begin{pmatrix} c \\ s\cos\theta_c - d\sin\theta_c \end{pmatrix}$$

Moreover, the existence of the c quark implied that there should be a number of new mesons and baryons carrying *charm*, and indeed Λ_c^+, the first baryon carrying "naked" *charm* was observed in 1975 [10].

The bound state of a nonrelativistic heavy quark and antiquark of the same flavor, called *quarkonium*, is a particularly good testing ground for QCD. The large mass of the c quark ($m_c \sim 1.5$ GeV) sets a mass scale high enough (and correspondingly implies a bound state size small enough) to approach the asymptotically free regime. Bound states of the *charm* quark and its antiquark, called *charmonium*, are the first bound systems of quarks to which QCD applies, even approximately, as a perturbative theory. Charmonium provides a Coulomb-like spectrum in a system simple enough to have deserved the denomination of "hydrogen atom of the strong interaction". For this reason we will present a summary of the basic features of QCD, in the following section.

1.2 QCD

Experiments on deep inelastic scattering in the late 1960s showed that quarks might be more than just the indication of a quantum number for the flavor $SU(3)$ symmetry. At that time hadron-hadron collisions were thought to be too complicated to be useful to understand strong interactions, especially when perturbative field theory tools were to be used. However, deep inelastic lepton-nucleon scattering

experiments showed an interesting set of properties:

- there were more backward scattered particles than expected assuming a uniform mass distribution in the nucleon. This implies the presence of point-like particles, or *partons*, within the nucleon.

- Through the study of parton structure functions it was determined that partons have spin 1/2 and point-like magnetic moments; weak and electromagnetic cross sections from lepton-nucleon scattering experiments also suggested that partons have *fractional charge*.

- Partons are quasi-free inside the nucleon, as shown by high energy lepton probes. This leads to the phenomenon described as *Bjorken scaling* [2].

The parton model [41] explained Bjorken scaling as the incoherent elastic scattering of charged leptons from partons through exchange of a virtual photon. Identifying the partons with the quarks, the *quark-parton* model resulted: the model was useful in understanding the observations in deep inelastic scattering, but did not provide an explanation for 55% of the nucleon mass.

QCD, which was formulated in the early '70s [48][87], provides the most comprehensive framework for strong interactions. It is based on two fundamental premises:

- to describe strong interactions we need to use a local gauge theory, and

- the color quantum number is representative of a $SU(3)$ symmetry, distinct from the global flavor symmetry.

The bosons of the strong interaction are represented by 8 gluons, which are color charged, therefore they can interact with each other; being the gauge bosons of a

Yang-Mills field, the gluons are massless (mass terms would spoil the gauge invariance if explicitly included in the Lagrangian). The QCD Lagrangian density is:

$$\mathcal{L} = \sum_{f=1}^{N} \overline{\psi}_f (i\gamma^\mu D_\mu - m_f)\psi_f - \frac{1}{4} F^j_{\mu\nu} F_j^{\mu\nu} \tag{1.1}$$

$$D_\mu = \partial_\mu + \frac{i}{2} g \lambda_l A^l_\mu \tag{1.2}$$

$$F^j_{\mu\nu} = \partial_\mu A^j_\nu - \partial_\nu A^j_\mu - g f_{jkl} A^k_\mu A^l_\nu \tag{1.3}$$

where f is the flavor index, N is the number of flavors, g the gauge coupling constant, A^l_μ is the space-time component of the l^{th} gluon vector potential, λ_l are the 8 Gell-Mann matrices and f_{jkl} are the $SU(3)$ structure constants. The QCD Lagrangian 1.1 has the following symmetry properties [76]:

- it is invariant under P, C and T
- it is invariant for global phase rotations $\psi_f \rightarrow e^{i\theta_f}\psi_f$, therefore implying conservation laws for the quantum number associated to the flavor f
- if the difference in quark masses can be ignored, then 1.1 is invariant under $\psi_j = U_{jk}\psi_k$, where jk are flavor indices and U_{jk} is a unitary matrix; for the (u, d, s) quarks this implies approximate flavor $SU(3)$ symmetry, and isospin invariance for the lightest quarks (u, d)
- cosidering (u, d, s) massless, the Lagrangian 1.1 is invariant under the product of global flavor $SU(3)$ rotations on the fields:

$$\begin{aligned} q_L &\equiv \frac{1}{2}(1 - \gamma_5)q \\ q_R &\equiv \frac{1}{2}(1 + \gamma_5)q \end{aligned}$$

This symmetry under $SU(3)_L \times SU(3)_R$ is called *chiral symmetry* and it is explicitly broken by current quark mass terms such as $m_u\overline{u}u + m_d\overline{d}d + m_s\overline{s}s$. The *current* (i.e. bare quark) masses appearing in the Lagrangian can be deduced from the chiral symmetry breaking term by computing the ratios [61][42]:

$$\frac{m_d}{m_u} = \frac{m^2_{K^0} - m^2_{K^+} + m^2_{\pi^+}}{2m^2_{\pi^0} + m^2_{K^+} - m^2_{K^0} - m^2_{\pi^+}} \simeq 1.8 \tag{1.4}$$

$$\frac{m_s}{m_d} = \frac{m^2_{K^0} + m^2_{K^+} - m^2_{\pi^+}}{m^2_{K^0} - m^2_{K^+} - m^2_{\pi^+}} \simeq 20 \tag{1.5}$$

Combining 1.4 and 1.5 with an estimate of m_s obtained from the $\Lambda - N$ mass difference one gets [42]:

$$m_u \simeq 4.2 \text{ MeV} \quad m_d \simeq 7.5 \text{ MeV} \quad m_s \simeq 150 \text{ MeV}$$

The quark *constituent masses* are significantly higher than the current masses, due to the interactions taking place inside the hadron. However, the relation between current and constituent masses requires a solution with non perturbative methods (lattice calculations, QCD sum rules) [47], which is presently not available. The Feynman rules for QCD are similar to those of electroweak theory. They are constructed with standard methods from the Lagrangian density 1.1 and they can be found in the literature [7].

Two distinctive features of QCD are *asymptotic freedom* and *confinement*. The running coupling constant in QCD is [47]:

$$\alpha_s(q^2) = \frac{12\pi}{(33 - 2N_f(q^2))ln(-q^2/\Lambda^2)} \tag{1.6}$$

where q is the momentum transfer, N_f the number of accessible (i.e. with $m^2 < |q^2|$) quark flavors and Λ is a scale parameter determined experimentally. Λ also depends on the renormalization scheme in use; it can be seen that 1.6 tends to zero for large q^2; this asymptotic behavior helps to qualitatively understand Bjorken scaling and provides

a justification for the quark-parton model. This is a fundamentally different behavior from the one we see in the QED coupling constant, and it is explained by the fact that gluons interact with each other, and gluon loops dominate over quark loops (there are 8 gluons and only 6 flavors). At small momentum transfer (or large distance) α_s becomes very large and perturbation theory cannot be applied. Nonperturbative models suggest also that at large distances the coupling becomes so strong that it is not possible to separate color sources; this behavior, also suggested by 1.6, is known as color confinement. Λ defines the length at which the strong interaction cannot be treated perturbatively; the renormalization scheme commonly used, referred to as *modified minimal subtraction* [14], defines $\Lambda = \Lambda_{\overline{MS}}^{(N_f)}$ as a function of the number of quark flavors included in the calculations; for $N_f = 4$ an average of the experimental determinations of Λ gives $\Lambda_{\overline{MS}}^{(4)} = 200^{+150}_{-80}$ MeV [17] (which corresponds to $\alpha_s(q = 1.55$ GeV$) \simeq 0.37$).

1.3 Charmonium

The first bound state of a particle and its antiparticle to be studied experimentally and theoretically was positronium, an electron bound to a positron. Stringent QED tests were performed with this simple system, so the idea of being able to test QCD by using quarkonium was particularly promising. Usually a distinction is made between light quarkonium ($u\overline{u}$,$d\overline{d}$, $s\overline{s}$) and heavy quarkonium ($c\overline{c}$, $b\overline{b}$ and $t\overline{t}$).

Heavy quarkonium appears to be particularly interesting because it is expected [1] that a quark and its antiquark should form a bound state if its mass is higher than the QCD scale Λ. Sufficiently heavy quarks are also expected to behave non-relativistically, in quarkonium. This implies that solving a Schrödinger equation with an effective potential could give us a fairly accurate description of heavy quarko-

nium. In reality the only system for which a non relativistic treatment is completely adequate is bottomonium[2]. However, the non relativistic treatment is justified for charmonium as well: using the virial theorem $2 < T >=< \vec{r} \cdot \nabla V(\vec{r}) >$[3] we can show that $< v^2 > \sim 0.15$. The simplest idea is to use a Coulomb-like potential plus a linear term (for quark confinement):

$$V(r) \sim -\frac{4}{3}\frac{\alpha_s(r)}{r} \quad , \quad r \ll 1/\Lambda$$
$$V(r) \sim kr \quad , \quad r \gg 1/\Lambda$$

where $\alpha_s(r)$ is the QCD running coupling constant and k is a constant. Let us assume that the linear term dominates the behavior of the potential at an (average) distance r; then $2 < T >=< V >$, and $E_c =< T > + < V >= 3 < T >$, where E_c is a characteristic energy analogous to the binding energy in atoms[4]. From the non relativistic expression for the kinetic energy follows $\mid E_c \mid = 3m_c < v^2 >$. Assuming we can estimate the characteristic energy of the J/ψ as

$$E_c \;=\; M(J/\psi) - M(\psi(3770)) \;=\; -673 \text{ MeV}$$

we obtain $< v^2 > \simeq 0.15$, which appears to justify a non relativistic approach. It is evident though that the above reasoning is already based on a non relativistic picture; moreover, the result depends on the potential chosen. Quark potential models [77] suggest that $< v^2 > \sim 0.3$; even in this case though, such a model can describe well

---

[2]The large *top* mass ($m_t \sim 175$ GeV) implies that the decay time is very short, therefore t quarks cannot bind to form hadrons and they decay as free particles. Moreover, the toponium width ($\Gamma_{t\bar{t}} \sim 3$ GeV) would be larger than the splitting between $1S$ and $2S$ states expected from the perturbative QCD potential, merging all *top* resonances and showing as a broad excitation curve in the cross section.

[3]$< \cdots >$ is the expectation value, $< T >\equiv m_c < v^2 >$ is the kinetic energy and $m_c \sim 1.5$ GeV the charm quark mass

[4]Isolated quarks are not observed; we cannot define a binding energy for the $\overline{c}c$ system.

charmonium spectroscopy and decays. We can also observe that the scale of the separation between radial excitations and orbital angular momentum excitations is of the order of $m_c v^2$, the Compton wavelength $1/m_c$ defines the spatial scale for the annihilation processes and the size of the bound state is given by $1/m_c v$ and even for charmonium these energy scales are well separated: $m_c^2 \gg (m_c v)^2 \gg (m_c v^2)^2$. This justifies using a non relativistic approach.

1.3.1 Nonrelativistic potential models

Non relativistic quark models first appeared with a Hamiltonian of the form [82]:

$$H = \sum_i \left(\frac{\vec{p}_i^2}{2m_i} + m_i \right) + \sum_{i>k} \left(\alpha q_i q_k + \frac{1}{4} < \lambda_i \cdot \lambda_j > \alpha_s \right) S_{ij} + V_{conf} \tag{1.7}$$

where α_s and α are respectively the strong coupling constant and the fine structure constant; q_i, m_i and $\vec{p}_i$ are electric charge, mass and momentum of the i^{th} quark,

$$\frac{1}{4} < \lambda_i \cdot \lambda_j > = \begin{cases} -\frac{4}{3} & : \quad q\overline{q} \\ -\frac{2}{3} & : \quad qq^5 \end{cases} \tag{1.8}$$

is the color factor (λ_i being the Gell-Mann matrices), V_{conf} is the confining potential and the spin dependent terms are described by

$$\begin{aligned} S_{ij} = \; & \frac{1}{r} - \frac{1}{2m_i m_j} \left(\frac{\vec{p}_i \cdot \vec{p}_j}{r} + \frac{\vec{r} \cdot (\vec{r} \cdot \vec{p}_i) \vec{p}_i}{r^3} \right) - \frac{\pi}{2} \delta^3(\vec{r}) \left(\frac{1}{m_i^2} + \frac{1}{m_j^2} + \frac{16 \vec{s}_i \cdot \vec{s}_j}{3 m_i m_j} \right) \\ & - \frac{1}{2r^3} \left[\frac{1}{m_i^2} \vec{r} \times \vec{p}_i \cdot \vec{s}_i - \frac{1}{m_j^2} \vec{r} \times \vec{p}_j \cdot \vec{s}_j \right. \\ & \left. \frac{1}{m_i m_j} \left(2\vec{r} \times \vec{p}_i \cdot \vec{s}_j - 2\vec{r} \times \vec{p}_j \cdot \vec{s}_i - 2\vec{s}_i \cdot \vec{s}_j + 6 \frac{(\vec{s}_i \cdot \vec{r})(\vec{s}_j \cdot \vec{r})}{r^2} \right) \right] \end{aligned} \tag{1.9}$$

where $\vec{r} = \vec{r}_i - \vec{r}_j$ and $\vec{s}_i$ is the quark spin operator. In the literature 1.9 is known as the *Fermi-Breit interaction*. The term within square brackets represents spin-orbit and tensor interactions; it does not contribute for $q\overline{q}$ states with $L = 0$. If $L = 1, 2, \ldots$

[5] For qq in a color singlet baryon qqq.

$\delta^3(\vec{r})$ reduces the contribution of its term to zero. In practice only selected terms in 1.9 are used for calculations, depending on what one wants to study; the spin-orbit interaction terms are kept for fine structure investigation, i.e. ${}^3P_J$ level spacings. The spin-spin terms are used for hyperfine structure calculations, as in the spacing ${}^3P - {}^1P$. Assuming that the long range potential has only radial dependence, the strong interaction part in 1.7 can be written (for a meson) as:

$$V(r) = -\frac{4}{3}\frac{\alpha_s}{r} + V_{conf}(r) + V_\sigma \tag{1.10}$$

where V_σ contains the remaining terms. String models [88] and lattice gauge field theory arguments [89] suggest $V_{conf} \sim \kappa r$. In the string model κ is called *string tension* and it is possible to show that κ is related to the Regge slope. In general there are other possible choices for V_{conf}, but the one above is the most easily justifiable. A potential often used to describe the spin-independent features of the charmonium spectrum is the *Cornell potential*, which has the form 1.10 where the confining potential is κr and $V_\sigma = 0$. Once the potential $V(r)$ is chosen, the quarkonium spectrum can be calculated by solving the Schrödinger equation:

$$-\frac{1}{m_c}\nabla^2\psi(\vec{r}) + V(r)\psi(\vec{r}) = E\psi(\vec{r}) \tag{1.11}$$

1.3.2 Energy spectrum

The charmonium spectrum is usually described with the spectroscopic notation $n^{2S+1}L_J$, where $n = 1, 2, 3, \ldots$ is the principal quantum number, $L = S, P, D, \ldots$ the orbital angular momentum, S the total spin and J the total angular momentum. Parity and charge conjugation parity are given by:

$$P = (-1)^{L+1} \quad , \; C = (-1)^{L+S} \tag{1.12}$$

Figure 1.1 shows the charmonium spectrum. The states with $J^{PC} = 1^{--}$ have been studied mostly with $e^+e^- \to \gamma^* \to \overline{c}c$. Other levels are reached either through dipole transitions from the 1^{--} states (as indicated by the green and blue arrows in fig. 1.1) or through direct formation in $\overline{p}p$ annihilations. The $\psi(3770)$ and other states that were not studied by our experiment are not included in fig. 1.1. The levels $^1D_2$ and $^3D_2$ are still unobserved; they are expected to be narrow, as they are thought to lie under the $D\overline{D}^*$ threshold. Since $^{1,3}D_2$ have $J^P = 2^-$ they cannot decay to $D\overline{D}$, for which $P = (-1)^J$. Under the "open charm" threshold one expects to observe total widths between 10 MeV, typical for 2 gluon intermediate states, to less than 100 keV for transitions with 3 intermediate gluons (as it is the case for the J/ψ).

1.3.3 The Okubo-Zweig-Iizuka rule and the J/ψ

We mentioned in 1.1 the unusually narrow width of the J/ψ. This occurrence can be qualitatively explained with a phenomenological selection rule that was postulated for the decay of vector mesons [68][90][55]. An example is given by the decays of the $\phi(1020)$. This meson has a width of 4.4 MeV; phase space strongly favors the decay $\phi \to 3\pi$, but this channel is highly suppressed with respect to $\phi \to K^+K^-$. To account for this observation one can assume that *connected quark diagrams are favored with respect to disconnected diagrams.* Analogously to the ϕ decay, J/ψ decays could proceed as shown in fig. 1.2. We expect that the favored decay would be into two charmed mesons, as in fig. 1.2*a*. However the energy threshold for the decay into $\overline{D}^0D^0$ is higher than the J/ψ rest energy; therefore the only strong decay allowed is through an OZI-suppressed process such as the one in fig. 1.2*b*. QCD can help us qualitatively understand this suppression mechanism. In a diagram like 1.2*b* the initial and the final states can be connected only through gluon exchange. Single

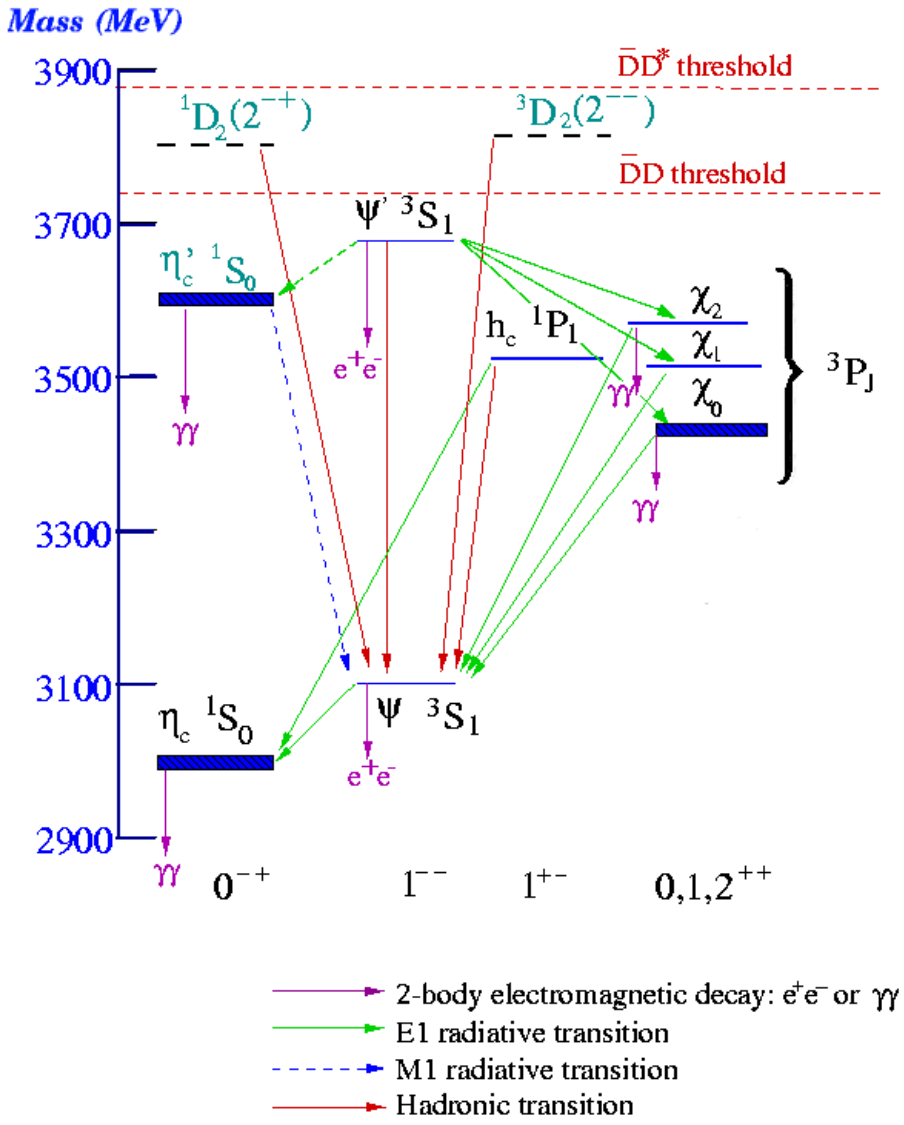

Figure 1.1: The spectrum of charmonium.

gluon exchange is ruled out, because of color conservation. Two gluons could lead to a color singlet, but a $J^{PC} = 1^{--}$ state such as the J/ψ cannot couple to two gluons, which must be even under charge conjugation. So, in the case of the J/ψ the simplest case involves the exchange of three gluons. These three gluons are hard, as they carry all the energy of the $\overline{c}c$ pair. Perturbative QCD should be approximatively valid to describe the $\overline{c}c$-3 gluon emission, so the emission rate for three hard gluons would be $\simeq (\alpha_s(q^2))^3$. If $\alpha_s(q^2)$ is small enough, the contribution of the OZI-suppressed diagrams to the J/ψ decay is small.

1.4 Charmonium transitions

The charmonium decay mechanisms include annihilation processes, radiative transitions and hadronic transitions. In the following we will talk about decays that occur below the open charm threshold.

1.4.1 Resonance cross section

The cross section for the formation and decay of a resonance R in the process $a + b \to R \to f$ can be expressed by means of the well known Breit-Wigner formula, as follows:

$$\sigma_R(E) = \frac{2J+1}{(2S_a+1)(2S_b+1)} \frac{\pi}{k^2} \frac{B_{in} B_{out} \Gamma_R^2}{(E - E_R)^2 + \frac{\Gamma_R^2}{4}} \tag{1.13}$$

where:

- J, M_R are resonance spin and mass
- $\Gamma_R = \sum_f \Gamma_f$ is the total width

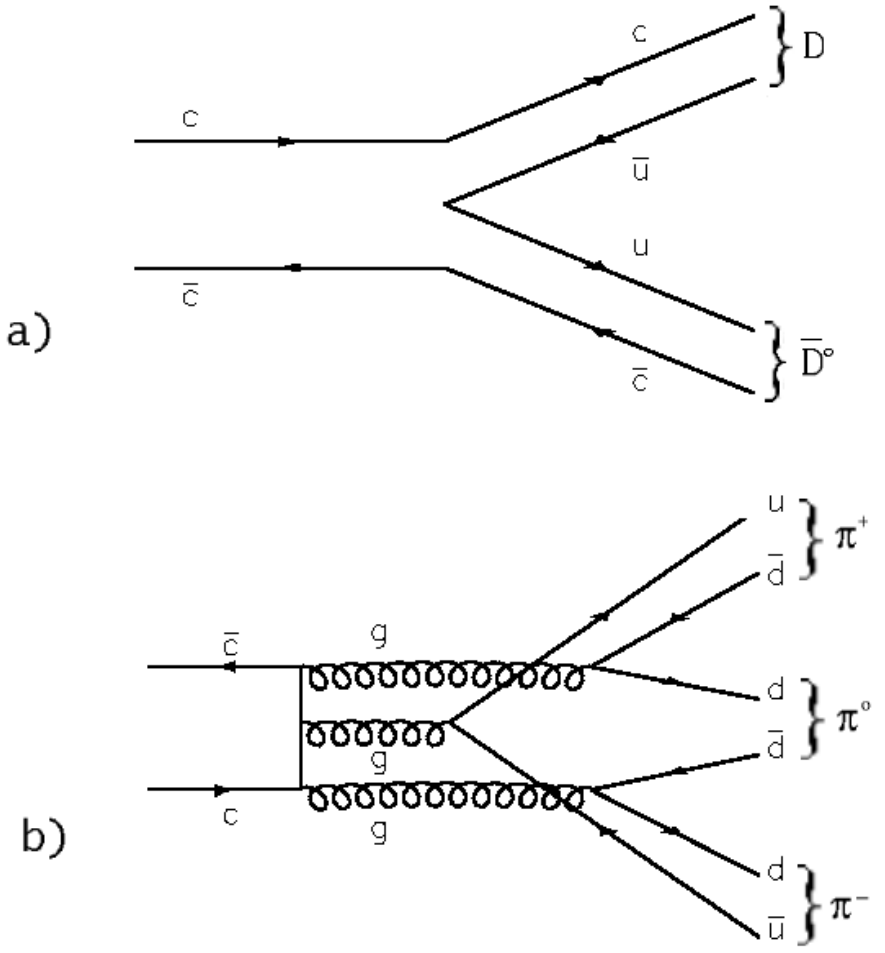

Figure 1.2: Strong decay modes of charmonium; in the J/ψ decay diagram a) is OZI allowed but kinematically forbidden, while b) is kinematically possible, but OZI suppressed.

- k is the momentum in the CM frame:

$$k^2 = \frac{M_R^2 - 4m_p^2}{4} \tag{1.14}$$

- $S_{a,b}$ are the spins of the incoming particles
- $B_{in}B_{out}$ is the product of the formation and decay branching ratios
- E_R is the resonance rest energy and E the total CM energy

1.4.2 Annihilation transitions

The state of a charged nonrelativistic lepton moving with its antiparticle can help us build a procedure for computing annihilation rates in charmonium. Let us look at the annihilation into two γ. Due to charge conjugation invariance ${}^3S_1$ states do not decay to 2 photons. We consider the bound state ${}^1S_0$. For momentum eigenstates the amplitude is:

$$\mathcal{M} = -ie^2\overline{v}(\lambda_+, \vec{p}_+)\left[\not{\varepsilon}_2^* \frac{i}{\not{p}_- - \not{q}_1 - m}\not{\varepsilon}_1^* + \not{\varepsilon}_1^* \frac{i}{\not{p}_- - \not{q}_2 - m}\not{\varepsilon}_2^*\right] u(\lambda_-, \vec{p}_-) \tag{1.15}$$

where e,m, $\vec{p}_\pm$ are lepton charge, mass and momenta, $\lambda_\pm$ the initial state spins, $q_{1,2}$ the momenta of the two photons, $\varepsilon_{1,2}$ the photon polarizations. Let us choose the transverse gauge $\varepsilon_1^* \cdot p_- = \varepsilon_2^* \cdot p_- = 0$ in the lepton rest frame. The squared amplitude for a ${}^1S_0$ transition can be calculated summing over $\lambda_\pm$:

$$\sum_{\pm} |\mathcal{M}|^2 = \frac{e^4}{2m^2}\left[2 + \frac{\omega_1}{\omega_2} + \frac{\omega_2}{\omega_1} - 4(\vec{\varepsilon}_1^* \cdot \vec{\varepsilon}_2^*)^2\right] \tag{1.16}$$

where $\omega_{1,2}$ are the photon energies in the lepton rest frame. The details of the calculation can be found in the literature [46]. In the nonrelativistic limit the photons have

energies $\omega_{1,2} \to m$ and are emitted back-to-back, and the differential cross section is:

$$\frac{d\sigma_{nr}}{d\Omega} = \frac{\alpha^2}{2m^2 v_+}(1 - (\vec{\varepsilon}_1^* \cdot \vec{\varepsilon}_2^*)^2) \tag{1.17}$$

The sum on back-to-back photon polarization gives [46]:

$$\sum_{\varsigma_{1,2}}(1 - (\vec{\varepsilon}_1^* \cdot \vec{\varepsilon}_2^*)^2) = 2 \tag{1.18}$$

Integrating over the solid angle 4π the spin averaged total cross section is found to be [46]:

$$\overline{\sigma}_{nr} = \frac{1}{2}\int d\Omega \frac{d\overline{\sigma}_{nr}}{d\Omega} = \frac{\alpha^2 \pi}{v_+ m^2} \tag{1.19}$$

Equation 1.19 represents the transition rate per incident flux of antileptons, so $v_+\overline{\sigma}_{nr}$ is the transition rate for a density of one lepton per unit volume. If the wavefunction of the state is $\Psi_n(\vec{x})$ then the density is $|\Psi_n(0)|^2$, and the rate is:

$$\Gamma_{2\gamma}^{em}(^1S_0) = v_+\overline{\sigma}_{nr}|\Psi_n(0)|^2 = \frac{4\alpha^2\pi}{m^2}|\Psi_n(0)|^2 \tag{1.20}$$

The charmonium rate to 2γ can be obtained from 1.20 including a color factor of 3 and using the appropriate quark charge $e_c = +2/3$:

$$\Gamma_{2\gamma}^{em}(^1S_0) = \frac{12 e_c^4 \alpha^2 \pi}{m_q^2}|\Psi_n(0)|^2 \tag{1.21}$$

Only the spin singlet S state can annihilate into 2 photons, due to C invariance.

The procedure to determine the rate for the 2 gluon emission is similar, if the gluons are considered massless; the diagram is shown in fig. 1.3(a). The result is [78]:

$$\Gamma_{gg}(^1S_0) = \frac{8\alpha_s^2\pi}{3m_q^2}|\Psi_n(0)|^2 \tag{1.22}$$

.

Annihilation of n^3S_1 states of charmonium can occur via a single photon to a fermion-antifermion pair, as in fig. 1.3(b), or into a final state consisting of 3 gluons,

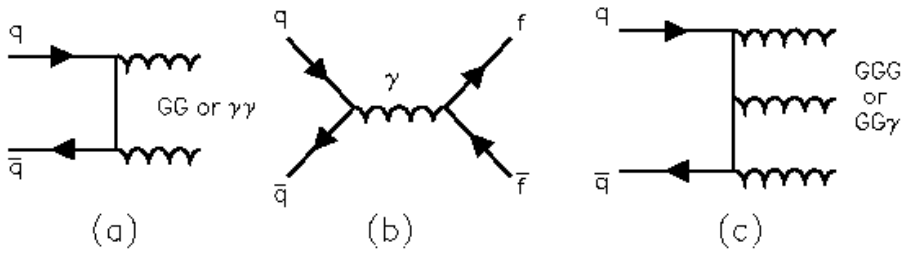

Figure 1.3: Annihilation diagrams for quarkonium.

2 gluons and a photon or 3 photons. The decay rates for each of these cases with QCD radiative corrections are reported in table 1.1; such corrections are calculated using the $\overline{MS}$ renormalization method [14], and they are evaluated at the mass of the decaying particle.

A rigorous QCD prediction for heavy quarkonium production and decay is formulated by the Bodwin-Braaten-Lepage formalism [3]. Within this framework the decay rates are expressed as an expansion with respect to α_s and v^2, v being the relative velocity of quark and antiquark.

1.4.3 Radiative transitions

Such transitions can be expressed as a multipole expansion of the electromagnetic field. The lowest allowed multipoles dominate the transition rate, as summarized in table 1.2. For charmonium these transitions, shown in fig. 1.1, are either E1 or M1. The selection rule for E1 transitions is ($\Delta S = 0$,$\Delta L = \pm 1$), for M1 transitions is ($\Delta L = 0$,$\Delta S = \pm 1$).

The decay width for an E1 transition between triplet S and P charmonium states

can be written as [60]:

$$\Gamma_{E1} = \mathcal{S}_{fi}\frac{2J_f+1}{27}k^3\alpha\frac{m_f}{m_i}\left[\frac{4}{9}|\mathcal{M}_0|^2 + \frac{8}{9}|\mathcal{M}_2|^2\right] \tag{1.23}$$

where $\mathcal{S}_{fi}$ is a statistical factor equal to 1 for triplet-triplet transitions, 3 for singlet-singlet transitions, J and m are total angular momentum and mass of the charmonium state, k is the momentum of the emitted photon and $\mathcal{M}_l$ is the radial matrix element for l-wave photon emission. The width for a M1 transition can be expressed as:

$$\Gamma_{M1} = \frac{16}{2S_i+1}k^3\alpha\frac{m_f}{m_i}|\mathcal{M}|^2 \tag{1.24}$$

Measurements have been performed of charmonium radiative transitions, including $\chi_{cJ} \to J/\psi\gamma$ and $\psi' \to \chi_{cJ}\gamma$ (E1), and $\psi', J/\psi \to \eta_c\gamma$ (M1).

E1 widths are generally overestimated by theory [64][65][69]. In particular, a rigorous E1 approximation typically overestimates the widths by a factor ~ 2. A comparison between theoretical estimates and experimental values is presented in table 1.3. The experimental width of the M1 transition $J/\psi \to \eta_c\gamma$ was overestimated by a factor of ~ 3 by nonrelativistic calculations [49]. Other recent relativistic calculations yield a better comparison with experimental results, as reported in table 1.4.

1.4.4 Hadronic transitions

Hadronic transitions in QCD are described as two step processes; in heavy quarkonium there is the emission of gluons from the quarks, then the conversion of such gluons into light hadrons. This picture can be visualized as in fig. 1.4.

Perturbative QCD is not applicable to hadronic transitions between heavy quark states, because the emitted gluons carry little energy. It has been shown that for quarkonium transitions it is possible to multipole expand the color gauge field, if

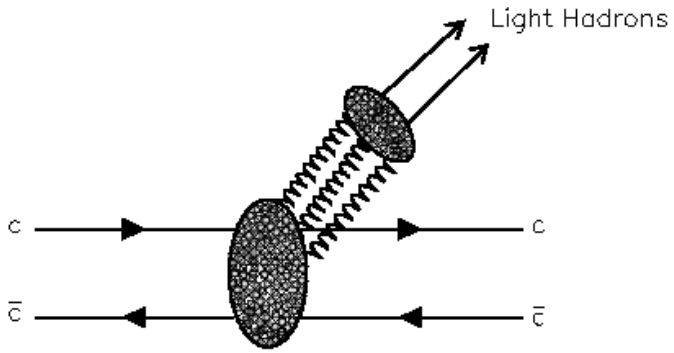

Figure 1.4: Hadronic transition in charmonium. The process consists of gluon emission by the $\overline{c}c$ pair (lower half) and successive hadronization of the gluons (upper half).

the heavy quark system is non relativistic [45]. Convergence of the multipole expansion is assured by the disparity between the heavy quark masses and the light hadrons. The multipole expansion parameter is ka, where k is the typical momentum of the emitted gluons and a is the size of the $Q\overline{Q}$ system. For a 2-gluon emission $(ka)_{c\overline{c}} \simeq 0.7$, assuming a Cornell potential; it is not clear how this estimate is related to confinement, and the relatively high value for ka does not immediately tell how well the QCD multipole expansion may work for charmonium. Several predictions for the decay rates of quarkonium using a nonrelativistic approach have been published [58][8][63][74][53][54], but in the case of charmonium the relativistic effects are non negligible.

Emission of two pions from excited $\overline{c}c$ constitutes a significant fraction of its total decay width, especially in the case of 2^3S_1, where it is $\sim$50% [27]. The $\overline{c}c$ coupling to the pions proceeds through at least two gluons. Several different approaches have been proposed, among which are effective field theories, where fitting of the gluonic operator coefficients in the multipole expansion is performed [13], and other QCD motivated models [66].

Process	Width	1^{st} order QCD correction
${}^3S_1 \to e^+e^-$	$\frac{64\pi\alpha^2}{9}\frac{\lvert\Psi(0)\rvert^2}{(2m_c)^2}$	$1-\frac{16\alpha_s}{3\pi}$
${}^3S_1 \to \gamma\gamma\gamma$	$\frac{4096\alpha^3(\pi^2-9)}{2187}\frac{\lvert\Psi(0)\rvert^2}{(2m_c)^2}$	$1-\frac{12.6\alpha_s}{\pi}$
${}^3S_1 \to ggg$	$\frac{160\alpha_s^3(\pi^2-9)}{81}\frac{\lvert\Psi(0)\rvert^2}{(2m_c)^2}$	$1+\frac{4.9\alpha_s}{\pi}$
${}^3S_1 \to gg\gamma$	$\frac{512\alpha_s^2\alpha(\pi^2-9)}{81}\frac{\lvert\Psi(0)\rvert^2}{(2m_c)^2}$	$1-\frac{0.9\alpha_s}{\pi}$
${}^3P_2 \to \gamma\gamma$	$\frac{64\alpha^2}{45}\frac{\lvert R'_{1P}(0)\rvert^2}{m_c^4}$	a [1]
${}^3P_2 \to gg$	$\frac{8\alpha_s^2}{5}\frac{\lvert R'_{1P}(0)\rvert^2}{m_c^4}$	$a(1+\frac{8.4\alpha_s}{\pi})$
${}^3P_1 \to q\overline{q}g$	$\frac{8\alpha_s^3 ln(2m_c<r>)}{9\pi}\frac{\lvert R'_{1P}(0)\rvert^2}{m_c^4}$	*not known*
${}^3P_0 \to \gamma\gamma$	$\frac{16\alpha^2}{3}\frac{\lvert R'_{1P}(0)\rvert^2}{m_c^4}$	$a(1+\frac{5.5\alpha_s}{\pi})$
${}^3P_0 \to gg$	$\frac{6\alpha_s^2\lvert R'_{1P}(0)\rvert^2}{m_c^4}$	$a(1+\frac{20.4\alpha_s}{\pi})$

Table 1.1: Lowest order width expressions and first order QCD corrections for $\overline{c}c$ decays. [1]Corrections not known for the P states; only ratios are indicated here [78].

Transition	P_iP_f	C_iC_f	Lowest allowed multipole
${}^3S_1 \leftrightarrow {}^3P_{0,1,2}$	-1	-1	E1
${}^1S_0 \leftrightarrow {}^1P_1$	-1	-1	E1
${}^3S_1 \leftrightarrow {}^1S_0$	+1	-1	M1
${}^3P_J \leftrightarrow {}^1P_1$	+1	-1	M1

Table 1.2: Lowest allowed multipole transitions between charmonium states; transitions between states with the same C parity are forbidden by C conservation.

Transition	E1 approx. (keV)	TL [60](keV)	Experiment (keV)
$\Gamma(\psi' \to \chi_2)$	37.1	33	20.4 ± 4.0
$\Gamma(\psi' \to \chi_1)$	45.8	39	25.2 ± 4.5
$\Gamma(\psi' \to \chi_0)$	44.6	33	26.1 ± 4.5
$\Gamma(\chi_2 \to J/\psi)$	558	343	389 ± 60
$\Gamma(\chi_1 \to J/\psi)$	422	276	290 ± 60
$\Gamma(\chi_0 \to J/\psi)$	196	144	165 ± 40

Table 1.3: E1 transitions for low lying states of charmonium. The experimental data are given by ref. [27], and theoretical estimates by ref. [60].

Transition	TL [60](keV)	Experiment (keV)
$\Gamma(J/\psi \to \eta_c\gamma)$	1.25	1.14 ± 0.39
$\Gamma(\psi' \to \eta_c\gamma)$	1.13	0.84 ± 0.24

Table 1.4: M1 transitions for S states of charmonium. The experimental data are given by ref. [27], and theoretical estimates by ref. [60].

Chapter 2

ψ' decays: theory and experiment

The J/ψ and ψ' have been studied mostly from e^+e^- annihilation. Experiments carried out at the SLAC storage ring SPEAR provided measurements of ψ' radiative decays, branching ratios in $J/\psi X$ and in cascade decays $J/\psi\gamma\gamma$. At Fermilab, the E760 collaboration produced charmonium through $\overline{p}p$ annihilation, like the predecessor experiment R704 at CERN. To date R704, E760 and its upgrade E835 are the only experiments which studied charmonium from $\overline{p}p$ annihilations.

The ψ' mass present estimate is 3685.96 ± 0.09 MeV [27]. The first experiment to measure $m_{\psi'}$ was the SLAC-LBL collaboration at SPEAR, which measured $m_{\psi'} = 3695 \pm 4$ MeV [22]. Successively, experiment E760 at FNAL measured $m_{\psi'} = 3686.02 \pm 0.09 \pm 0.27$ MeV [33] from $\overline{p}p \to e^+e^-$ events. Detector OLYA at VEPP-4 studied 413 $e^+e^- \to$ *hadrons* events and estimated $m_{\psi'} = 3685.95 \pm 0.10$ MeV [16]. The value quoted in [27] is an average of the E760 and OLYA measurements.

2.1 Theory of ψ' decays

2.1.1 $^3S_1$ leptonic width

The first entry in table 1.1 shows the charmonium $^3S_1$ leptonic width based on the Van Royen-Weisskopf formula [81]:

$$\Gamma(^3S_1 \to e^+e^-) = 16\pi\frac{\alpha^2 e_q^2}{(2m)^2} \mid \psi(0) \mid^2 \tag{2.1}$$

We will review briefly the steps leading to 2.1. We start from the Feynman diagram in figure 1.3(b), where $\overline{c}c$ annihilate into a virtual photon; we write the matrix element as:

$$\mathcal{M} = \frac{e^2 e_c}{s}\overline{v}(p_2)\gamma_\mu u(p_1)\overline{v}(k_2)\gamma^\mu u(k_1) \tag{2.2}$$

where s is the square of the center of mass energy, $e_c(=2/3)$ is the quark charge in units of the proton charge, $p_{1,2}$ and $k_{1,2}$ are the 4-momenta of the quarks and electrons respectively, and u and v the particle-antiparticle spinors. We sum over final spins and average over initial spins, and we use Casimir's trick to rewrite 2.2 in terms of traces:

$$\overline{\mid \mathcal{M} \mid^2} = \frac{1}{4}\frac{e^4 e_c^2}{s^2} Tr[\gamma_\mu(\not{p}_1 + m)\gamma_\nu(\not{p}_2 - m)]\; Tr[\gamma^\mu \not{k}_1 \gamma^\nu \not{k}_2] \tag{2.3}$$

where we have neglected the mass of the final particles. Using the trace theorems (see [73]) we find:

$$\overline{\mid \mathcal{M} \mid^2} = 8\frac{e^4 e_c^2}{s^2}[(p_1\cdot k_1)(p_2\cdot k_2) + (p_1\cdot k_2)(p_2\cdot k_1) + m^2(p_1\cdot p_2)] \tag{2.4}$$

$$\frac{d\overline{\sigma}}{d\Omega} = \frac{e_c^2\alpha^2}{4s}\frac{k}{p}\left[1 + \frac{4m^2}{s} + (1 - \frac{4m^2}{s})\cos^2\theta\right] \tag{2.5}$$

$$\overline{\sigma} = \frac{\pi e_c^2\alpha^2}{s}\frac{k}{p}\left[\frac{4}{3} + \frac{2}{3}\frac{4m^2}{s}\right] \tag{2.6}$$

where $k = \mid \vec{k}_1 \mid = \mid \vec{k}_2 \mid$, $p = \mid \vec{p}_1 \mid = \mid \vec{p}_2 \mid$, and θ is the angle between the $\overline{c}c$ and e^+e^- directions, in the center of mass. Define $v_r = \mid \vec{v}_1 - \vec{v}_2 \mid$. If the $\overline{c}c$ motion is non

relativistic $k \to m$, $s \to 4m^2$ and $p \to (1/2)mv_r$; then the cross section takes the form:

$$\overline{\sigma} = \frac{\pi e_c^2}{m^2}\frac{\alpha^2}{v_r} \tag{2.7}$$

The transition probability for a density of one particle per unit volume is given by $\overline{\sigma}v_r$; to obtain the transition rate we need to:

- multiply by the density $\mid \psi(0) \mid^2$
- multiply by 4/3 to account for the $\overline{c}c$ spins in triplet state
- substitute $e_c^2 = 4/9$
- multiply by a color factor equal to 3

We find:

$$\Gamma(^3S_1 \to e^+e^-) = \frac{64\pi}{9}\frac{\alpha^2}{(2m)^2} \mid \psi(0) \mid^2 \equiv \Gamma_{ee}^{(0)} \tag{2.8}$$

Including a single gluonic radiative correction at the annihilation vertex of the quarks one obtains [11][75]:

$$\Gamma(^3S_1 \to e^+e^-) = \frac{64\pi}{9}\frac{\alpha^2}{(2m)^2} \mid \psi(0) \mid^2 \left(1 - \frac{16\ \alpha_s(-4m^2)}{3\pi}\right) \tag{2.9}$$

Aside from α_s in place of α and a color factor of 4/3, the correction in 2.9 is the same obtained for positronium when studying lowest order radiative corrections to the annihilation diagram [57].

Several calculations of the leptonic decay rates of quarkonium including radiative corrections exist in the literature. We will mention here Buchmüller and Tye [6], Gupta *et al.* [79] and Grotch *et al.* [83]. Buchmüller and Tye proposed a potential model incorporating asymptotic freedom and linear confinement; they used the Regge slope α' and the QCD scale parameter Λ to determine the potential, finding a fair

agreement with experiment, particularly for the leptonic width of the ψ. In the Bethe-Salpeter formalism for relativistic bound states they derive:

$$\Gamma_{ee} = \Gamma^0_{ee}\left(1 - \frac{16\alpha_s(-4m_c^2)}{3\pi} \pm \Delta\right) \tag{2.10}$$

Higher order radiative and relativistic corrections are incorporated into $\Delta = \Delta_{rad} + \Delta_{rel}$ as an uncertainty, whose order of magnitude they estimated as follows: i) the coefficient of the higher order radiative correction was assumed to be of the same order of magnitude as the lowest order coefficient (i.e. $\Delta_{rad} = (16/3\pi)\alpha_s^2$); ii) $\Delta_{rel} = v^2/c^2$ is estimated from the model, using a running coupling constant evaluated for $\Lambda_{\overline{MS}} = 0.5$ GeV. They obtained the theoretical leptonic width $\Gamma_{ee}(\psi) = 3.70 \pm 3.05$ keV.

Gupta *et al.* proposed a quarkonium model based on the semirelativistic Hamiltonian:

$$H = 2\sqrt{\vec{p}^2 + m^2} + V_p(\vec{r}) + V_c(\vec{r}) \tag{2.11}$$

with

$$V_c = (1 - B)V_S + BV_V \tag{2.12}$$

where V_p and V_c are the second-order perturbative and confining potentials, and B is an arbitrary parameter. The expressions for V_p, V_S and V_V are obtained in the quasistatic approximation and are reported in ref. [51]. The trial wave function is of the form:

$$\psi^m_{nl}(\vec{r}) = \sum_{k=0}^{K} a_{L,nl}\left(\frac{r}{R}\right)^L e^{-r/R} Y^m_l(\Omega_{\vec{r}}), \quad L = k + l \tag{2.13}$$

The coefficients $a_{L,nl}$ are determined by minimizing the expectation value of the unperturbed Hamiltonian, while R is determined by means of the virial theorem. The comparison with experimental results for the leptonic width is shown in table 2.1. The theoretical estimate was obtained with formula 2.9; the result is in fair agreement with the experimental data.

State	Γ_{ee} $(Theory)$	Γ_{ee} (Exp)
1^3S_1	5.57	5.26
2^3S_1	2.87	2.19

Table 2.1: Charmonium leptonic widths in keV from Gupta *et al.* quarkonium model [79]

It has been recently pointed out ([83]) that the term $16\alpha_s/3\pi$ is the zero quark momentum limit (static limit) of the contribution due to the exchange of a transverse gluon between quark and antiquark, and that one has to remove from the one gluon vertex correction all terms already accounted for in the wave function $\psi(0)$ to avoid overcounting. Moreover, the static limit is not a reasonable approximation for charmonium, where $\beta^2 \sim 0.2 \div 0.3$. Grotch *et al.* calculated the charmonium decay rate into lepton pairs including the residual single gluon radiative correction without making any static approximations and avoiding the use of the Bethe-Salpeter formalism but including relativistic effects [83]; the quark and the antiquark are taken to be on mass shell, but this gives rise to a divergence "cured" by introducing a cutoff parameter μ. The results, obtained within the framework of the potential model by Gupta *et al.* mentioned in the previous paragraph, are not in good agreement with experiments and they depend on the value of μ.

2.1.2 ψ' two pion transitions

We summarize here two of the theoretical approaches developed to describe the coupling of two pions to heavy mesons. The first is a QCD motivated model where the multipole expansion of the gluon field is applied, and the two pions couple to the heavy meson as a whole; this approach was introduced by Voloshin and Zakharov [86] and refined by Novikov and Shifman [66]. The second model was proposed by Lähde

and Riska [59], and it is based on a $Q\pi\pi$ interaction lagrangian with derivative pion couplings.

2.1.3 $\psi' \to J/\psi\pi\pi$ description in QCD multipole expansion

A perturbative approach in QCD is not possible for this transition; the gluons are soft, therefore the running coupling constant is large. In heavy quarkonium the size of the $Q\overline{Q}$ bound state is small compared to the size of the emitted light quark systems, so that the multipole expansion of the gauge field can be used; if the quark mass is large enough the expansion exhibits fast convergence [45]. It was shown by Voloshin and Zakharov [86] that the conversion of gluons in the transitions between S states is described by the matrix element:

$$< \pi\pi \mid g^2 G^a_{\mu\nu}(x) G^a_{\mu\nu}(x) \mid 0 >, \quad g^2 = 4\pi\alpha_s \tag{2.14}$$

where $G^a_{\mu\nu}$ is the gluon field strength operator and g is the QCD coupling constant. They found that for low q and neglecting the pion mass μ_π:

$$< (\pi\pi)_{J=0} \mid g^2 G^a_{\mu\nu} G^a_{\lambda\sigma} \mid 0 >= -\frac{8\pi^2}{3b} q^2 \left(\frac{1}{2}\phi^\alpha_\pi \phi^\alpha_\pi\right)(g_{\mu\lambda}g_{\nu\sigma} - g_{\mu\sigma}g_{\nu\lambda}) \tag{2.15}$$

where q is the total 4-momentum of the pions, $b = 11 - (2/3)n_f$ is the coefficient of the QCD β function ($\beta = bg^3/16\pi^2$) and ϕ^α_π is the pion isotopic amplitude. The description of the interaction of the heavy quarks with the soft gluon fields is based on a electric-dipole-type hamiltonian:

$$\mathcal{H}_d = -\frac{1}{2} g \xi^a \vec{r} \vec{E}^a(0) \tag{2.16}$$

where $\xi^a = t^a_1 - t^a_2$, $t^a_{1,2}$ are the color SU(3) generators for quark and antiquark respectively, and $E^a_i = G^a_{0i}$. The calculation of the decay amplitude, using 2.15, yields:

$$A_{\pi\pi} =< \pi\pi \mid g^2 \vec{E}^a \vec{E}^a \mid 0 > (\vec{\Sigma}'\vec{\Sigma}) A_0/4 \tag{2.17}$$

where $\vec{\Sigma}'$ and $\vec{\Sigma}$ are the spin amplitudes for initial and final charmonium states, and A_0 is a matrix element which depends on initial and final charmonium wave functions. Using 2.15 the amplitude $A_{\pi\pi}$ can be written as:

$$A_{\pi\pi} = \frac{2\pi^2}{b}(q^2 - \lambda\mu_\pi^2)(\vec{\Sigma}'\vec{\Sigma})(\frac{1}{2}\phi_\pi^\alpha\phi_\pi^\alpha)A_0 \tag{2.18}$$

where the term proportional to μ_π^2 can be determined from phenomenological analysis.

Novikov and Shifman recalculated 2.17 introducing an effective amplitude with explicit S-wave and D-wave state dipion contributions [66]:

$$A_{eff} = \Big[(S\ wave)^2 + (D\ wave)^2\Big]^{1/2} = \left[\frac{d\Gamma(\psi' \to J/\psi\pi\pi)}{dq^2}\Big/(phase\ space)\right]^{1/2} \tag{2.19}$$

They found the following expressions:

$$A_{eff} = C\sqrt{\left[q^2 - \kappa(\Delta M)^2\left(1 + \frac{2m_\pi^2}{q^2}\right)\right]^2 + \frac{\kappa^2}{5}[(\Delta M)^2 - q^2]^2\left(1 + \frac{4m_\pi^2}{q^2}\right)^2} \tag{2.20}$$

$$\kappa = \frac{3}{2\pi}\alpha_s(\mu)\rho^G(\mu) \tag{2.21}$$

where C is a constant, $q^2 = (p_1 + p_2)^2$ is the dipion mass, $\Delta M = M_{\psi'} - M_{J/\psi}$ and $\rho^G(\mu)$ is the fraction of the pion momentum carried by gluons. The second term in 2.21 is associated with the D wave dipion emission; it vanishes at both ends of the q^2 spectrum, for $q^2 \to 4m_\pi^2$ and $q^2 \to (\Delta M)^2$, and it is suppressed by a factor of $\kappa/5$ at intermediate q^2.

κ is a calculable numerical coefficient. To evaluate κ one needs to know $\alpha_s(\mu)$ and $\rho^G(\mu)$; for the $\psi' \to J/\psi\pi\pi$ transition $\alpha_s(\mu)$ was set to 0.7[1] and the glue fraction of a pion was assumed to be the same as the glue fraction of a nucleon at $Q^2 \sim$ 1 GeV^2 (for which $\rho^G(\mu) = 0.5$); these numbers yield $\kappa \sim 0.2$.

[1]See [85] for an argument supporting this choice.

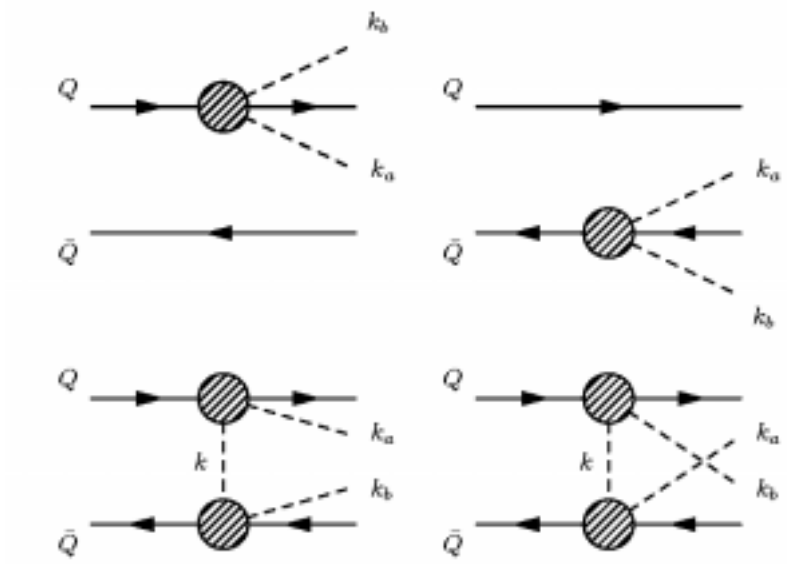

Figure 2.1: Feynman diagrams at tree level for the $\psi' \to J/\psi\pi\pi$ transition. The upper two diagrams show the single quark coupling to the pions; the pion exchange between the heavy quarks is described by the two lower diagrams.

2.1.4 $\psi' \to J/\psi\pi\pi$ width from effective interaction Lagrangian

Lähde and Riska [59] used an interaction hamiltonian with the Blackenbecler-Sugar equation to determine wave functions and spectra of charmonium. Their model for $\pi\pi$ decay leads to an expression for the $\psi' \to J/\psi\pi\pi$ width from a $Q\pi\pi$ interaction lagrangian of the form:

$$\mathcal{L}_{Q\pi\pi} = 4\pi\lambda\overline{\psi}_Q(\partial_\mu\pi_a)(\partial^\mu\pi_a)\psi_Q \tag{2.22}$$

where ψ_Q is the heavy quark spinor, π_a is the pion field and $\lambda(\mathrm{MeV}^{-3})$ is a coupling constant. The tree-level diagrams relevant to the interaction modeled by 2.22 include direct coupling of the two pions to the single constituent quarks as well as pion exchange diagrams, as shown in fig.2.1. The pion rescattering is modeled by modifying the λ coupling constant with the inclusion of a scalar meson resonance σ

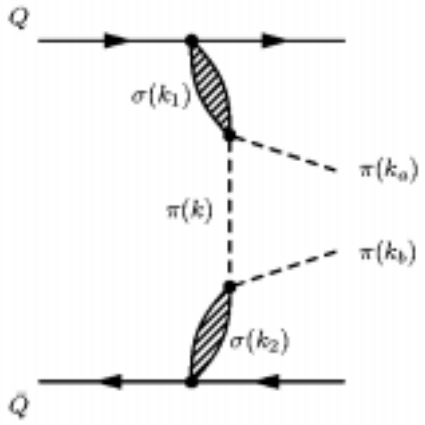

Figure 2.2: Pion rescattering model with intermediate σ mesons [59].

with a Breit-Wigner type propagator:

$$\lambda \to \lambda \left(\frac{M_\sigma^2 + \Gamma_\sigma^2/4}{M_\sigma^2 + q^2 + \Gamma_\sigma^2/4} \right) \tag{2.23}$$

The width is calculated from the expression:

$$\Gamma_{\pi\pi} = \frac{1}{(2\pi)^5} \int d^3k_a d^3k_b d^3P_f \frac{M_f M_i}{E_f E_i} \frac{\mid T_{fi} \mid^2}{4\omega_a \omega_b} \delta^{(4)}(P_f + k_a + k_b - P_i) \tag{2.24}$$

where $\omega_{a,b}$ and $k_{a,b}$ are the energies and 4-momenta of the emitted pions, $P_{i,f}$ are the 4-momenta of the heavy quarkonium, $M_{i,f}$ and $E_{i,f}$ are masses and energies of the heavy mesons and T_{fi} is the amplitude:

$$T_{fi} = T_Q + T_{\overline{Q}} + T_{ex} + T_{exc} = T_{1Q} + T_{2Q} \tag{2.25}$$

T_Q and $T_{\overline{Q}}$ are the pion emission amplitudes from single quark and antiquark, and $T_{ex,exc}$ indicate the pion exchange amplitudes (lower two diagrams in fig.2.1). The modification of the coupling constant 2.23 corresponds to the model depicted in fig.2.2, where the crossed diagram is obtainable by exchanging k_a and k_b. The single-quark amplitude is found to be:

$$T_{1Q} = -16\pi\lambda \left(\frac{M_\sigma^2 + \Gamma_\sigma^2/4}{M_\sigma^2 + q^2 + \Gamma_\sigma^2/4} \right) \left[m_\pi^2 - \frac{1}{2}((\omega_a + \omega_b)^2 - \vec{q}^2) \right] \mathcal{M}_{1Q} \tag{2.26}$$

where the matrix element $\mathcal{M}_{1Q}$ is evaluated in the relativistic case. The pion exchange amplitude contains a triple propagator which can be simplified by approximating $\vec{k}_1 \sim -\vec{k}$, $\vec{k}_2 \sim \vec{k}$, $\mid k_1^0 \mid \sim \mid k_2^0 \mid \sim (\omega_a + \omega_b)/2$ and $\mid k^0 \mid \sim (\omega_a - \omega_b)/2$; this amounts to assuming that: i) the momenta of the σ mesons are equivalent in magnitude to the momentum of the exchanged pion, ii) the exchanged pion carries most of the 3-momentum and iii) the emitted pions carry most of the energy. The sum of the two pion exchange amplitudes yields the expression:

$$T_{2Q} = -2 \cdot (8\pi\lambda)^2 \Big[\frac{1}{3} \left(\frac{\vec{q}^{\,2}}{4} - Q_f^2 \right) (\mathcal{M}_{e1} - A^2(\mathcal{M}_{e2} - \mathcal{M}_{e3})) + \tag{2.27}$$

$$+ \left(\frac{\vec{q}^{\,2} z^2}{4} - \frac{2Q_f^2}{3} - \frac{\vec{q}^{\,2}}{12} \right) \mathcal{M}_{e4} + \frac{\omega_a \omega_b}{4} (\omega_a - \omega_b)^2 (\mathcal{M}_{e2} - \mathcal{M}_{e3}) \Big] \tag{2.28}$$

In eq.2.28 the following variables are defined as: $\vec{q} = \vec{k}_a + \vec{k}_b$, $\vec{Q} = (\vec{k}_b - \vec{k}_a)/2$, $A = \sqrt{m_\pi^2 - k_0^2}$ and $z = \vec{Q} \cdot \vec{q}/Qq$. Q_f is the relative momentum of the emitted pions (constrained by the δ function in eq. 2.24):

$$Q_f^2 \equiv \frac{(E_f - M_i)^4 - (4m_\pi^2 + q^2)(E_f - M_i)^2}{4(E_f - M_i)^2 - 4q^2 z^2} \tag{2.29}$$

$\mathcal{M}_{e1\ldots e4}$ indicate the matrix elements in the non-relativistic approximation (refer to [59] for the full expressions). In order to compare the calculated width with the experimental results it is necessary to assign a value to the free parameter λ; this parameter is strongly influenced by the shape of the $\pi\pi$ energy distribution, therefore both the theoretical widths, shown in table 2.2, and the $\pi\pi$ energy spectrum, shown in fig. 2.3, for $\psi' \to J/\psi\pi^+\pi^-$ and $\Upsilon' \to \Upsilon\pi^+\pi^-$ have been optimized through an appropriate choice of λ.

2.1.5 The angular distribution for $\psi' \to e^+e^-$

Let us derive the angular distribution for this decay using the helicity formalism. It is useful to describe the scattering amplitude for a process $\overline{p}p \to \psi' \to e^+e^-$ in

Decay	Γ_{tot}	$\Gamma_{\pi\pi}$ (Exp)	$\Gamma_{\pi\pi}$ $(Theor.)$
$\psi' \to J/\psi\pi^+\pi^-$	$277 \pm 31\ keV$	$86 \pm 12\ keV$	$53.5\ keV$
$\psi' \to J/\psi\pi^0\pi^0$	$277 \pm 31\ keV$	$50 \pm 10\ keV$	$27.8\ keV$

Table 2.2: Comparison between experimental and theoretical widths from the Lähde-Riska model [59], for $\psi' \to J/\psi\pi\pi$. The mass and width of the intermediate meson σ were chosen as $m_\sigma = 450\ MeV$, $\Gamma_\sigma = 550\ MeV$. The parameter $\lambda = -0.02\ fm^3$ was chosen to optimize both $\overline{c}c$ and $b\overline{b}$ data.

partial amplitudes in the basis $\mid \vec{p}, h >$. In the CM reference frame we can substitute the momentum with the direction vectors $\vec{n} = \vec{p}/p$ for e^+e^- and $p\overline{p}$. We can write the $\mathcal{S}$ matrix element as:

$$< \vec{n}', h' \mid \mathcal{S} \mid \vec{n}, h > =$$

$$\sum_{J,M} \frac{2J+1}{4\pi} D^J_{H'M}(\phi', \theta', -\phi') D^{*J}_{HM}(\phi, \theta, -\phi) < h' \mid \mathcal{S} \mid h > \qquad (2.30)$$

where:

$$\begin{aligned}
\vec{n}'(\phi', \theta', -\phi') &= \overline{p}\ direction \\
\vec{n}(\phi, \theta, -\phi) &= e^+e^- direction \\
h &= (h_{e^+}, h_{e^-})\ helicity\ of\ e^\pm \\
h' &= (h_p, h_{\overline{p}})\ helicity\ of\ p(\overline{p}) \\
H &= h_{e^+} - h_{e^-} \\
H' &= h_p - h_{\overline{p}}
\end{aligned}$$

Equation 2.30 contains the sum over all possible angular momenta; we can keep only J=1, since $J_{\psi'} = 1$. We can also separate the contributions from the ψ' decay and formation in $< h' \mid \mathcal{S} \mid h >$:

$$< h' \mid \mathcal{S} \mid h > = < h' \mid \mathcal{S}_{e^+e^-} \mid JM > < JM \mid \mathcal{S}_{p\overline{p}} \mid h > \equiv A_H \cdot C_{H'} \qquad (2.31)$$

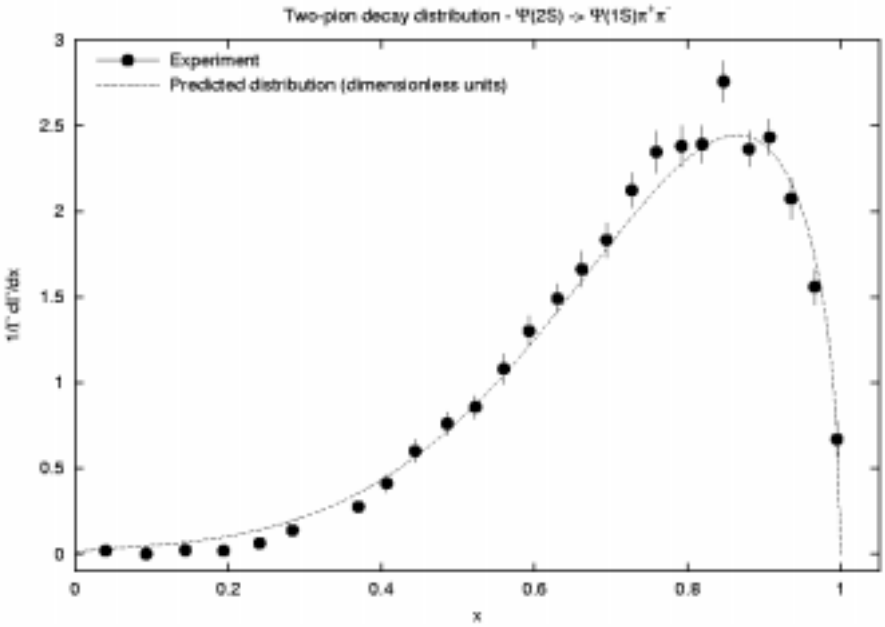

Figure 2.3: Comparison between experimental and theoretical $\pi\pi$ energy distributions in the Lähde-Riska model [59], for $\psi' \to J/\psi\pi\pi$ and $m_\sigma = 450\ MeV$, $\Gamma_\sigma = 550\ MeV$, $\lambda = -0.02\ fm^3$. The dimensionless variable x is defined as $\frac{m_{\pi\pi}-2m_\pi}{M_i-M_f-2m_\pi}$.

We can rewrite eq. 2.30 as:

$$\mathcal{M} = < \vec{n}', h' \mid \mathcal{S} \mid \vec{n}, h > \propto\ D^1_{H',H}(\phi,\theta,0)\ A_H\ C_{H'} \tag{2.32}$$

where we chose $\vec{n}'$ parallel to the $\overline{p}$ direction, so that $D^1_{H',M}(\phi,\theta,-\phi) = \delta_{H',M}$.

Element 2.32 must be squared, averaged over the possible helicity combinations of $\overline{p}p$ and summed over the possible helicity combinations of e^+e^-. For $\overline{p}p$ the possible helicity values are (-1,0,1), with two possible ways to get 0. For e^+e^- we only have $H = \pm 1$ when we neglect the mass of the ultrarelativistic electron and positron. So, the total number of helicity amplitudes in this process is 5: $A_1, A_{-1}, C_1, C_0, C_{-1}$. These amplitudes are not all independent; parity conservation requires:

$$A_H \ = \ \eta_{\psi'}\eta_{e^+e^-}(-1)^{S_{\psi'}-(S_{e^+}+S_{e^-})}A_{-H} = \ (-1)(-1)(-1)^0 A_{-H} = A_{-H} \tag{2.33}$$

$$C_{H'} \ = \ \eta_{\overline{p}p}\eta_{\psi'}(-1)^{(S_p+S_{\overline{p}})-S_{\psi'}}C_{-H'} = \ (-1)(-1)(-1)^0 C_{-H'} = C_{-H'} \tag{2.34}$$

Let us remember how the rotation matrix $D^J_{M,M'}$ is related to the d functions:

$$D^{*J}_{M,M'}(\phi,\theta,\zeta) = e^{-iM\phi} d^J_{M,M'}(\theta) e^{-iM'\zeta} \tag{2.35}$$

and the useful identity $d^J_{M',M} = (-1)^{M-M'} d^J_{M,M'} = d^J_{-M,-M'}$. Now we square the matrix element, sum over the the e^+e^- helicities and average over the $\overline{p}p$ helicities:

$$\mid \mathcal{M} \mid^2 \;\propto\; \sum_H \sum_{H'} A^2_H C^2_{H'} [d^1_{H,H'}(\theta)]^2 \tag{2.36}$$

$$\mid \mathcal{M} \mid^2 \;\propto\; 2A^2_1 C^2_1 [d^1_{1,1}(\theta)]^2 + 2A^2_1 C^2_1 [d^1_{1,-1}(\theta)]^2 + 4A^2_1 C^2_0 [d^1_{1,0}(\theta)]^2 \tag{2.37}$$

$$\mid \mathcal{M} \mid^2 \;\propto\; 2C^2_0 + C^2_1 + (C^2_1 - 2C^2_0)[\cos(\theta)]^2 \tag{2.38}$$

where we have used:

$$d^1_{1,1} = \frac{1+\cos\theta}{2} \quad , \quad d^1_{1,0} = \frac{-\sin\theta}{\sqrt{2}} \quad , \quad d^1_{1,-1} = \frac{1-\cos\theta}{2} \tag{2.39}$$

Finally, we write the angular distribution in the form:

$$\frac{d\sigma}{d\Omega} = 1 + \frac{C^2_1 - 2C^2_0}{2C^2_0 + C^2_1} \cos^2\theta = 1 + \lambda \cos^2\theta \tag{2.40}$$

Observe that $\mid \lambda \mid \leq 1$, for $\overline{p}p \to \psi' \to e^+e^-$. This parameter depends on the ψ' formation amplitudes; if we had produced the ψ' through e^+e^- annihilation we could not include the contribution of helicity zero, therefore λ would be always equal to 1.

The process of $\overline{p}p$ annihilation into a ψ' and decay into a e^+e^- pair can be viewed as the strong interaction analogous to the electromagnetic $\overline{p}p \to e^+e^-$, with the annihilation proceeding through the charmonium 1^{--} state ψ' instead of an intermediate photon.

The coupling at the electron-positron vertex is pointlike, and the vertex factor is $ie\gamma^\mu$; at the $\overline{p}p$ vertex it can be written as:

$$-ie\Gamma^\mu = -ie\gamma^\mu F_1(q^2) - e\frac{\sigma^{\mu\nu} q_\nu}{2m_p} F_2(q^2) \tag{2.41}$$

where $F_{1,2}$ are Pauli's form factors, m_p is the proton mass and $\sigma^{\mu\nu} = i[\gamma^\mu, \gamma^\nu]/2$. In the electromagnetic case $F_{1,2}$ are related to the electric and magnetic proton form factors, or Sachs form factors, by:

$$G_E = F_1 + \frac{s}{4m_p^2} F_2 \ , \ G_M = F_1 + F_2 \tag{2.42}$$

where we set $q^2 = s$; in $\overline{p}p \to e^+e^-$ q^2 is timelike and equal to the square of the total center of mass energy. With a calculation entirely analogous to the electromagnetic case it is possible to find the square amplitude, averaged over the initial helicity states and summed over the final helicities:

$$\overline{\mid \mathcal{M} \mid}^2 \propto 1 + \frac{E_{cm}^2 - 4 \mid \frac{G_E}{G_M} \mid^2 m_p^2}{E_{cm}^2 + 4 \mid \frac{G_E}{G_M} \mid^2 m_p^2} \cos^2 \theta \tag{2.43}$$

therefore the angular distribution parameter λ is related to $G_{E,M}$ by:

$$\lambda = \frac{E_{cm}^2 - 4 \mid \frac{G_E}{G_M} \mid^2 m_p^2}{E_{cm}^2 + 4 \mid \frac{G_E}{G_M} \mid^2 m_p^2} \tag{2.44}$$

A pointlike proton would imply $F_2 = 0$, and $G_E = G_M$; in this case from 2.44 we get $\lambda = 0.59$, for the ψ'.

In the $\overline{p}p$ annihilation through a charmonium $^3S_1$ resonance $G_{E,M}$ are specific to the decaying charmonium state, and they are not related to the charge and magnetic moment distributions inside the proton. Asymptotic freedom and quark confinement both contribute to the process and make its understanding more complex. Hadron form factors have not as yet been predicted in QCD, although several theoretical models have been put forward to explain proton structure, with various degrees of success.

Brodsky and Lepage [4] use a perturbative expansion in terms of $\alpha_s(q^2)$. The baryon structure is pictured as three valence quarks, each carrying a fraction x_i of the baryon's momentum, and all moving roughly in parallel with the hadron. Using helicity selection rules within this model they find $\lambda = 1$ [5].

Claudson, Glashow and Wise [43] study the isospin violating electromagnetic contributions to $J/\psi \rightarrow$ *baryon* + *antibaryon*; they write the form factors $F_{1,2}$ according to the model [4], and find that F_2 is negligible compared to F_1. Their prediction for the ψ' is $\lambda = 0.59$.

Carimalo's model involves assigning to each constituent quark a mass equal to $m_p/3$ in a nonrelativistic bound-state model. Carimalo's estimate of the angular distribution parameter has the following expression, for the ψ' [9]:

$$\lambda = \frac{(1+r)^2 - r(1+6r)^2}{(1+r)^2 + r(1+6r)^2}\ ,\ r = \frac{m_p^2}{M_{\psi'}^2} \tag{2.45}$$

This expression leads to $\lambda = 0.802$.

2.2 Experimental results for ψ' decays

Contributions to the ψ' width come primarily from $\psi' \rightarrow J/\psi X$ transitions, direct decays to hadrons, radiative decays to intermediate χ_c states and second-order electromagnetic decays. Table 2.3 presents a summary of the world measurements of these partial widths; from the PDG2002 the present estimate for the total width is $\Gamma_{\psi'} = 300 \pm 25$ keV [27]. It is the result of an overall fit to 79 measured values to determine 23 parameters among χ_c and ψ' widths, branching ratios and combinations of branching ratios. The following sections will provide an overview of the experimental results concerning the channels studied in this thesis.

2.2.1 $\psi' \rightarrow J/\psi\pi\pi$

The transition $\psi' \rightarrow J/\psi\pi\pi$ is the largest contribution to $\Gamma_{\psi'}$. It accounts for 48.7% of the total width. The measurement of $B(\psi' \rightarrow J/\psi\pi^+\pi^-)$ was first performed at SPEAR by Abrams *et al.* from the $\pi^+\pi^-$ missing mass spectrum; they obtained

Decay mode	Γ_i/Γ (%)
hadrons	98.10 ± 0.30
virtual γ	2.9 ± 0.4
e^+e^-	0.73 ± 0.04
$\mu^+\mu^-$	0.70 ± 0.09
$\tau^+\tau^-$	2.7 ± 0.7
$J/\psi\pi^+\pi^-$	30.5 ± 1.6
$J/\psi\pi^0\pi^0$	18.2 ± 1.2
$J/\psi\eta$	3.13 ± 0.21
$J/\psi\pi^0$	0.096 ± 0.021
$3(\pi^+\pi^-)\pi^0$	0.35 ± 0.16
$2(\pi^+\pi^-)\pi^0$	0.30 ± 0.08
$\chi_0\gamma$	8.7 ± 0.8
$\chi_1\gamma$	8.4 ± 0.7
$\chi_2\gamma$	6.8 ± 0.6
$\eta_c\gamma$	0.28 ± 0.06

Table 2.3: Branching ratios for the most important ψ' decay modes [27].

$B(\psi' \to J/\psi\pi^+\pi^-) = 0.32 \pm 0.04$. From the distribution of the $\mu^+\mu^-$ effective mass the same collaboration measured $B(\psi' \to J/\psi X) = 0.57 \pm 0.08$ [23].

Studying the collinearity of the e^+e^- or $\mu^+\mu^-$ emission from ψ' decays Hilger *et al.* [20] measured $\Gamma(\psi' \to \mu^+\mu^-)/\Gamma(\psi' \to J/\psi X) = 0.014 \pm 0.003$. The number of decays $\psi' \to \mu^+\mu^-$ was estimated by subtracting the number of QED expected events from the number of elastic e^+e^- events, as shown in fig. 2.4. The muon pair event rate around the 3684 MeV region in fig. 2.4(a) shows the enhancement associated with the ψ'. Fig. 2.4(b) shows the collinearity distribution for muon pairs detected at center-of-mass energies within 0.5 MeV from the resonance energy. From direct observation of γ rays and charged particles they also found $\Gamma(\psi' \to \pi^+\pi^-)/\Gamma(\psi' \to \pi^0\pi^0) = 0.64 \pm 0.15$. More recently, experiment E760 at Fermilab measured $B(\psi' \to J/\psi\pi\pi)$ from $\overline{p}p$ annihilation and found $B(\psi' \to J/\psi\pi^0\pi^0) = 0.184 \pm 0.019 \pm 0.013$, $B(\psi' \to J/\psi\pi^+\pi^-) = 0.283 \pm 0.021 \pm 0.020$. E760 selected high invariant mass e^+e^- events

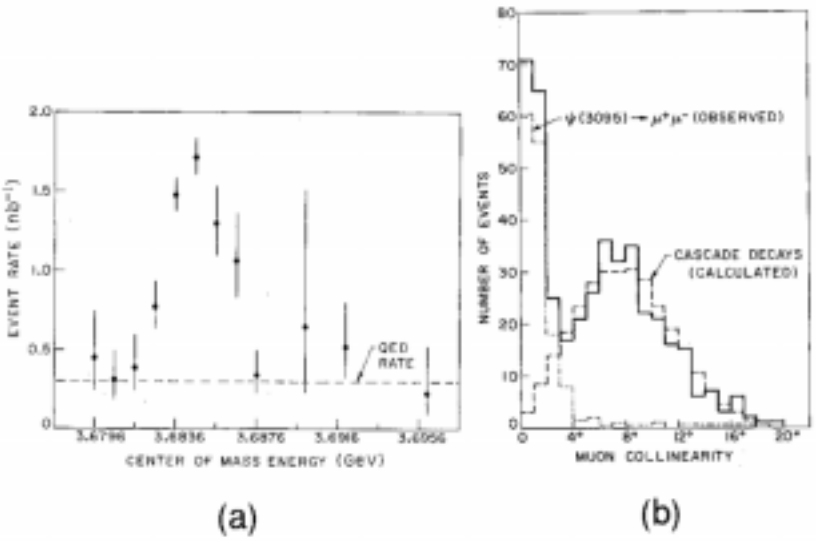

Figure 2.4: From Hilger *et al.* [20]: (a) Observed $\mu^+\mu^-$ rate from 603 events in the ψ' energy region, and QED expected rate (b) Muon collinearity distribution from 444 events within 0.5 MeV from the ψ' energy.

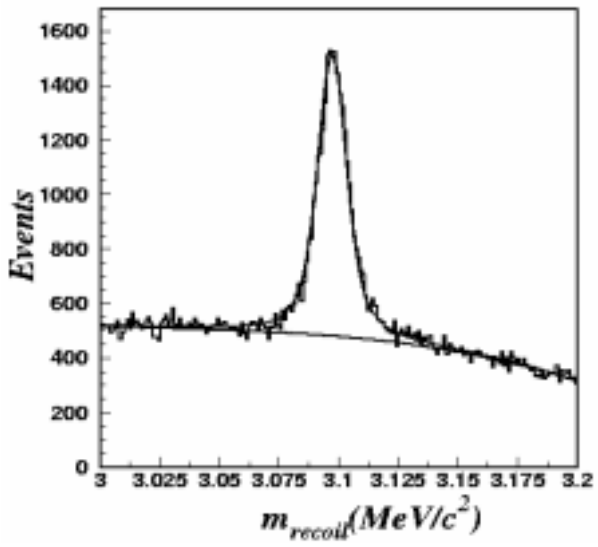

Figure 2.5: From BES II: mass recoiling against $\pi^+\pi^-$; the peak is from the J/ψ in $\psi' \to J/\psi\pi^+\pi^- \to$ *anything* $\pi^+\pi^-$.

with a combination of topological cuts and kinematical fits to identify $J/\psi\pi^+\pi^-$ and $J/\psi\pi^0\pi^0$ [35]. E835 measured $B(\psi' \to J/\psi\pi^0\pi^0) = 0.187 \pm 0.009 \pm 0.013$ [29] during its 1996-97 run. E760 and E835 measured the ψ' branching ratios, normalizing the number of events in each channel to the number of events in $\psi' \to J/\psi X$; this is also the approach followed in this thesis, and it will be described in detail in chapter 4. In 2002, the BES collaboration published $B(\psi' \to J/\psi\pi^+\pi^-) = 0.323 \pm 0.014$ [26], from a study of e^+e^- collisions. The 19425 $J/\psi\pi^+\pi^-$ events were selected by determining the mass, m_{rec}, recoiling against a pair of low energy pions; the m_{rec} distribution is fitted to a signal shape plus background to obtain the number of $\psi' \to J/\psi\pi^+\pi^-$ at each energy point. Fig. 2.5 shows the BES recoil mass distribution.

2.2.2 $\psi' \to J/\psi\eta$

The first observation of this channel was made by MARK I at SPEAR, in the decay sequence $\psi' \to J/\psi\eta \to \mu^+\mu^-\pi^+\pi^-(\pi^0, \gamma)$. The measurement was carried out

by detecting the two muons and one or two charged pions. The candidates were then selected by plotting the square of the mass recoiling against the muon pair and cutting to isolate the $\psi' \to J/\psi\pi^+\pi^-$ decays. From 48 candidates, it was found that $B(\psi' \to J/\psi\eta) = 0.043 \pm 0.008$ [39].

In 1978, a high statistics experiment at the DORIS storage rings at DESY measured branching ratios of several cascade electromagnetic decays $\psi' \to J/\psi\gamma\gamma$. The 624500 ψ' observed in this experiment were identified by the $\mu^+\mu^-$ decays of the J/ψ and by the two photons. The mass distribution for the two photon system was fitted with an experimental resolution function for the η signal, and with contributions from $\psi' \to \chi_c\gamma$ and $\psi' \to J/\psi\pi^0\pi^0$. The 164 events attributed to $J/\psi\eta$ gave a branching ratio of $B(\psi' \to J/\psi\eta) = (3.6 \pm 0.5)\%$ [38].

A year later, the DASP collaboration measured $B(\psi' \to J/\psi\eta) = (3.5 \pm 0.7)\%$ [31].

The Crystal Ball collaboration collected an even higher statistics sample of ψ' at SPEAR in 1980; from an integrated luminosity of 1518 nb^{-1} they examined 776000 ψ'. The selection of $\psi' \to J/\psi\gamma\gamma \to e^+e^-(\mu^+\mu^-)\gamma\gamma$ events was based on detection of all particles in the final state, and it yielded 2048 events. Fig. 2.6(b) shows the $J/\psi\eta$ events before background subtraction; after correcting for detection efficiency and acceptance, they obtained $B(\psi' \to J/\psi\eta) = (2.18 \pm 0.14 \pm 0.35)\%$ [30].

The E760 result, based on 23 events, was $B(\psi' \to J/\psi\eta) = (3.2 \pm 1.0 \pm 0.2)\%$ [35]; in 1996-97 E835 measured $B(\psi' \to J/\psi\eta) = (4.1 \pm 0.3 \pm 0.5)\%$ [29], from 193 events.

2.2.3 $\psi' \to e^+e^-$

The only previous measurement of the angular distribution parameter λ in $\overline{p}p \to \psi' \to e^+e^-$ decays has been performed by E760 [33], which found $\lambda(\psi') = 0.69 \pm 0.02$.

The first measurement of the leptonic decay width was performed at SPEAR in

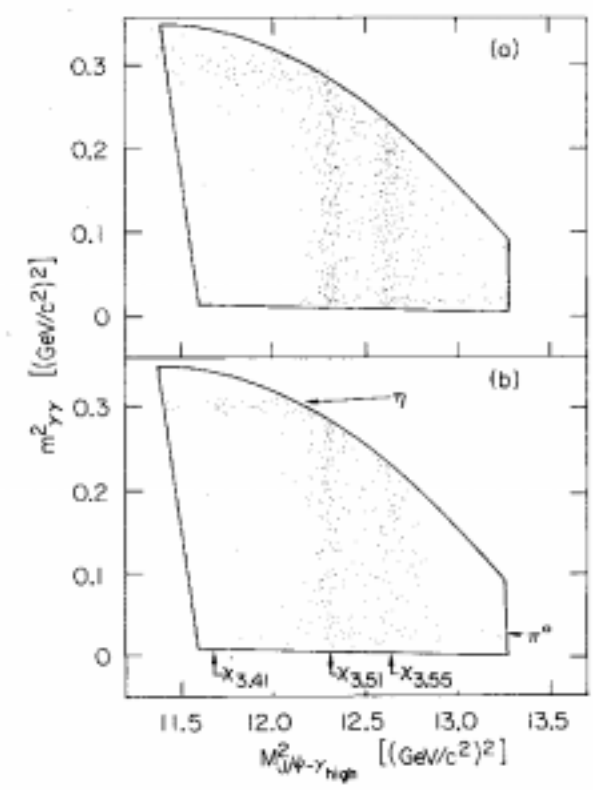

Figure 2.6: Dalitz plot for events $\psi' \to J/\psi\gamma\gamma$ from Crystal Ball [30]. It shows $m^2_{\gamma\gamma}$ versus the mass recoiling from the lower energy photon. The solid curves indicate the kinematical limits imposed by the cuts. (a) shows data satisfying selection criteria not including kinematical fit, whereas in (b) the events are fitted kinematically to $J/\psi\gamma\gamma$.

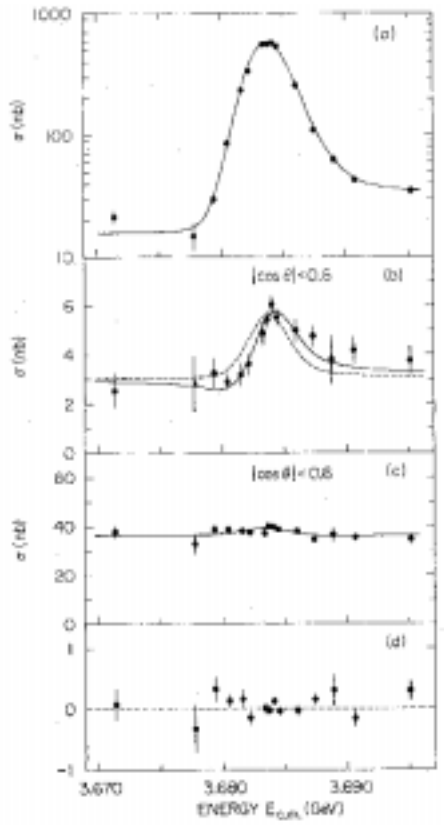

Figure 2.7: Cross sections for (a) $e^+e^- \rightarrow$ *hadrons*, (b) $e^+e^- \rightarrow \mu^+\mu^-$, (c) $e^+e^- \rightarrow e^+e^-$; (d) is the front-back asymmetry in $e^+e^- \rightarrow \mu^+\mu^-$. The solid curves are the fits to the data [37].

1975 [37]. The three observed processes were $e^+e^- \rightarrow$ *hadrons*, $e^+e^- \rightarrow e^+e^-, \mu^+\mu^-$. The measured cross sections, shown in fig. 2.7, were fitted simultaneously with a Breit-Wigner amplitude plus a nonresonant direct-channel amplitude, folded over the energy distribution of the colliding beams. The fit varies the mass m, the partial widths Γ_{had} and $\Gamma_e (= \Gamma_\mu)$, the energy spread of the machine, the nonresonant hadronic cross section and a luminosity normalization constant. The result is $\Gamma_e = 2.1 \pm 0.3$ keV and $\Gamma_{tot} = 228 \pm 56$ keV, with a corresponding branching ratio of $B(\psi' \rightarrow e^+e^-) = (0.93 \pm 0.16)\%$.

The DASP collaboration followed a similar approach in fitting the cross sections

and taking m, Γ_{had}, $\Gamma_e = \Gamma_\mu$ as free parameters. Their results were $\Gamma_e = 2.0 \pm 0.3$ keV and $\Gamma_{tot} = 202 \pm 57$ keV [31].

Chapter 3

The E835 experiment

In our experiment charmonium is formed by collision of an antiproton beam against a proton target in the form of a molecular hydrogen jet; the Fermilab antiproton accumulator provides the beam, and the E835 apparatus is situated along this beam line.

The E835 detector is a non magnetic spectrometer designed to detect with high efficiency the decays of charmonium states into electron-positron pairs and photons; it is an upgrade of the apparatus used for the predecessor experiment E760 at Fermilab.

The detector is composed of four sets of hodoscopes for charged track identification and triggering, two straw chambers for azimuthal angle measurement, two scintillating fiber detectors for polar angle measurement, a Čerenkov counter for electron identification, two electromagnetic calorimeters for triggering and energy/position measurements and a luminosity monitor; the trigger system performs the first event selection and the data acquisition system writes the preselected events to disk and tape.

3.1 The beam line.

The Fermilab beam acceleration system is shown in fig. 3.1. Until LHC comes online, its proton-antiproton collider is the highest energy particle collider in the world: it reaches an energy of 1 TeV and an instantaneous luminosity of 0.86×10^{32} $cm^{-2}s^{-1}$.

The proton beam is provided to the Tevatron through a 400 MeV Linac (with an H^- ion source and Cockroft-Walton accelerator) and an 8 Gev ring (the Booster).

The antiproton beam is provided by the Antiproton Source, which is comprised of a target station, two rings called Debuncher and Accumulator and the transport lines between these rings and the Main Injector.

In order to produce a $\overline{p}$ beam suitable for $\overline{p}p$ collisions the following steps are performed:

- A batch of protons is accelerated to 120 GeV in the Main Injector ring (MI).
- The protons are focused and directed onto a Ni-Cu target.
- The negatively charged particles are collected by means of a lithium lens and focused by means of a bending magnet while most of the other particles are directed to a beam dump.
- The surviving particles are injected into the Debuncher ring where the momentum spread of the 8.9 GeV beam is reduced through bunch rotation and adiabatic debunching. Most muons and pions in the beam decay while they are in this ring. The Debuncher reduces the momentum spread $\Delta p/p$ from $\simeq 3\%$ to less than 0.02%.
- Before the next pulse arrives from the target the particles are transferred to

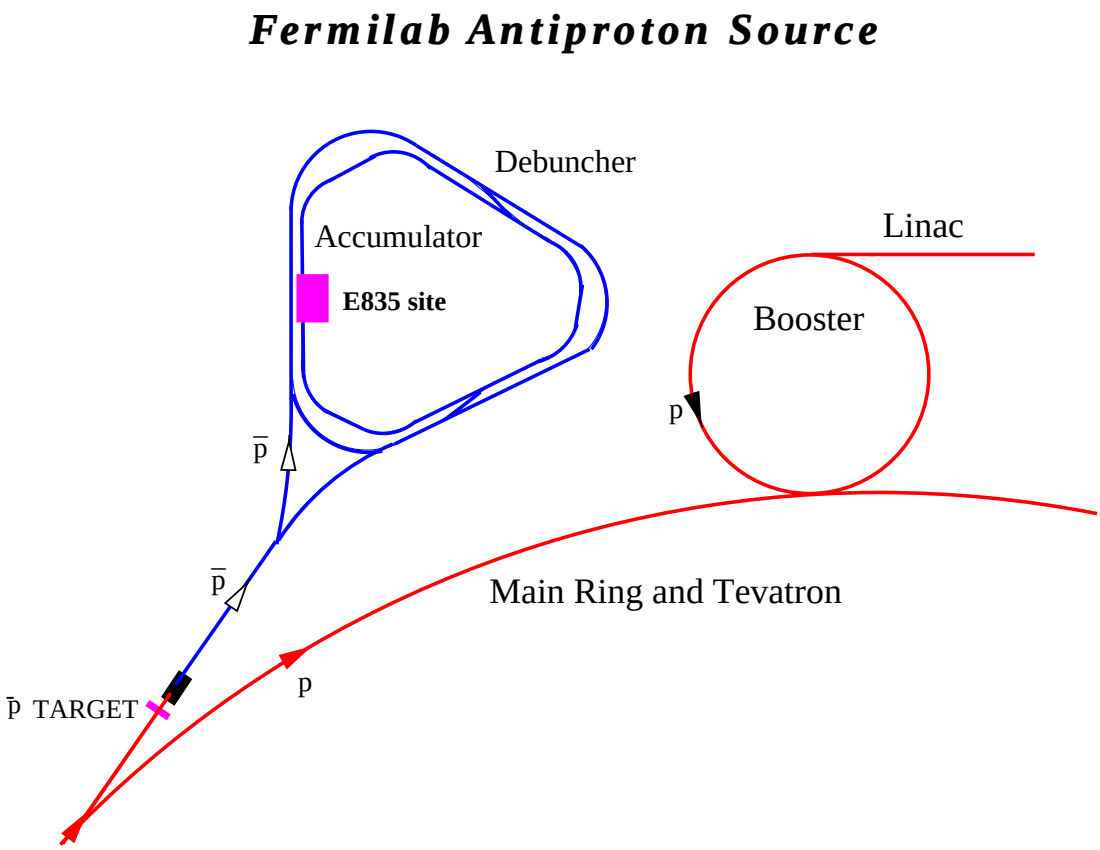

Figure 3.1: The Fermi National Accelerator beam line system.

the Accumulator ring. The accumulation rate is of the order of 10^{10} $\overline{p}$/hour. After several hours, enough $\overline{p}$ have been stored and are ready to be used in the Tevatron, or decelerated to the desired energy for E835 data collection.

E835 needs the momentum of the stored antiprotons to be reduced to values between 3.6 and 6.9 GeV; this range corresponds to CM energies in the range $2.95 \div 3.85$ GeV, since:

$$p_{\overline{p}} = E_{cm}\sqrt{\frac{E_{cm}^2}{4m^2} - 1} \tag{3.1}$$

3.1.1 $\overline{p}$ energy measurement

The precision of the $\overline{p}$ energy measurement determines the precision of the charmonium resonance mass measurement; the determination of the width of the $\overline{p}$ energy distribution affects the precision of the width measurement of narrow charmonium states. Knowledge of the beam parameters is therefore essential to this experiment.

The technique used to measure the beam energy distribution is as follows: we run at the ψ' peak energy and determine the beam momentum p_b; then, from the knowledge of the beam revolution frequency inside the accumulator ($\delta\nu/\nu \approx \pm 1.5 \times 10^{-7}$) we can measure the reference orbit length $L_0(\psi')$. As a reference orbit we use the one corresponding to the ψ' resonance, for which we know the energy with a small uncertainty (± 90 keV), from e^+e^- experiments. The energy of the $\overline{p}$ beam in the laboratory frame is:

$$E_{\overline{p}} = \gamma m_p \tag{3.2}$$

where :

$$\gamma = \frac{1}{\sqrt{1-(\nu L/c)^2}} \tag{3.3}$$

ν being the revolution frequency and L the orbit length.

The orbit length at different energies is related to the reference orbit by:

$$L = L_0 + \Delta L \tag{3.4}$$

where:

$$\Delta L \simeq \frac{1}{\rho_0} \sum_{i=1}^{N_d} \Delta x_i \Delta s_i. \tag{3.5}$$

in which Δx_i is the difference between the displacement of the new orbit and the reference orbit inside the i^{th} dipole, ρ_0 the average curvature radius, Δs the length of the bending dipole and N_d is the number of dipoles. It is possible to measure the displacements Δx_i with a system of Beam Position Monitors (BPMs) positioned along the ring. It is not possible to perform an absolute calibration of the BPMs; this is the reason why it is necessary to have a reference orbit to which we can associate a specific beam displacement configuration.

The error in the measurement of the beam frequency is very small, therefore the error in the determination of the resonance mass δM_0 depends almost exclusively on the error on the reference orbit length δL_0:

$$\delta L_0 / L_0 \simeq \frac{M_0}{\gamma_0^3 \beta_0^2 m_p^2} \delta M_0 \tag{3.6}$$

An uncertainty $\delta M_0 \simeq \pm 0.09$ MeV leads to an uncertainty in the reference orbit length of $\delta L_0 \simeq \pm 0.8\ mm$, at the ψ' energy. For the ψ' $L_0 = 474050\ mm$.

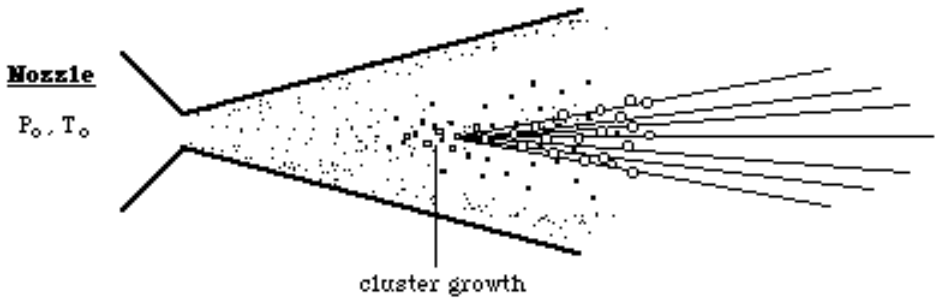

Figure 3.2: Schematic view of how the nozzle works.

3.2 The H_2 jet target

In order to achieve $\overline{p}$-p interaction the $\overline{p}$ beam circulating in the Accumulator is directed against a H_2 gas jet perpendicular to the $\overline{p}$ beam.

The structure and the density of the H_2 jet is chosen to maximize instantaneous luminosity and beam lifetime. For this purpose, a variable density jet target (JT) apparatus was developed. A detailed description of the target apparatus is given in [19].

The jet is made of gaseous H_2 pumped through a thin (37 μm) nozzle into the Accumulator ring. The vacuum in the ring is preserved by means of a system of pumps and skimmers. Fig. 3.2 presents a schematic drawing of the nozzle and fig. 3.3 shows the H_2 jet line and the recovery system. The H_2 gas flows through the nozzle at a temperature of about $20 - 45\ K$, and a pressure of $10 - 115\ psi$. Low T and P in the nozzle induce the formation of H_2 clusters in the axial region of the jet, with a density $\sim 10^{14}\ atoms/cm^3$. The actual target is formed selecting a 1.5° cone around the jet core, with a system of skimmers downstream of the nozzle. A recovery system prevents contamination of the beam pipe vacuum by pumping out of the jet target area the hydrogen which did not interact with the antiproton beam. The instantaneous luminosity depends on the density of the H_2 jet and on

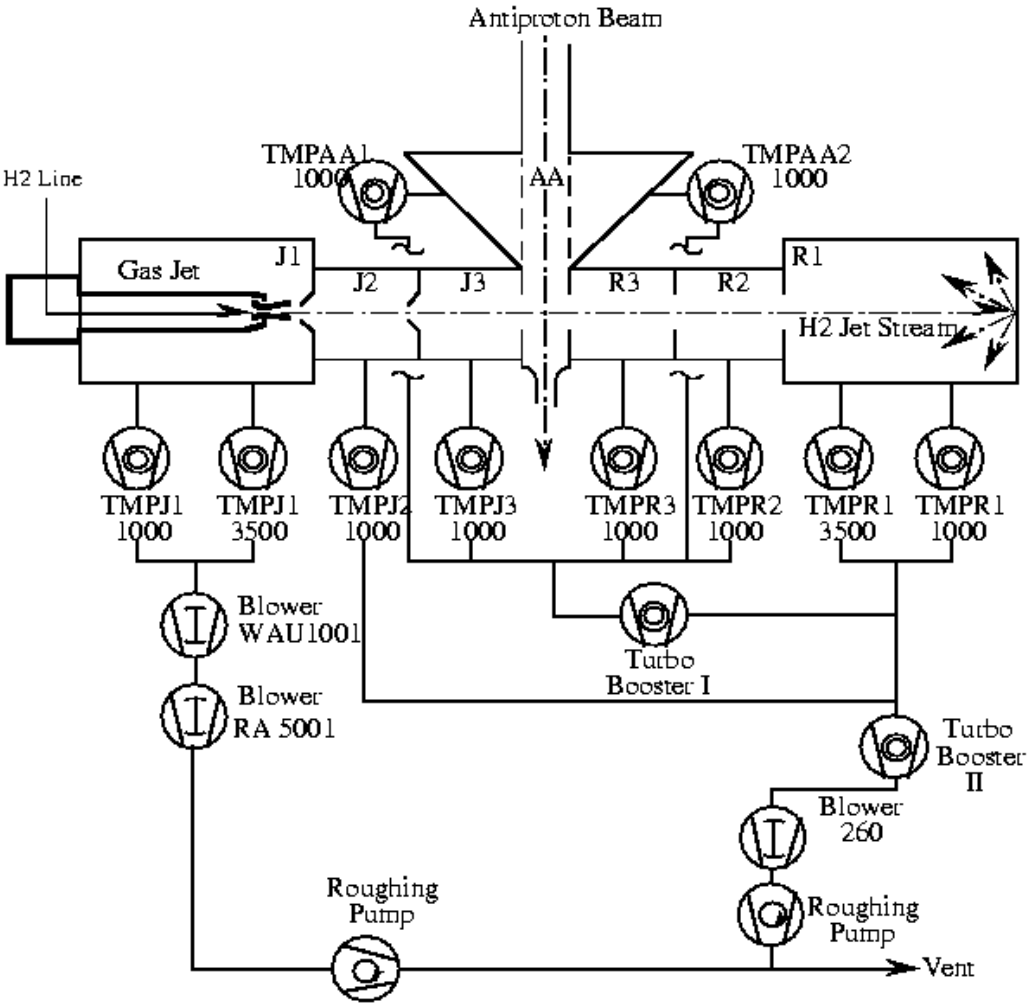

Figure 3.3: Vacuum chambers and pumping system of the jet target.

the antiproton current circulating in the accumulator. The number of antiprotons in the beam decreases over the course of a data taking period; the jet target system can vary the density of the jet so that the instantaneous luminosity is maximized over a run. The achievable range of H_2 density as a function of T and P is shown in fig. 3.4.

3.3 The inner tracking detectors

The charged particle tracking provides a measurement of the θ, ϕ angles, and a fast topological pattern recognition employed by the charged trigger. The components of this system are shown in fig. 3.5; they are:

- the scintillator counters H1, H2' and H2
- the inner (SCI) and outer (SCO) straw chambers
- the inner (SFI) and outer (SFO) scintillating fiber trackers

3.3.1 The hodoscopes H1, H2', H2 and the veto counter

The hodoscope H1 is made up of 8 NE110 scintillator strips placed around the beam pipe. Each element covers 45° in ϕ[1] and is 10 cm long, which allows for a $9° \div 65°$ coverage in θ[2]. The scintillator thickness is $2mm$. The photons from each element are collected by a light guide and sent to a photomultiplier. A single minimum ionizing particle yields between 10 and 20 photoelectrons.

[1]The ϕ angle is measured in reference to the x axis defined by the hydrogen jet direction, as shown in fig. 3.5

[2]The θ angle is defined with respect to the direction of the antiproton beam. In fig. 3.5 this direction is perpendicular to and entering the page.

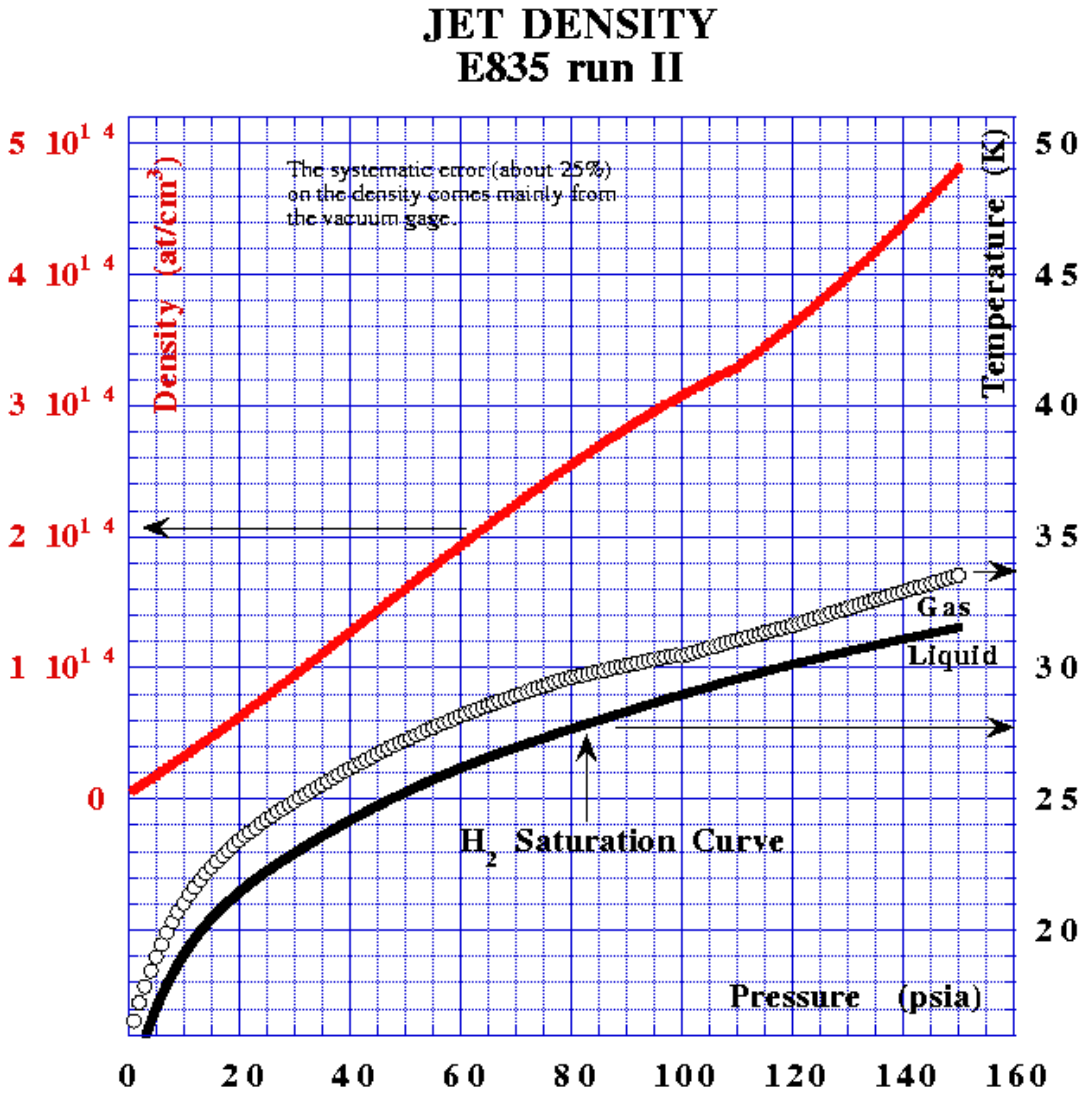

Figure 3.4: Cluster density as a funcion of $P(psia)$ and $T(K)$

The hodoscope H2' consists of 24 elements of scintillator material, $40.8cm$ long and $3mm$ thick, each covering $15°$ in ϕ and $9° \div 65°$ in θ.

H2 has 32 scintillator elements, $60cm$ in length and $4mm$ thick. Each covers $11.25°$ in ϕ and $15° \div 65°$ in θ. The light yield is about $50 \div 100$ photoelectrons per minimum ionizing particle. H2 and H2' provide a measurement of dE/dx, used to distinguish between a single charged track and two close-by tracks.

The hodoscopes are used in the charged trigger. A coincidence between an H1 element and one of the four corresponding H2 elements defines a "charged particle" for the trigger system. A coincidence between an H1 element and H2' provides a veto signal for the neutral trigger.

An additional hodoscope counter forms the endcap of the inner detector system; it is a set of 8 scintillator elements placed perpendicularly to the beam pipe, covering the whole azimuthal angle. It is used as a charged veto in the region where θ is less than $12°$.

3.3.2 The straw chambers

This subdetector provides a measurement of the azimuthal angle ϕ. There is an inner chamber and an outer chamber (SCI and SCO respectively in fig.3.5); each chamber is composed of two layers of 64 staggered tube-like proportional drift chambers. The gas used to operate the chambers is a $82 : 15 : 3$ mix of $Ar : C_4H_{10} : (OCH_3)_2CH_2$, at 1320(1530) V for the inner(outer) chamber. The acceptance region in polar angle is $15° < \theta < 58°$ for SCI and $15° < \theta < 65°$ for SCO.

The detection efficiency with both layers was measured at 97%, while on a single layer was 90%. The resolution in the measurement of ϕ was estimated to be $\sim 9\ mrad$.

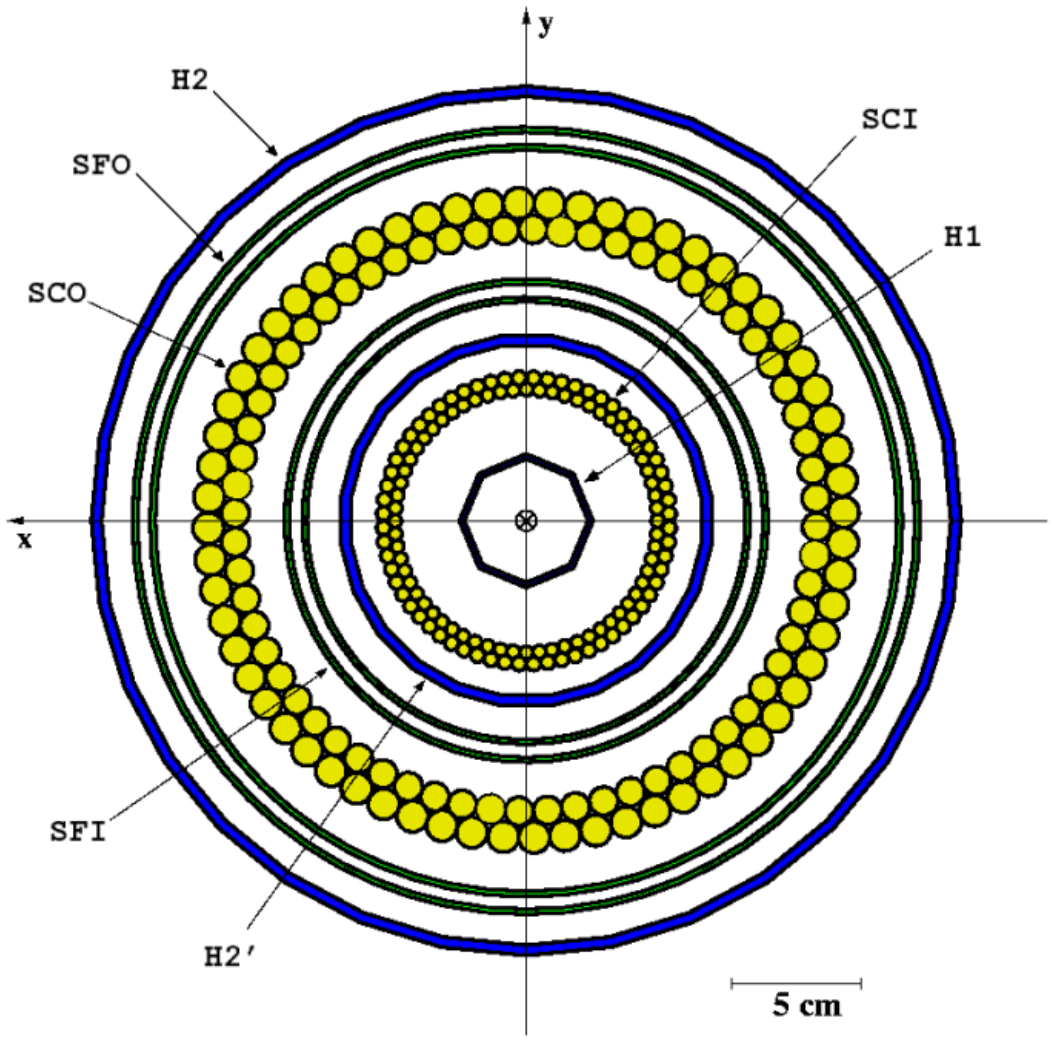

Figure 3.5: Frontal view of the inner tracking subdetectors.

3.3.3 The scintillating fiber tracker

This detector is used to measure the polar angle θ. It is also present in the trigger decision for the $\eta_c \to \phi\phi$ channel.

The SF tracker comprises an inner (SFI) and an outer (SFO) detector. Each detector is made of two layers of scintillating fibers Kuraray 3HF; these fibers are made of polistyrene with pTp as active material. The fibers rest on two cylindrical plexiglass supports. The light emitted by each fiber when hit by a charged particle is transported to the photodetectors by means of non-scintillating fibers (same type as the scintillating ones, but not treated with pTp). Some geometrical parameters of the detector are reported in table 3.1.

Subdetector	Radius (cm)	# fibers	θ coverage
SFI	8.5÷9.2	240	$15° \div 55°$
SFO	14.4÷15.1	430	$15° \div 65°$

Table 3.1: Geometrical characteristics of the scintillating fiber tracker.

The general layout of the detector and the path of the collected light to the photodetector is shown in fig. 3.6. The devices used to convert the fiber light output into an electric charge signal are called *Visible Light Photon Counters*, or $VLPC$s. A $VLPC$ is a semiconductor photodetector with gain $\sim$ 15000 and high quantum efficiency (70% at $\lambda = 550nm$); they operate at a temperature of about 6.5 K, and therefore are contained in a liquid He cryostat. Each signal from a $VLPC$ is amplified, split and sent to an ADC and, after discrimination, to a TDC. Signals from fiber bundles are used in the trigger decision for the $\phi\phi$ channel.

The efficiency as a function of the polar angle is very high, close to 100% between 15° and 45°, and decreases at larger angles but staying above 80%. The intrinsic

resolution of the detector depends on the polar angle and is in the range $1 \div 4\ mrad$.

A detailed description of this detector can be found in [28].

3.4 The Čerenkov counter

The Čerenkov counter is a threshold gas counter used to distinguish between $e^{\pm}$ and other charged particles, mostly hadrons such as $\pi^{\pm}$. It covers 360° in ϕ and between 15° and 65° in θ. A side view of the Čerenkov counter appears in fig. 3.7. In order to optimize the thresholds for e/π separation and $e^{\pm}$ detection there are two separate θ regions where gases with different refractive index are used. CO_2 ($n = 1.000410$) is used in the forward region, between 15° and 38° and Freon 13[3] ($n = 1.000720$) is used in the backward region, for $34° < \theta < 65°$. The π thresholds are 4.873 GeV in the forward region and 3.677 GeV in the backward region. The azimuthal angle coverage is divided in 8 sectors; the Čerenkov light generated in each sector and section by the charged particles is directed to a photomultiplier by means of converging mirrors. The signal from the photomultiplier is amplified by a factor ~ 10 and split in two; half is sent to an ADC and the other half is sent to the trigger logic. The detection efficiency for a single electron was estimated to be $\epsilon = 98.1 \pm 0.5\%$. For an accurate description of the detector refer to [32].

3.5 The central calorimeter

The energy of the electromagnetic showers from $e^{\pm}$ and γ are detected by the central calorimeter (CCAL). This detector is composed of 1280 lead-glass Čerenkov

[3]Freon 13 was used in the year 2000 run of E835 and during the last month of the 1996-97 run; Freon 12 was used for the rest of the '96-'97 data taking.

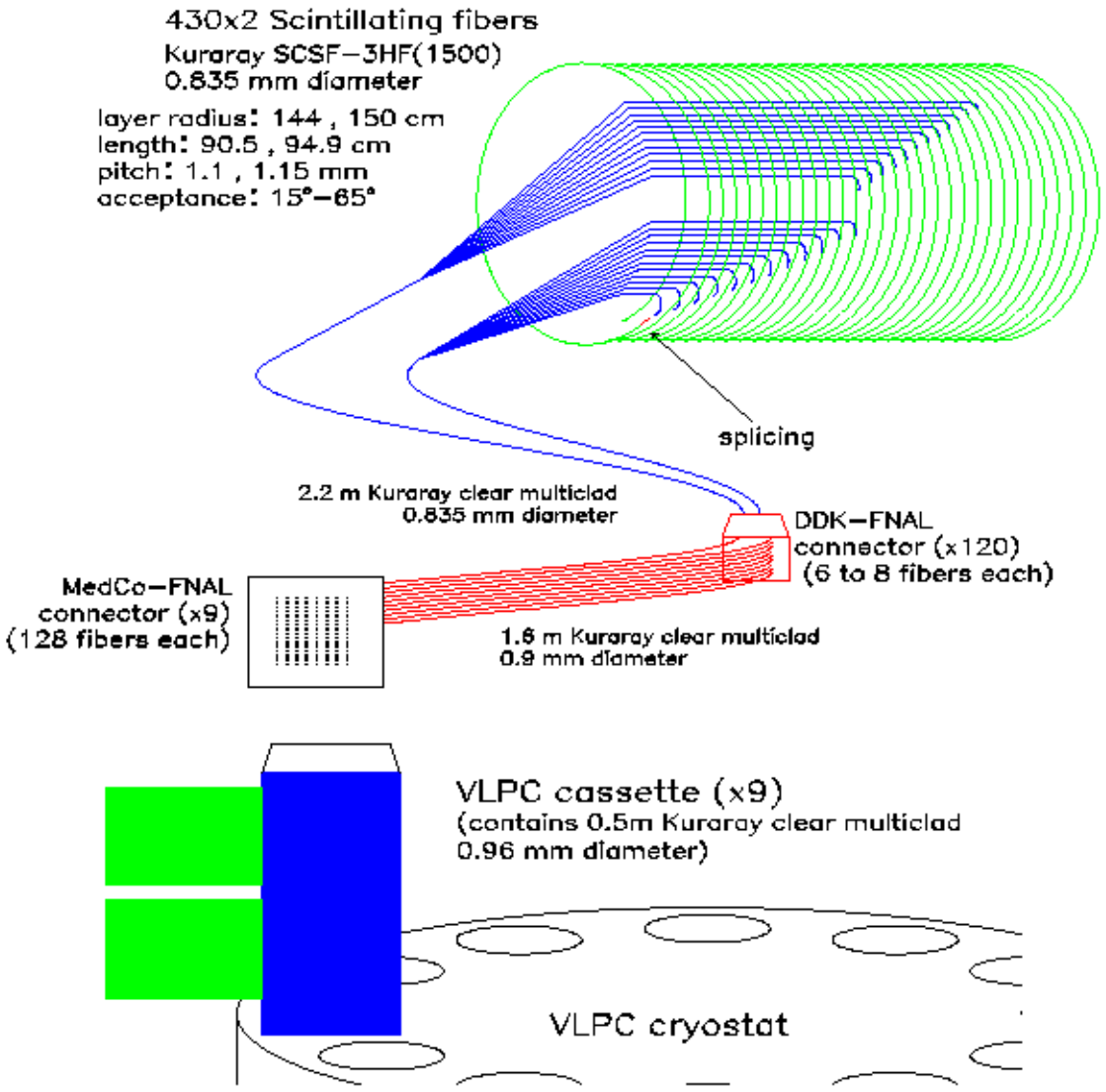

Figure 3.6: General view of the scintillating fiber detector, with path from the scintillating fibers to the VLPCs.

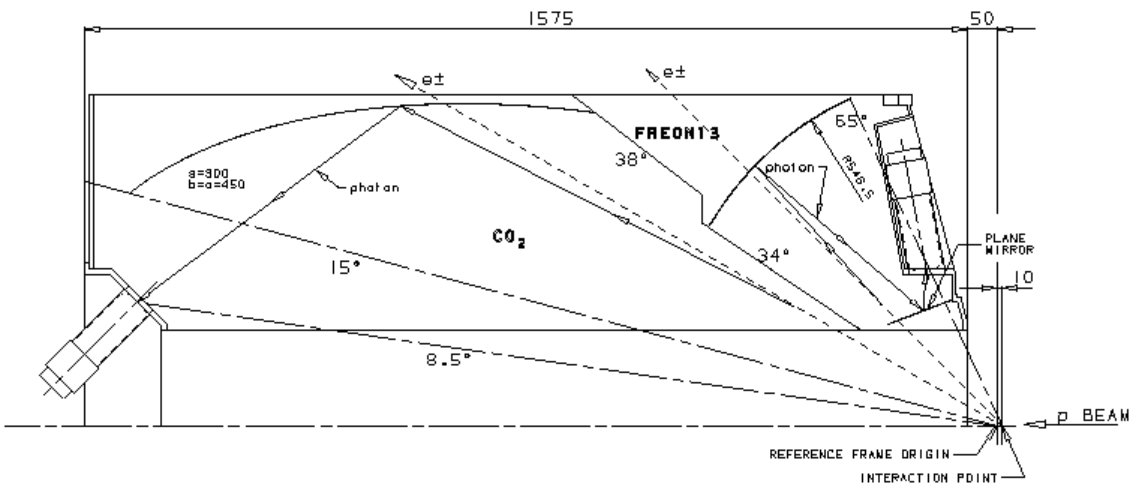

Figure 3.7: Side view of a Čerenkov counter octant, with the CO_2 and $Freon$ sectors in evidence. Dimensions are expressed in mm.

counters read out by means of photomultipliers. An outline of the structure is presented in fig. 3.8. The coverage in ϕ is 360° and in θ is $10.6° \div 70°$; this represents about 70% acceptance for charmonium decays.

The granularity of the detector is evident from fig. 3.8; there are 64 *wedges* in ϕ and 20 *rings* in θ. This choice was made based on the opening angle of the two photons in a symmetrical π^0 decay, so that two distinct clusters would be produced in CCAL at the highest production energy. Each block is made of *Schott Type F2* lead glass, with 42.2% lead, a density of 3.61 g/cm^3, radiation length 3.141 cm and refractive index 1.651.

The geometrical dimensions and positions of the CCAL blocks are reported in table 3.2. Each counter points towards the interaction region, so that it is possible to use CCAL for a fast topological event analysis. The length of each block was chosen to contain $90 \div 95\%$ of the $e.m.$ shower while minimizing losses due to light transmission.

The photomultipliers used in CCAL are built by *Hamamatsu*, and they are of

different diameters depending on the lead-glass block size. Rings $1 \div 14$ are equipped with $3''$ R3036-02, rings $15 \div 16$ with $2.5''$ R3345-02, rings $17 \div 18$ with $2''$ R2154-04 and rings $19 \div 20$ with $1.5''$ R580-13.

The signal from each PMT is delayed by 300 ns cables to the readout electronics of the CCAL to allow the trigger enough time for event processing. The transmission through coaxial cable degrades the signal introducing a 600 ns tail; such tail may interfere with an event happening close enough in time, generating a so called *pile-up* event, where two consecutive events are partially superimposed. A *signal shaper* circuit board is used to narrow the pulses and substantially reduce the tails so that a short (about 100 ns) ADC gate can be used. After shaping, the signal is split and a part of it is sent to an ADC; the rest goes to a discriminator and then to a TDC. Further details on the shaper boards can be found in [72].

Gain shifts in CCAL blocks are monitored by means of a system based on a Nitrogen laser and optic fibers. The light from the laser, with a peak wavelength of 337 nm, is directed on a scintillator to produce visible light. By means of a lucite bar the laser light is distributed equally to 64 optic fibers, which are then used to carry the light to each CCAL wedge; another lucite bar splits the light signal, which is brought to each of the 20 blocks in the wedge with optic fibers. Photodiodes measure the light output from the laser, so that a comparison with the CCAL block response can be made. The laser system is also used to calibrate the energy measurement of each counter; the method used will be described in a following chapter.

The energy resolution of the CCAL was measured by E760, the predecessor experiment of E835, and was found to be [34]:

$$\frac{\sigma(E)}{E} = \frac{6.0\%}{\sqrt{E(\mathrm{GeV})}} + 1.4\% \tag{3.7}$$

The position resolution of the electromagnetic shower centroid was also measured in [34], giving an average rms error of 9 mm. Taking into account the uncertainty in the position of the interaction vertex, the angular resolutions were measured and found to be 6 $mrad$ for θ and 11 $mrad$ for ϕ.

Block	Length (L_R)	θ (deg)	$\Delta\theta$ (deg)	ρ (cm)	A_{PMT}
1	12.03	67.387	5.226	72.44	0.473
2	12.30	62.259	5.031	75.87	0.475
3	12.70	57.342	4.803	80.07	0.476
4	13.21	52.664	4.552	85.08	0.478
5	13.86	48.246	4.284	90.96	0.479
6	14.65	44.101	4.007	97.79	0.481
7	15.59	40.234	3.728	105.62	0.482
8	15.92	36.644	3.451	114.54	0.497
9	15.92	33.327	3.183	124.66	0.520
10	15.92	30.273	2.925	136.07	0.544
11	15.92	27.472	2.679	148.89	0.568
12	15.92	24.908	2.449	163.26	0.593
13	15.92	22.567	2.233	179.34	0.617
14	15.92	20.434	2.033	197.28	0.641
15	15.92	18.493	1.848	197.29	0.546
16	15.92	16.730	1.678	197.29	0.664
17	15.92	15.130	1.522	197.30	0.527
18	15.92	13.679	1.380	197.30	0.644
19	15.92	12.364	1.250	197.30	0.443
20	15.92	11.174	1.131	197.30	0.543

Table 3.2: Positions and dimensions of lead-glass blocks in a single axial segment (wedge); for each block we report the length in units of radiation length, the polar angle θ of the block center, the coverage $\Delta\theta$, the distance ρ from the target to the front face of the block, and the ratio of the areas of the photomultiplier face and the back face of the block A_{PMT}.

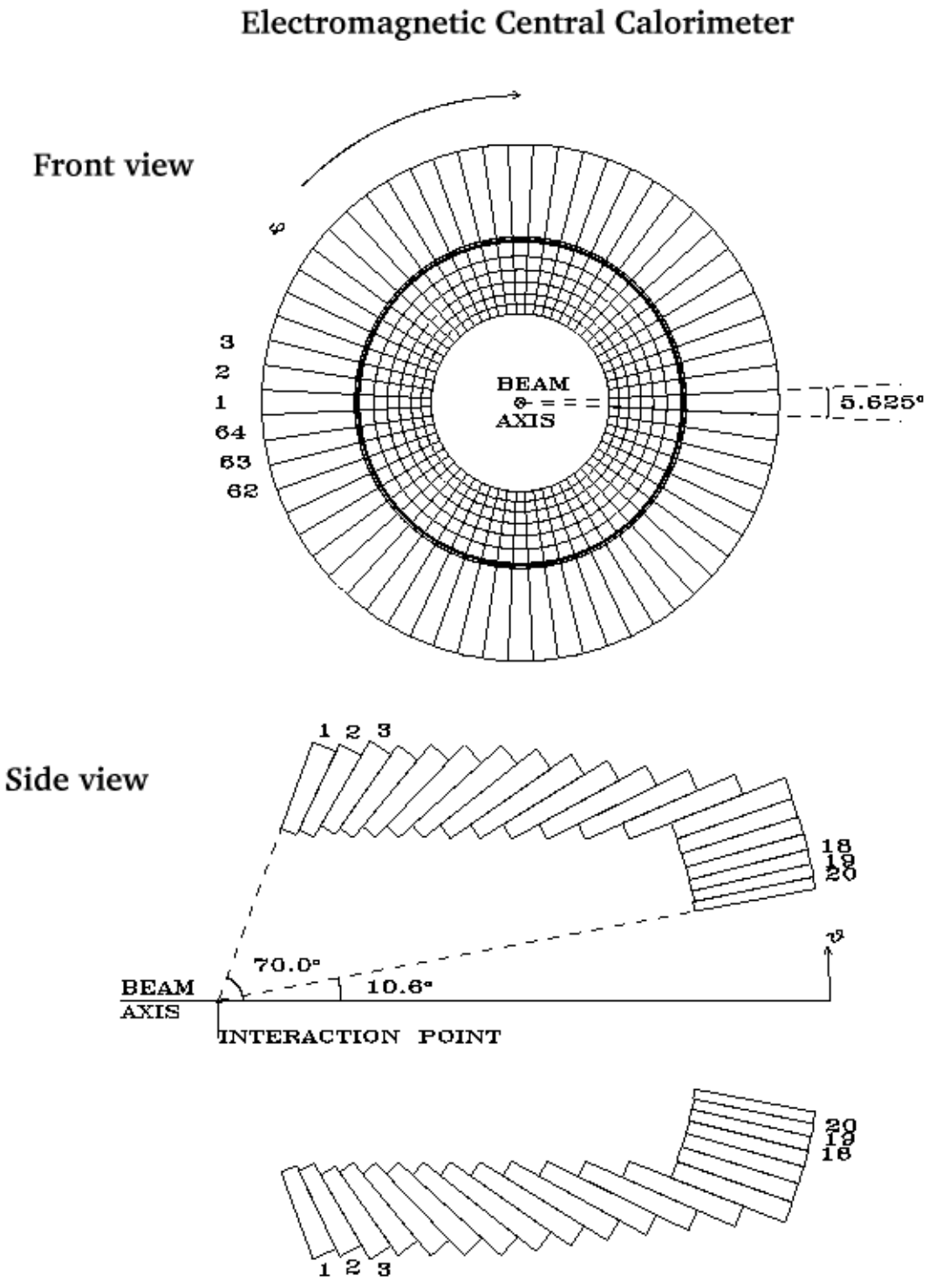

Figure 3.8: Layout of the lead glass blocks in the CCAL structure.

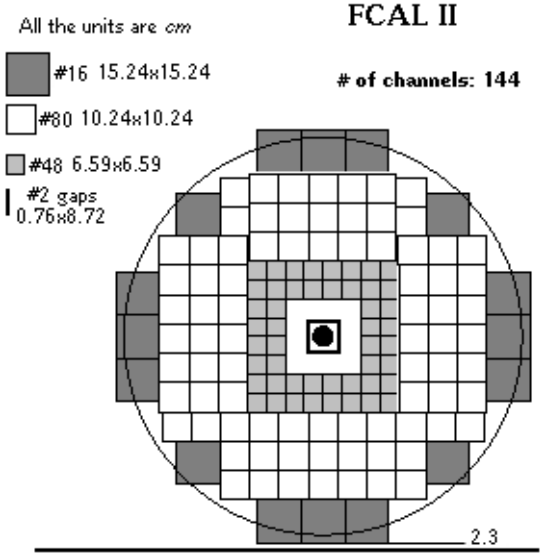

Figure 3.9: Front view of the forward calorimeter. The areas outside the circle overlap with the central calorimeter.

3.6 The forward calorimeter

The forward calorimeter (FCAL) covers the angular region $2^\circ < \theta < 10^\circ$ and is used almost exclusively as a veto. It is an array of 144 lead-glass *Schott F2* Čerenkov counters, shown in fig. 3.9. The array structure is dictated by the sizes of the lead-glass blocks; there are three block sizes, corresponding to 13, 14 and 21 radiation lengths. Like for CCAL, a photomultiplier is directly coupled to the lead-glass block with optical glue. The readout electronics consists of a setup identical to that used for CCAL. The energy resolution is:

$$\frac{\sigma(E)}{E} = \frac{6.0\%}{\sqrt{E(\mathrm{GeV})}} + 4\% \tag{3.8}$$

3.7 The luminosity monitor

The instantaneous and integrated luminosity are measured with the elastic $\overline{p}p \to \overline{p}p$ process. The cross section σ for the $\overline{p}p$ elastic scattering is well known [40], and is the sum of Coulomb, nuclear and interference contributions. The number of scattered protons N is related to the instantaneous luminosity through

$$N = \mathcal{L}_{ins} \frac{d\sigma}{dt} \frac{dt}{d\Omega} d\Omega \tag{3.9}$$

where t is the squared momentum transfer and $d\Omega$ is the solid angle covered by the detector. By measuring N we can evaluate $\mathcal{L}_{ins}$. The luminosity monitor consists of three solid state detectors placed under the beam line, at a polar angle $\theta \sim 86.5°$. The central detector lies right below the beam while the other two are placed symmetrically on either side, as shown in fig. 3.10. The side detectors are used to monitor horizontal beam displacements. The measured differential cross section is shown in fig. 3.11. The dominant source of error in measuring $\mathcal{L}_{ins}$ is in the differential cross section and is estimated to be less than 2.5% [72].

3.8 The trigger system

The task of the trigger system is to perform a rapid analysis of an event and make a decision as to whether the event is to be kept for further analysis or is to be rejected. The trigger consists of two levels: the 1^{st} *level trigger* is a hardware trigger, it has a decision time of about 100 ns and it uses information from the hodoscopes, the scintillating fiber detector, the Čerenkov counter and the central calorimeter; the 2^{nd} *level trigger* is a software selection which runs on the data acquisition microprocessors. The 1^{st} level trigger makes separate decisions for events with charged or all neutral

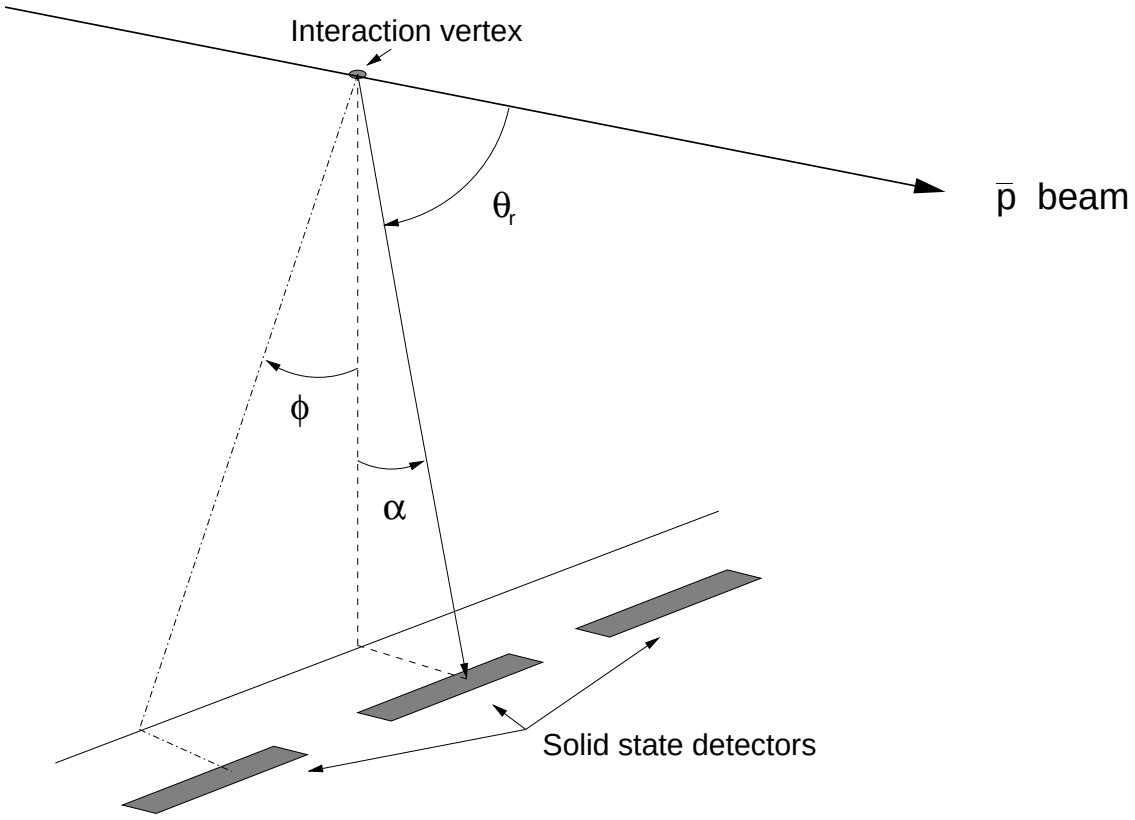

Figure 3.10: Schematic view of the luminosity monitor; the angle θ_r indicates the polar recoil angle of the proton.

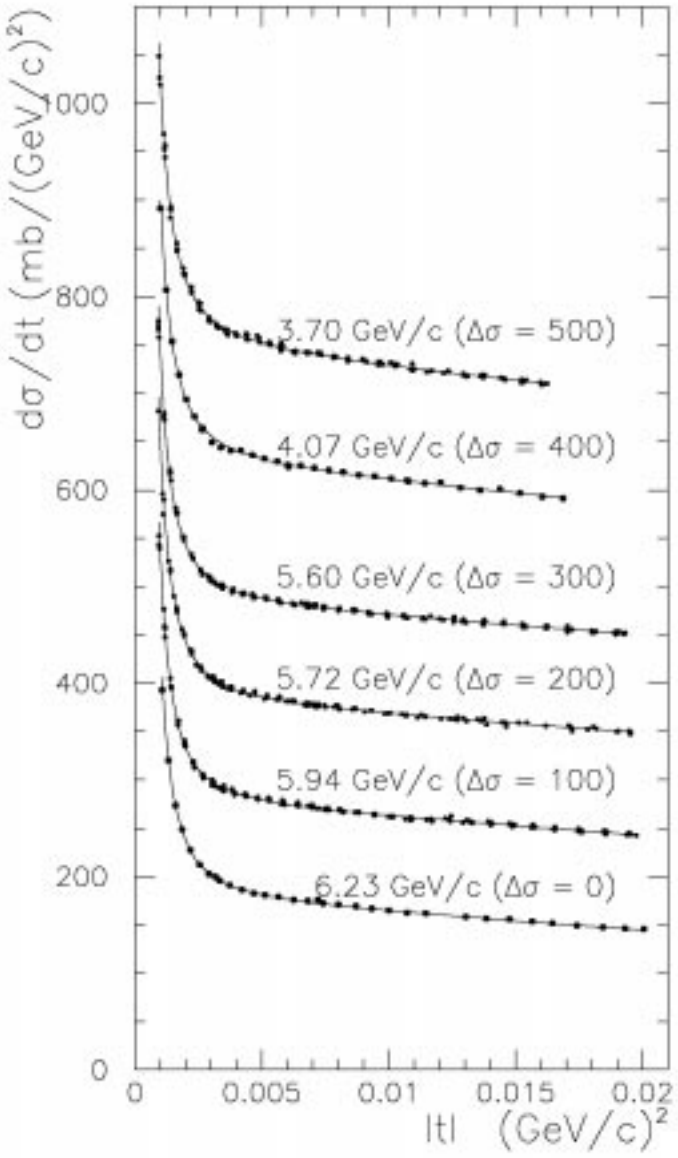

Figure 3.11: Measured differential cross section for six different beam momenta, with lines fitting the data [40].

final states; these decisions are passed to the 2^{nd} level trigger, along with a random trigger used to evaluate the effect of accidental events during offline analysis.

3.8.1 The charged trigger

The detectors used to form the charged trigger decision are: H1, H2', H2, forward veto, scintillating fiber detector and Čerenkov counter. The signals from the detectors are sent to discriminators, then to a single logic stage and to a final trigger stage. The single logic stage produces trigger decisions of the following types:

- *multiplicity*: the number of particles in the final state is counted through the number of H2 and scintillating fiber detector hits
- *coplanarity*: this is the coincidence of an H2 element and one of the three opposite elements in ϕ
- *track reconstruction*: the output of this logic is based on a topological analysis of the event, and establishes number (1 or 2) and type (electrons or hadrons) of particles
- $\phi\phi$ *logic*: this trigger was developed to detect events from $\overline{p}p \to \overline{c}c \to \phi\phi \to 4K^{\pm}$. It detects a coincidence between an H2 element hit and any other H2 hit within a back-to-back region 80° wide centered about the axis connecting the H2 element and its opposite; there must be no hits outside of this region. It also examines the coincidences in the scintillating fiber detector bundles and checks their compatibility with the $\phi\phi$ kinematics.
- *neutral veto*: coincidence between an H1 element and the corresponding H2' elements, plus the OR of the elements of the forward charged hodoscope. It is used as a veto for the neutral trigger.

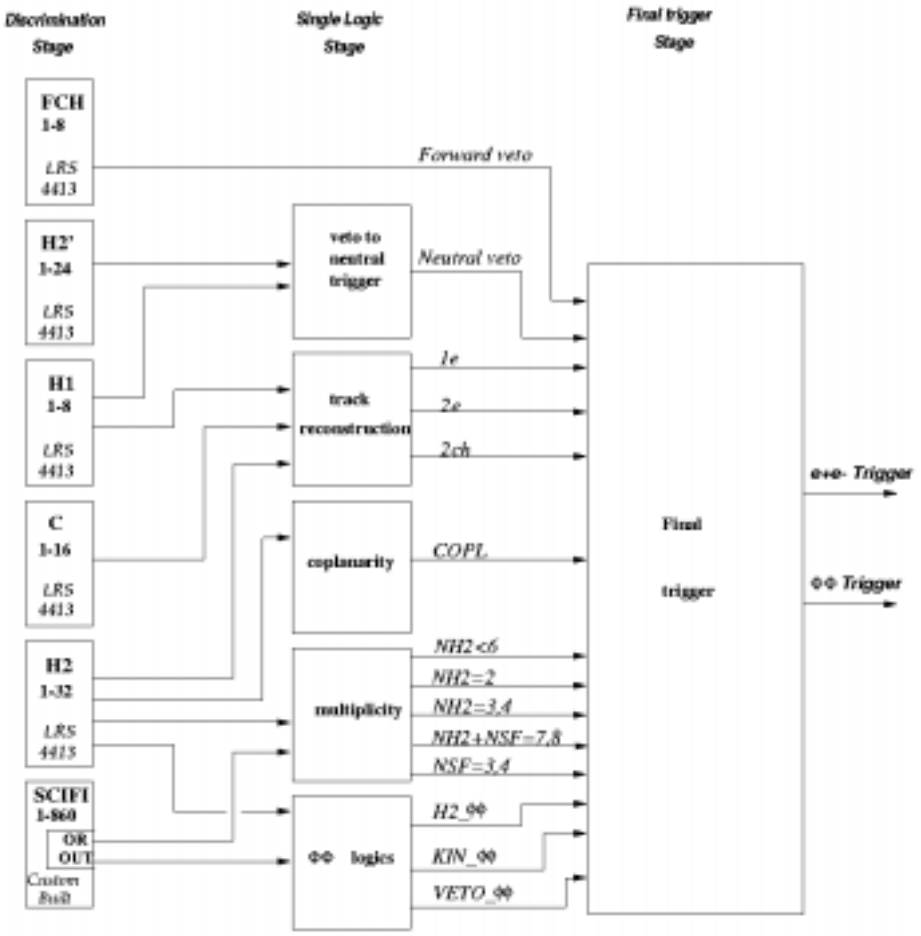

Figure 3.12: Charged trigger system layout.

The final trigger stage consists of CAMAC memory lookup modules. The charged trigger uses two such modules: the C_MLU and the Φ_MLU. C_MLU gathers the outputs of the single logic stage for events with e^+e^- in the final state, whereas Φ_MLU is dedicated to the $\phi\phi$ channel. The output from these modules is strobed by the OR of the H2 signals, and it is directed to a master module, the M_MLU, which provides the final logic signals for e^+e^- and $\phi\phi$ events. The layout of the charged trigger system is shown in fig. 3.12 and fig. 3.13.

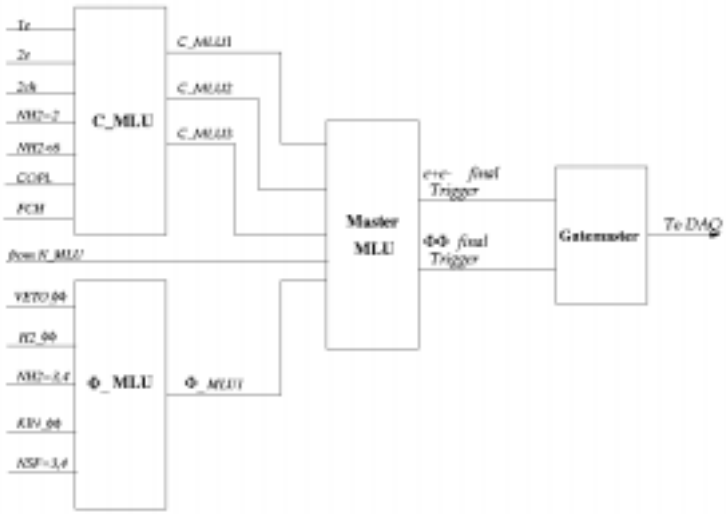

Figure 3.13: Inputs to the trigger final stage and M_MLU outputs.

3.8.2 The neutral trigger

The neutral trigger relies on information from the CCAL; 5% of the signal from the shaper boards is used for the neutral trigger logic. Rather than on the individual CCAL channels, the trigger decision is made based on sums of channels, called *super-wedges* and *super-blocks*, shown in fig. 3.14. A *super-wedge* is defined as a group of 9 adjacent counters within a CCAL ring; the signal from a super-wedge is the sum of the signals from each of the 9 counters. From a total of 20 rings and 64 wedges in CCAL we have 160 super-wedge signals distributed in 8 octants. The outer blocks of each super-wedge overlap with the adjacent super-wedges, in order to maximize the efficiency. A part of the super-wedge signal is discriminated and the other summed in the ring direction. The OR of all the super-wedges is called PBG_{OR} and is used as the minimum bias signal. The super-wedge signals within an octant are summed in groups of 5 adjacent rings, so as to obtain 5 *super-blocks* for each octant. The

super-blocks overlap by 2 blocks in θ and ϕ (except for the super-blocks formed with rings $1 \div 4$, as shown in fig. 3.14). The signal from each of the 40 CCAL super-blocks is integrated and discriminated, then sent to the neutral MLU. The N_MLU output consists of 4 logic signals:

- PBG1 is used to trigger events with two back-to-back energy deposits, in opposite CCAL sectors; it is used for two body decays.
- PBG3 requires two energy deposits; one deposit must be in one of the three opposite CCAL sectors with respect to the other energy deposit. It is used for two body inclusive decays.
- E_{tot}^{low} is formed by summing the energy from all the octants, requiring that the total energy deposited in CCAL be above 70% of the total available energy. This logic is used to evaluate the efficiency of the two previous logics and to trigger multi-photon events.
- E_{tot}^{high} is the same as above with a threshold of 80% of the total available energy.

Fig. 3.15 shows the layout of the neutral trigger.

3.9 The data acquisition

The E835 data acquisition is based on an integrated system of software packages called *DART* (Data Acquisition for Real Time systems [21]), developed at Fermilab by a collaboration between the F.N.A.L. Online Systems Department and the experiments that used this software during the 1996-1997 fixed target run. The hardware is based on the CAMAC/FASTBUS standards; in E835 the software has been developed

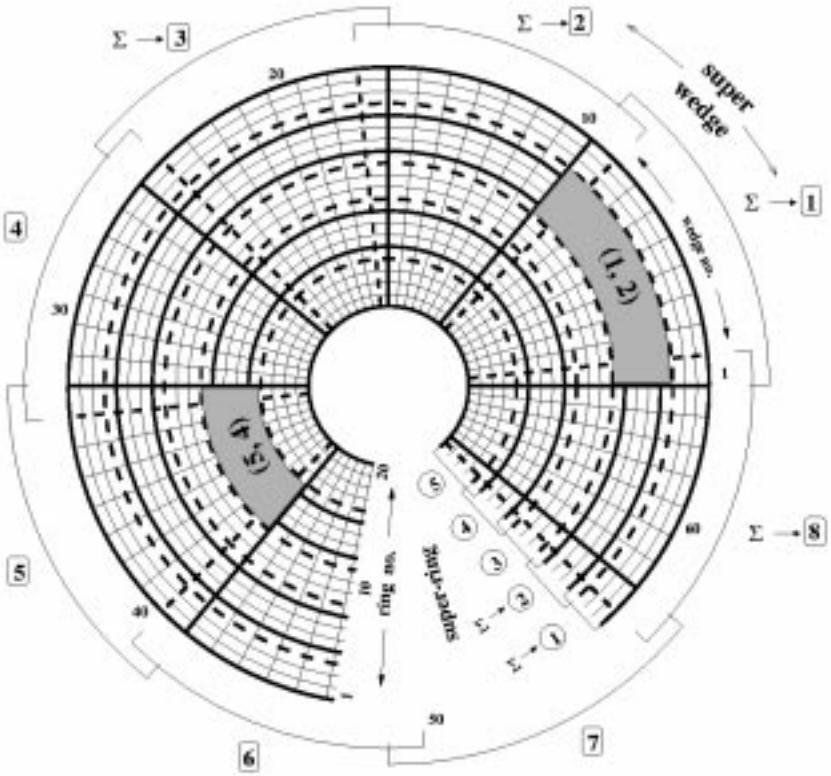

Figure 3.14: Sums of CCAL blocks. Super-rings and super-wedges are delimited by dashed lines; the shaded areas indicate two super-blocks.

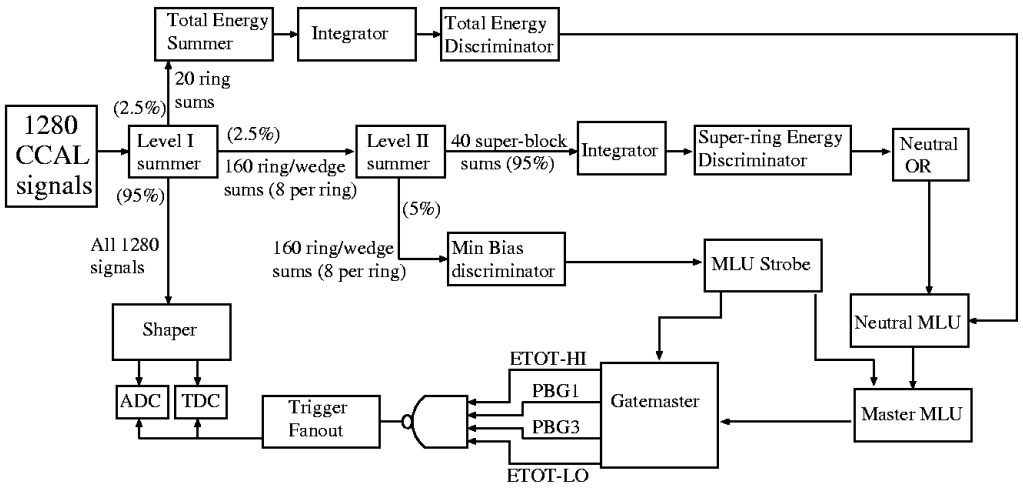

Figure 3.15: Diagram of the neutral trigger logic. The percentages of the signal sent to a logic module are indicated in parentheses.

for SGI Challenge multi-processor and SGI Indigo. The system is designed to handle a 6 kHz trigger rate with almost no deadtime.

3.9.1 The hardware setup

The E835 data acquisition layout is shown in figure 3.16. The signals from the detectors are read out by CAMAC modules (LeCroy LRS 4300/4300b ADCs and Lecroy 3377 TDCs). The ADC and TDC modules fill 17 CAMAC crates, arranged in 3 branches (one serial and two parallel) and controlled by an SGI Indigo through two SCSI Jorway 411 Branch Controllers. The collection of the output of the CAMAC modules is organized in 4 streams distributed among 18 DYC+ modules and 23 CAMAC controllers. The DYCs are intermediate data buffers that retain data in their 32-bit FIFO until the whole event is read; when the event reading is over it sends the data to 6 Dual Ported Memories MM-6390 (DPMs) through two pairs of Access Dynamics DC2/DM115 modules which control the access to the DPMs. Each

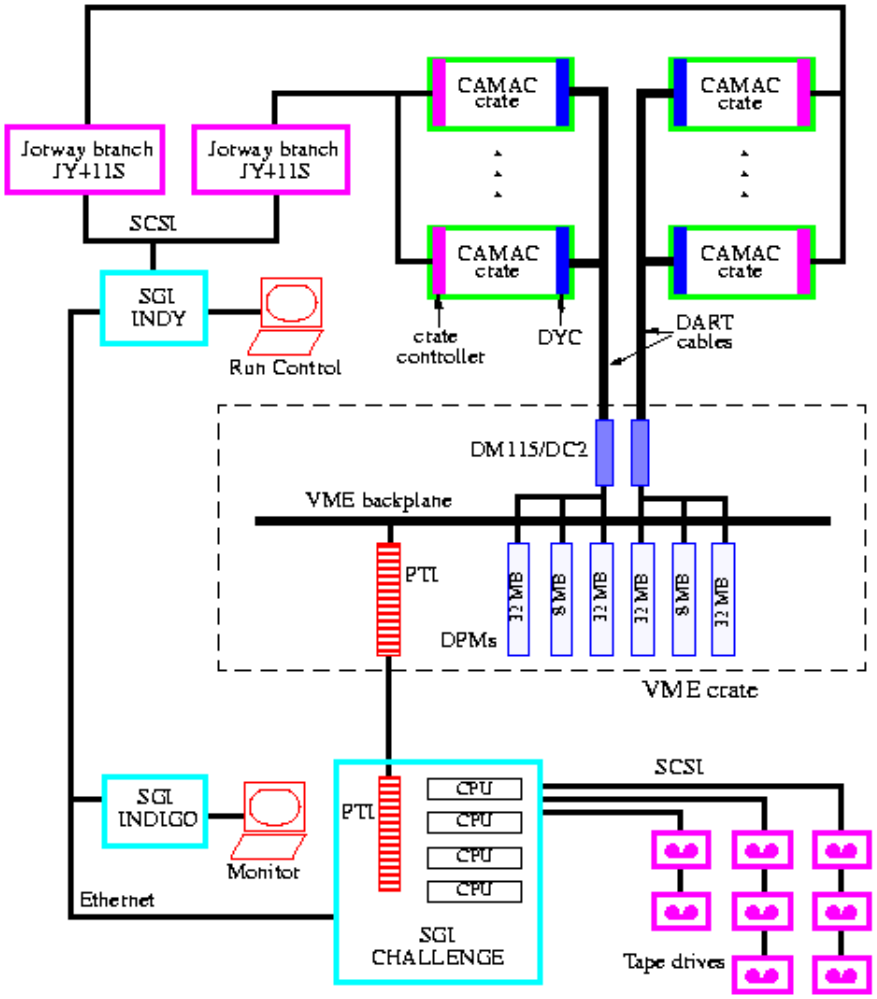

Figure 3.16: Hardware layout of the E835 data acquisition.

DYC serves one crate of ADC/TDC modules. The DYCs are daisy chained together and they read the data from the CAMAC modules enabling the readout via a PASS signal sent along the chain. During the readout of the modules the DYCs issue a BUSY signal that prevents further triggers from the trigger logic modules. Each DYC can simultaneously receive data from the CAMAC modules and send data via RS-485 cable to the DC2/DM115; the transmission is controlled by a permit token issued by the DC2/DM115 to the DYC and a WAIT signal issued by the destination buffer. Upon finishing the transmission of the event header and the event data the DYC passes the transmission token on to the next DYC in the chain.

There are two 32 Mb DPMs and one 8 Mb DPM where the DC2/ DM115 writes data using a 'ping-pong' algorithm. This is done by means of a process running on a Challenge called *gateway*. The gateway reads data from one of the two 32 Mb DPMs (the 'ping' memory) while the DC2 is writing to the other DPM (the 'pong' memory). The gateway and the DC2 use the 8 Mb DPM as a 'mailbox' to exchange information about the use of the two 32 Mb DPMs. When either one of the two processes is working with a DPM a message is left on the 'mailbox' to signal to the other process that the DPM is being read/written to. When a process has finished using a DPM it writes a 'release' message on the mailbox and it starts polling for an analogous message from the other process until they switch DPMs. This way the data transfer of the DC2 or the gateway is not interrupted by the other process polling directly for a 32 Mb DPM. The gateway process writes data to a shared memory area of the Challenge; the online filters running on each CPU of the Challenge read from this area and start processing the event, as described in the next section.

Beam parameters like beam position, intensity, longitudinal frequency spectrum, emittance, and other control data like magnet currents, magnetic field strengths and jet target parameters are monitored by the Accelerator Control NETwork (ACNET)

system. The computer with the ACNET data sends its information to the E835 run control computer for logging and monitoring.

3.9.2 Event builder and online filter

The online filters take the gateway buffers and build the event checking synchronization numbers of the DYCs and DPMs, verifying data integrity, adding an event header and performing the online analysis.Event building, classification and logging are provided by *PRUDE* (Program for Rejecting Unwanted Data Events), a software package running on the online computers. PRUDE works as online filter/tagger, software trigger/level 2 trigger; it performs a basic analysis of the detector; it sets detector bits and summary variables, and performs a data integrity check in a subset of the events processed. If the event passes the trigger (upon comparison of the bit map of the event with acceptable bit masks) summary variables are put in an array appended to the raw data buffer. This new buffer is then assigned to the appropriate stream for logging to tapes/disk and to the monitor/display computer. The PRUDE software performs a fast online analysis of the event using information from the detectors; the type of analysis depends on the level 1 hardware trigger type. The analysis performed by PRUDE are:

- CCAL analysis: PRUDE finds local energy maxima in the CCAL (blocks with an energy deposit of at least 37.5 MeV and larger in energy than any of the 8 nearest neighbors) and forms a cluster of 3x3 blocks around the local maximum. Then the energy of the 9 blocks is summed to obtain the cluster energy, which is used to determine the θ and ϕ with an energy weighted average over the 9 blocks of the cluster. The invariant mass of the cluster is also calculated. These clusters are used to determine the invariant mass of large energy deposits in

CCAL and to find events including π^0, η and $\overline{c}c$.

- e^+e^- analysis: counts hodoscope coincidences, identifies pairs of candidate electrons using information from CCAL analysis and Cerenkov counter; it identifies channels like $\overline{p}p \to e^+e^-$ and $\overline{p}p \to J/\psi X \to e^+e^-X$.

- $\phi\phi$ analysis: checks topology of event based on counters, straw chambers and scintillating fibers information to look for events $p\overline{p} \to \phi\phi \to 4K$.

Chapter 4

Analysis

The method used to perform the measurement of the ψ' branching ratios will be described in this chapter. Since such method involves normalizing the number of events collected for a specific ψ' channel to the number of $J/\psi X$ events, a key point in the measurement of the ψ' branching ratios is the accuracy in the evaluation of the detection efficiency for each exclusive decay relative to the efficiency for the $J/\psi X$ decay. In this chapter we will focus on the selection criteria of the candidate events and determination of the selection efficiency for each channel. We will estimate background levels and obtain the raw number of events for each channel. We will describe the selection of the event sample for the measurement of the angular distribution parameter $\lambda(\psi')$, and the measurement procedure.

4.1 Data collection

The data used to measure the ψ' decay parameters considered in this thesis was collected in the run II of E835, in year 2000. A summary with the details relative to the data taking is reported on table 4.1. At the ψ' most of the data taking time was spent around the peak, at $E_{cm} = 3686\ Mev/c^2$; a summary of the data taken at the ψ'

is presented on table 4.2. The data samples are identified as *stacks* and *runs*. A stack is a data sample collected in the life of the antiproton beam inside the accumulator ring. Often within a stack the CM energy is changed several times to perform a scan of a resonance; a run is a data sample taken at a given energy. Typically a run corresponds to an integrated luminosity of about $50 \div 400\ nb^{-1}$. Some of the data collected are not used in this analysis, due to detector problems which affected the quality of the data. Such problems include:

- missing data from straw chambers and VLPC subdetectors: in stack 1 runs 5009-5012 ($\int \mathcal{L}dt = 81.6\ nb^{-1}$) do not contain straw-chamber information, and VLPC data is missing from runs 5036-5038 ($\int \mathcal{L}dt = 82.6\ nb^{-1}$)

- off-orbit antiproton beam: during most of the data taking in stacks 5 and 6 ($\int \mathcal{L}dt = 643.0\ nb^{-1}$) part of the beam was not on the central orbit and the measured beam Schottky noise spectrum showed 2 peaks; therefore the measured beam parameters are not representative of the beam energy distribution

Resonance	Integrated luminosity (pb^{-1})	E_{cm} range (MeV)
χ_0	32.9	3340.0 - 3470.0
χ_1	5.98	3509.6 - 3511.7
χ_2	1.12	3535.0 - 3557.9
$^1P_1$	50.5	3523.3 - 3528.9
ψ'	15.1	3666.0 - 3704.0
High energy	7.27	3770.0 - 4270.0

Table 4.1: Summary of data taken during the run II of E835

Stack	E_{cm} (MeV)	$\int \mathcal{L}dt$ (nb^{-1})	Run numbers
1	$3685.2 \div 3687.6$	747.7	5006 - 5038
2	3686.1	1008.2	5076 - 5084
5	-	543.0	5235 - 5258
6	-	100.0	5407 - 5432
14	3686.0	991.9	5571 - 5574
29	$3684.4 \div 3686.6$	991.8	5818 - 5837
30	$3686.1 \div 3687.6$	396.2	5840 - 5842
49	3686.1	2566.4	7143 - 7148
50	3686.1	1275.0	7248 - 7252
51	3686.1	2103.2	7254 - 7259
54	$3666.1 \div 3704.9$	4333.7	7269 - 7283

Table 4.2: Data taken at the ψ' energy during the run II of E835; indicated are the stack number, the E_{cm} energy, the integrated luminosity per stack and the run numbers.

4.2 Branching ratio measurement: method

The measured cross section is the convolution of 1.13 with the center of mass energy distribution, which is essentially represented by the antiproton beam spread $G_{beam}(E)$:

$$\sigma_{meas}(E_{cm}) = \int_0^\infty \sigma_R(E')G_{beam}(E_{cm} - E')dE' + \sigma_{bkg}(E_{cm}) \tag{4.1}$$

In principle the branching ratios of the ψ' can be measured directly. At the resonance peak we get, from 1.13, an expression for $B(\psi' \to A)$:

$$B(\psi' \to A) = \frac{\sigma_{peak}}{3\pi}\frac{k^2}{B(\psi' \to \overline{p}p)} \tag{4.2}$$

The quantities on the right hand side of equation 4.2 are all directly measurable, at the CM momentum k. However, expression 4.2 depends on $B(\psi' \to \overline{p}p) = (1.9 \pm 0.5) \times 10^{-4}$ and the convolution with the beam shape brings in a dependence on Γ_R/Γ_{beam}. Since the systematic error on Γ_{beam} is in the range 5-10%, and the branching ratio

to $\overline{p}p$ has a large error, the direct measurement of the branching ratios would not be very precise.

Another approach is possible if we observe that the number N_A of $\psi' \to A$ events we count with our detector is given by:

$$N_A = \varepsilon_A N_{\psi'} B(\psi' \to A) B(A \to final) \tag{4.3}$$

where $N_{\psi'}$ is the number of ψ' produced in the $\overline{p}p$ annihilation and ε_A is the total detection efficiency. For $\psi' \to J/\psi X$ events:

$$N_{J/\psi X} = \varepsilon_{J/\psi X} N_{\psi'} B(\psi' \to J/\psi X) B(J/\psi \to e^+e^-) \tag{4.4}$$

Taking the ratio between 4.3 and 4.4 we obtain:

$$B(\psi' \to A) = \frac{N_A}{N_{J/\psi X}} \frac{\varepsilon_{J/\psi X}}{\varepsilon_A} \frac{B(\psi' \to J/\psi X) B(J/\psi \to e^+e^-)}{B(A \to final)} \tag{4.5}$$

Knowledge of $B(\psi' \to J/\psi X)$ and of $B(J/\psi \to e^+e^-)$ allows us to estimate ψ' branching ratios using formula 4.5. Normalizing detection efficiencies and numbers of events for each channel to the corresponding quantities for $J/\psi X$ also exploits the E835 capability to detect, with high efficiency, final states with a high invariant mass e^+e^- pair.

The channels studied in this thesis are:

- $\psi' \to e^+e^-$
- $\psi' \to J/\psi X \to e^+e^- X$
- $\psi' \to J/\psi \pi^+\pi^- \to e^+e^-\pi^+\pi^-$
- $\psi' \to J/\psi \pi^0\pi^0 \to e^+e^-\gamma\gamma\gamma\gamma$
- $\psi' \to J/\psi \eta \to e^+e^-\gamma\gamma$

The small $\psi' \to J/\psi\pi^0$ branching ratio relative to the amount of data collected does not allow us to separate effectively this channel from the background, therefore it is not examined in this analysis.

4.3 Branching ratio measurement: event selection

The hadronic background in $\overline{p}p$ annihilations is large ($\sigma_{total} \simeq 70\ mb$); the cross sections for the charmonium decays observed by E835 range from picobarns to nanobarns. The signature for charmonium formation consists of electromagnetic final states with two back-to-back charged tracks and/or two back-to-back energy deposits in CCAL. The data written on tape or disk by the online filter (see section 3.9.2) are submitted to an analysis where each of the two candidate e^+e^- from ψ' or J/ψ is associated with a Čerenkov signal and to at least 2 out of 3 hodoscope signals; the invariant mass of the e^+e^- pair is required to be greater than 2.2 GeV. The data subset selected in this manner is written to a set of Data Summary Table (mDST) files. The mDST data are then submitted to two more analysis stages: preliminary, to select candidate $\psi' \to e^+e^-$ and $\psi' \to J/\psi X$ events and reduce the background, and final to assign each candidate to its channel. The CCAL thresholds chosen for this analysis are 25 MeV for the central block and the cluster energy and 120 MeV for the cluster mass. For a definition of CCAL cluster and cluster mass, see appendix C.

4.3.1 Preliminary selection

The purpose of this selection is to obtain a clean sample of candidates for the channels being studied. The mDST files already contain events with high energy e^+e^- in the final state; from this set we need to exclude e^+e^- from γ conversion and Dalitz decays of the π^0. To this purpose we build a test statistic for each $e^\pm$ track

and perform a likelihood ratio test for the signal hypothesis against the background hypothesis. We call this test statistic *electron weight* (ew); information from the hodoscopes, Čerenkov and CCAL is used to build the test. A detailed description of the ew statistic is given in appendix A. The product of the ew for the candidate e^+e^- is shown in fig. 4.1. In our detector the main signature for charmonium resonances is a high invariant mass e^+e^- pair, therefore the product of the ew for the e^+e^- tracks is the quantity on which we cut. The reduction of the non resonant background after applying the ew cut can be appreciated in fig. 4.2. To further reduce the background we also cut on the invariant mass of the e^+e^-, to eliminate the tail below 2.6 GeV. The angular acceptance for e^+e^- is defined by the polar angle region where the Čerenkov counter has high efficiency and by the CCAL geometry; a cut on $\theta_{e^\pm}^{lab}$ is performed to maximize the efficiency on e^+e^- selection. Also, since the e^+e^- energy and angles measured by CCAL are affected by the presence of nearby *e.m.* showers, we require a minimum angle ($OpAng$) between each of the electron tracks and any additional on time tracks. The cuts used in the preliminary selection are:

- electron weight: $ew_{e^+} \times ew_{e^-} > 1.5$
- e^+e^- invariant mass: $m_{e^+e^-} > 2.6$ GeV
- electron isolation: $OpAng(e^\pm$, extra tracks$) > 100\ mrad$
- electron acceptance: $15^\circ \leq \theta_{e^\pm}^{lab} \leq 60^\circ$

4.3.2 Final selection

The preselection produces a data sample containing events with high invariant mass e^+e^- pairs. The next step is the classification of the candidate event into the

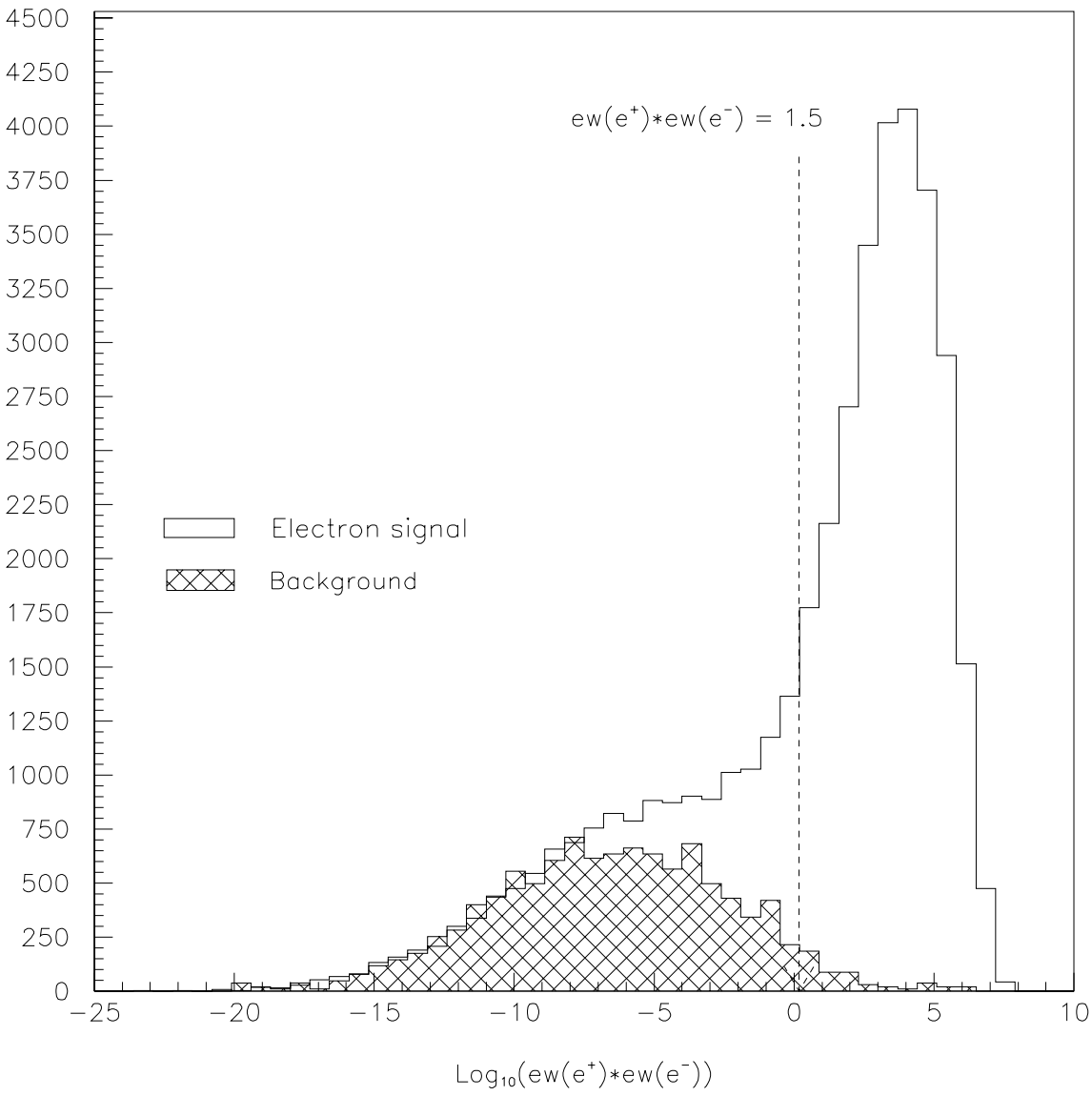

Figure 4.1: Logarithm of the product of the electron weights for the candidate e^+e^- pair. The shaded histogram is off resonance peak background; the areas to the right of the dashed line represent the number of events that pass the *ew* cut.

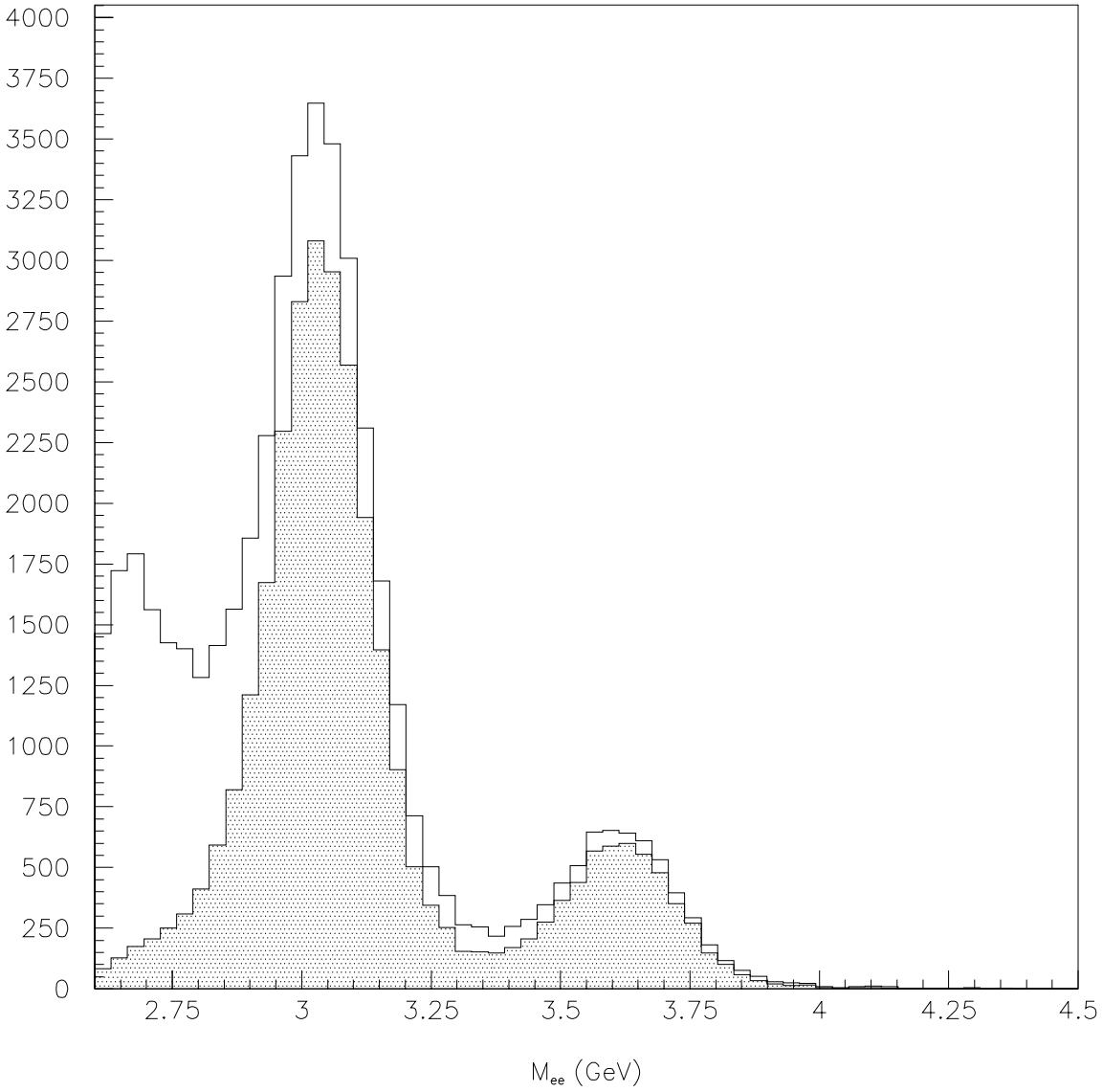

Figure 4.2: Background reduction on mDST sample after electron weight cut $ew_1 * ew_2 > 1.5$ (shaded histogram).

appropriate channel. In this analysis, events are classified by means of kinematical fits, with the addition of topological cuts for $\psi' \to J/\psi\pi^0\pi^0(\eta)$.

Kinematical fits

A way to test whether the observables of a specific event are compatible with the kinematics of a decay channel is to use a kinematical fit. Let us assume we measure a set of n variables $\vec{x}(x_1, x_2, \ldots, x_n)$ with expectation values $\vec{x_0}(x_{01}, x_{02}, \ldots, x_{0n})$. The measured variables may be correlated. Define:

$$\chi^2 = \sum_{j=0}^{n}\sum_{i=0}^{n}(x_{0i} - x_i)\mathcal{V}^{-1}(x_{0j} - x_j) \tag{4.6}$$

where $\mathcal{V}$ is the covariance matrix. Let us also define a set of l constraint equations:

$$f^k(\vec{x}, \vec{y}) = 0, \quad k = 1, l \tag{4.7}$$

where $\vec{y}(y_1, y_2, \ldots, y_s)$ is a vector with unmeasured variables. We want to find the value of $\vec{x_0}$ which minimizes 4.6; to accomplish this we use the method of Lagrange multipliers. We let the multipliers be $\vec{\xi}(\xi_1, \xi_2, \ldots, \xi_l)$, and rewrite 4.6 as:

$$\chi^2 = \sum_{j=0}^{n}\sum_{i=0}^{n}(x_{0i} - x_i)\mathcal{V}^{-1}(x_{0j} - x_j) + 2\sum_{k=1}^{l}\xi_k f^k(\vec{x}, \vec{y}) \tag{4.8}$$

In matrix notation we have:

$$\chi^2 = (x_0 - x)^T\mathcal{V}^{-1}(x_0 - x) + 2\xi^T f \tag{4.9}$$

For a minimum at $x_0 = x_m$ we set:

$$\frac{\partial\chi^2}{\partial x} = 2((x_m - x)^T\mathcal{V}^{-1} + \xi^T\frac{\partial f}{\partial x}) = 0 \tag{4.10}$$

$$\frac{\partial\chi^2}{\partial y} = 2\xi^T\frac{\partial f}{\partial y} = 0 \tag{4.11}$$

$$\frac{\partial\chi^2}{\partial \xi} = 2f = 0 \tag{4.12}$$

In general the equations above are non linear and difficult to solve analytically, therefore an iterative method is usually adopted to find the minumum. Start by considering only a number of constraints equal to the number of s unmeasured variables; this allows us to get starting values. The estimates for x^{min}, y^{min} and ξ^{min} for the $\kappa^{th}+1$ step of the iteration are obtained from step κ^{th}, by Taylor expanding the constraint equations around the minimum point and keeping only the linear terms:

$$f^{\kappa} + \frac{\partial f^{\kappa}}{\partial x}(x_m^{\kappa+1} - x_m^{\kappa}) + \frac{\partial f^{\kappa}}{\partial y}(y_m^{\kappa+1} - y_m^{\kappa}) = 0 \tag{4.13}$$

Using 4.10, 4.11, 4.12 and 4.13 after some algebra one obtains:

$$y_m^{\kappa+1} = y_m^{\kappa} - (\frac{\partial f^{\kappa T}}{\partial y}\mathcal{A}^{-1}\frac{\partial f^{\kappa}}{\partial y})^{-1}\frac{\partial f^{\kappa T}}{\partial y}\mathcal{A}^{-1}(f^{\kappa} + \frac{\partial f^{\kappa}}{\partial x}(x - x_m^{\kappa})) \tag{4.14}$$

where the $l \times l$ matrix $\mathcal{A}$ has been defined as:

$$\mathcal{A} \equiv \frac{\partial f^{\kappa}}{\partial x}\mathcal{V}\frac{\partial f^{\kappa T}}{\partial x} \tag{4.15}$$

Using 4.14 we obtain $\xi_m^{\kappa+1}$ and $x_m^{\kappa+1}$. To evaluate χ^2 at step $\kappa+1$ we use 4.10, set $x_0 = x_m^{\kappa+1}$, and after some algebra we find:

$$\chi^2(\kappa+1) = (\xi_m^{\kappa+1})^T(f^{\kappa} + \frac{\partial f^{\kappa}}{\partial x}(x - x_m^{\kappa}) + \frac{\partial f^{\kappa}}{\partial y}(y_m^{\kappa+1} - y_m^{\kappa})) \tag{4.16}$$

The iteration is continued until the values of $\chi^2(\kappa)$ and $\chi^2(\kappa+1)$ are judged to be close enough for convergence[1]. In our experiment and in the most general case, the measured quantities are the energies and the angles of the tracks in the final state, (E, θ, ϕ). We also assume that the covariance matrix $\mathcal{V}$ be diagonal (measurements not correlated). The constraint equations require the conservation of momentum and energy and impose a restriction on the mass M_v of intermediate particles such as

[1]In this analysis the requirement is that $\frac{|\chi^2(\kappa+1)-\chi^2(\kappa)|}{\chi^2(\kappa)} < 10^{-3}$.

J/ψ, π^0 and η:

$$\sum_{i=1}^{ntrk} p_{xi} = 0 \quad (4.17)$$

$$\sum_{i=1}^{ntrk} p_{yi} = 0 \quad (4.18)$$

$$\sum_{i=1}^{ntrk} p_{zi} = P_{lab} \quad (4.19)$$

$$\sum_{i=1}^{ntrk} E_i = E_{lab} + m_p \quad (4.20)$$

$$(E_i + E_j)^2 - (\vec{p}_i + \vec{p}_j)^2 = M_v^2 \quad (4.21)$$

Integrating the χ^2 distribution gives us the probability $Prob(\chi^2 > \chi^2_m)$ to get a χ^2 higher than the one we measure. The decision to assign an event to a specific channel is made by cutting on such probability. All kinematical fits use CCAL for $e^{\pm}$ and γ energy measurement and for γ direction measurement. The tracking detectors are used for position measurement of the charged particles.

Classification criteria: $\psi' \to e^+e^-$**,** $\psi' \to J/\psi X$

For both these channels only a cut on the kinematical fit probability is used to select the event. The fit to $J/\psi X$ is weakly constrained, therefore an additional requirement on $Prob(e^+e^-)$ is added.

- $Prob(e^+e^-) > 10^{-4}$ (4C)[2], for $\psi' \to e^+e^-$
- $Prob(J/\psi X) > 0.01$ (1C) and $Prob(e^+e^-) < 10^{-4}$, for $\psi' \to J/\psi X$

Classification criteria: $\psi' \to J/\psi\pi^+\pi^-$

The identification of $\psi' \to J/\psi\pi^+\pi^-$ is complicated by two detector specific issues:

[2]The numbers in parenthesis indicate the number of kinematical fit constraints.

- the E835 detector does not measure the energy of hadrons. In most cases charged pions produce a signal in a single CCAL block, depending on their energy. Low energy charged pions occasionally generate no CCAL signal;

- the CCAL is the only detector that can measure both θ and ϕ of a track; if a $\pi^{\pm}$ does not generate a signal in at least one CCAL block we cannot associate the θ and ϕ of the pion

We do not know how to measure the probability that a low energy $\pi^{\pm}$ generate no signal in the CCAL; therefore we need to avoid using the CCAL to associate θ and ϕ lines from $\pi^{\pm}$, when identifying $\psi' \to J/\psi\pi^+\pi^-$ events. The θ and ϕ tracks from the e^+e^- and the $\pi^{\pm}$ are measured by the scintillating fiber detector and by the straw chambers, respectively. In the case of the e^+e^- from the J/ψ the tracks can be identified by using the large energy deposits in the CCAL. It is then possible to perform a cycle of kinematical fits where all possible θ and ϕ lines unassociated with the e^+e^- pair are tested in the $\psi' \to J/\psi\pi^+\pi^-$ hypothesis; the combination with the highest $Prob(\chi^2)$ is chosen. Multiple scattering and vertex uncertainty affect the charged pion path in the inner detectors, as in this decay the pion momentum is low. To account for the multiple scattering contribution to the error in θ in the kinematical fit, we simulated $\psi' \to J/\psi\pi^+\pi^-$ events with a GEANT Monte Carlo [3] and estimated the error in θ as the σ of the difference between the generated and reconstructed $\pi^{\pm}$ tracks, obtaining:

$$\begin{aligned} \sigma_\theta(e^{\pm}) &= 0.026 + 10.7\theta - 30.6\theta^2 + 28.9\theta^3 \; mrad \\ \sigma_\theta(\pi^{\pm}) &= -0.73 + 51.4\theta - 109.1\theta^2 + 78.4\theta^3 \; mrad \end{aligned}$$

The cuts used for the $\psi' \to J/\psi\pi^+\pi^-$ selection are summarized as follows:

[3] Appendix B contains some information about this Monte Carlo.

- $Prob(J/\psi X) > 0.01$ and $Prob(e^+e^-) < 10^{-4}$
- $Prob(J/\psi\pi^+\pi^-) > 10^{-6}$ (3C)
- the e^+e^- pair from the J/ψ must have associated charged tracks in theta and phi.

Classification criteria: $\psi' \to J/\psi\pi^0\pi^0(\eta)$

The selection criteria for $\psi' \to J/\psi\pi^0\pi^0$ and $\psi' \to J/\psi\eta$ are similar. The events have to pass the $J/\psi X$ selection; then a cut on the number of ontime clusters is applied to reduce background from pileup events. The kinematical fit probability cut value is different between the two channels because of the extra background the $J/\psi\eta$ channel receives from the $J/\psi\pi^0\pi^0$ events that lose two photons. Besides the total 4-momentum conservation and e^+e^- invariant mass, the fit constraints include the invariant mass of the photon pairs from the $\pi^0\pi^0$ and the η. The error assigned to the γ energy measurement in the kinematical fits is a fixed fraction of the photon energy for low E_γ; the error is defined as follows: for $E_\gamma < 350$ MeV and $E_\gamma \geq 150$ MeV, $\sigma(E_\gamma) = 0.2E_\gamma$; for $E_\gamma < 150$ MeV, $\sigma(E_\gamma) = 0.3E_\gamma$. To reduce the background from $J/\psi\pi^+\pi^-$ and to avoid losing events with extra charged tracks due to π^0 Dalitz decays and photon conversions, extra ontime hodoscope signals are allowed except when not associated with a Čerenkov-counter signal. The mass plots of each of the two π^0 and of the η after selection are shown in fig. 4.3. The following is a summary of the selection criteria:

- $Prob(J/\psi X) > 0.01$ and $Prob(e^+e^-) < 10^{-4}$
- exactly 6(4) on time clusters in CCAL, for $\pi^0\pi^0(\eta)$ respectively
- $Prob(J/\psi\pi^0\pi^0) > 10^{-6}$ (7C), $Prob(J/\psi\eta) > 10^{-2}$ (6C)

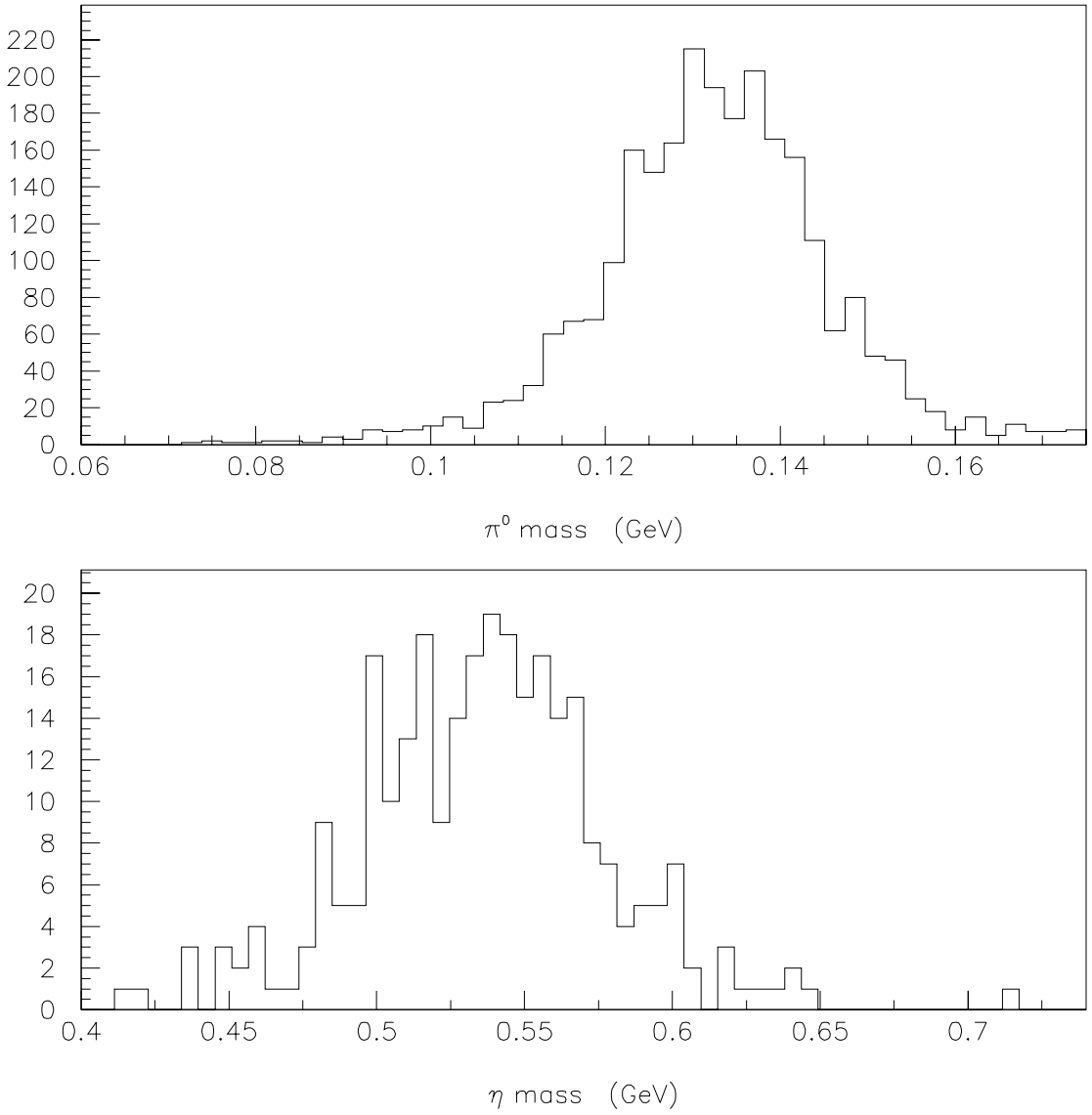

Figure 4.3: Mass of the neutral pions in $\psi' \to J/\psi\pi^0\pi^0$ (above) and of the η in $\psi' \to J/\psi\eta$ (below), after final selection.

- allow on time hodoscope signals not associated with e^+e^-; reject such signals only if not associated with Čerenkov signals.

4.3.3 Background estimation

Background sources include non-resonant continuum events (to which we refer as *external* background) and misidentified events in the $\psi' \to J/\psi X$ channels (*internal* background). External background is estimated by applying the selection criteria used to isolate the signal sample to data taken off the resonance region, normalized to the integrated luminosity collected at the ψ' peak for the signal sample. We used data from the $^1P_1$ energy region and the vicinity of the ψ' peak, for a total integrated luminosity of $\mathcal{L}_{int} = 50.5\ pb^{-1}$ and $\mathcal{L}_{int} = 1.9\ pb^{-1}$ respectively. The shape of the non-resonant background in these two energy regions is similar, as can be seen in fig. 4.4. After the preliminary selection, the background level is greatly reduced, as shown in fig. 4.5 where the background distribution is shown in comparison to the mDST and after preselection samples (after scaling to the signal sample integrated luminosity).

Internal background is estimated by GEANT Monte Carlo. For each channel we generate a sample of 10^5 events; we apply the full selection criteria for each channel to the MC events to obtain the misidentification probability. Table 4.3 reports the results, expressed as the fraction of simulated events classified in each channel normalized to the number of events passing the trigger and preliminary selection.

4.3.4 Background subtraction and selection stability

The number of signal events and the amount of internal and external background is reported in table 4.4. To check the stability of the selection over the course of the data

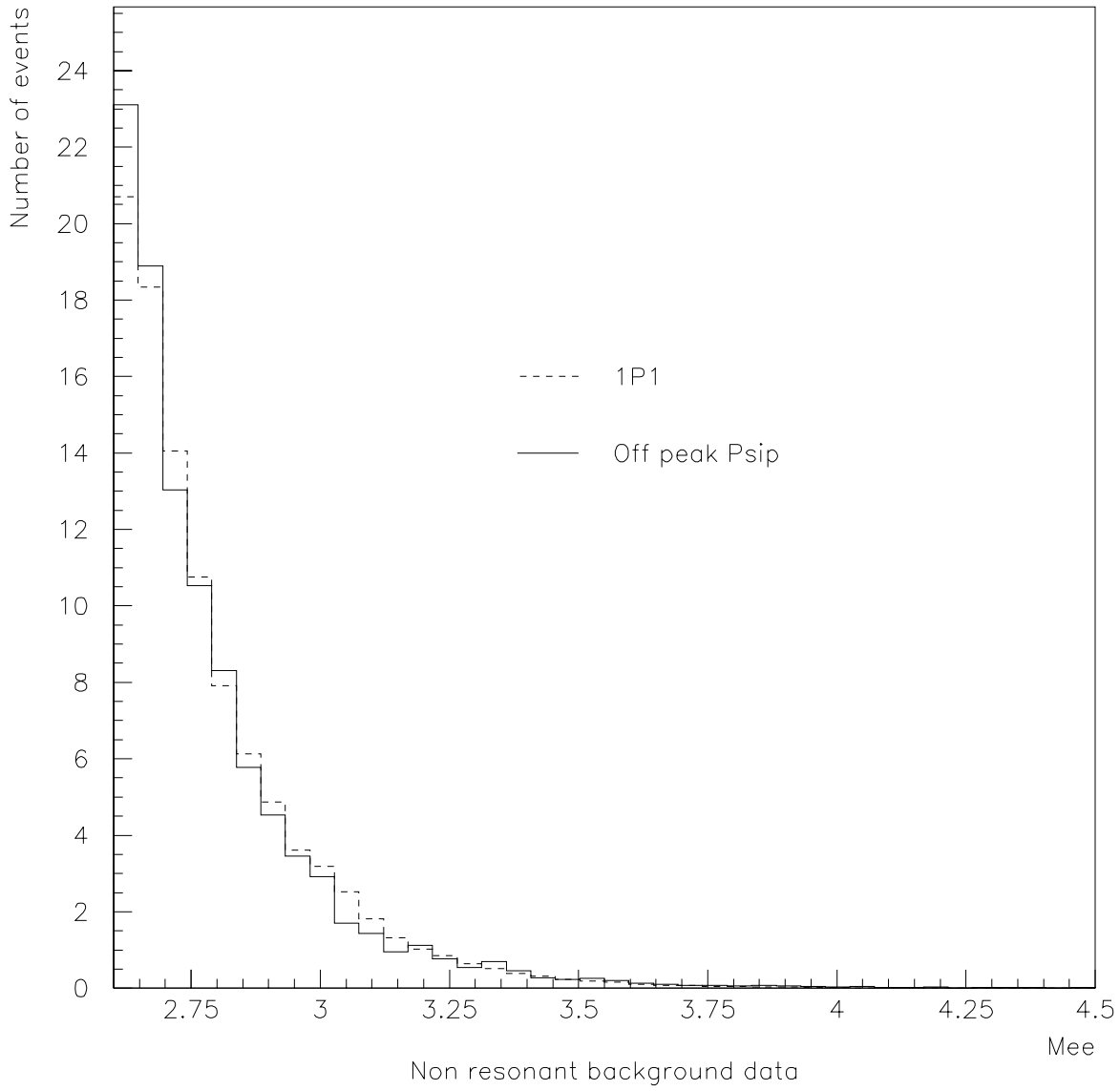

Figure 4.4: Non resonant background m_{ee} distribution comparison between the $^1P_1$ energy range (3523-3529 MeV) and around the ψ' peak.

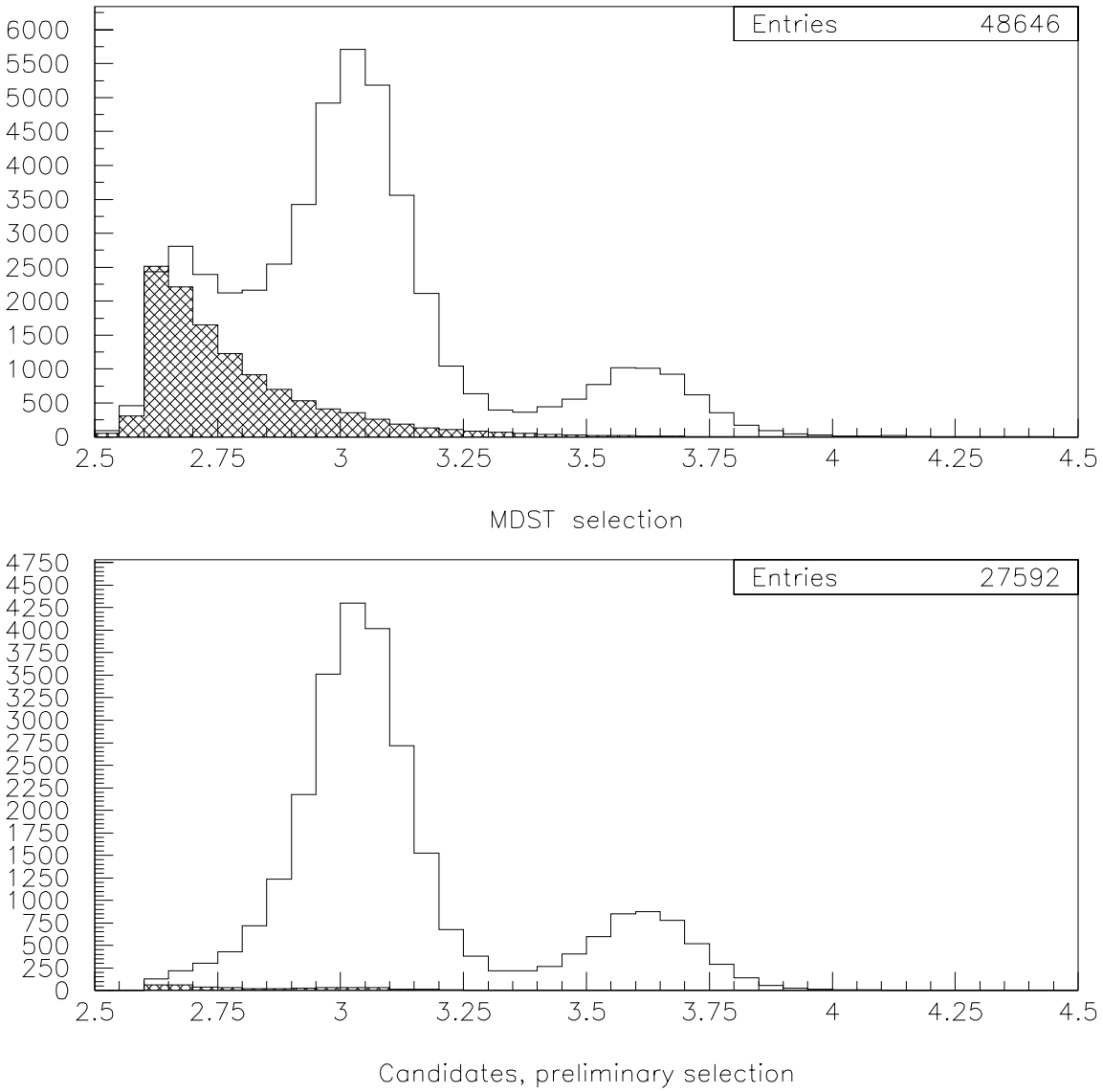

Figure 4.5: e^+e^- invariant mass distribution from mDST and preselection samples. The mass scale is in GeV. The shaded histograms are the external background sample, normalized to the signal sample integrated luminosity. The application of the preselection cuts significantly reduces the non resonant background.

Identified as:	Generated as:			
	e^+e^-	$J/\psi\pi^+\pi^-$	$J/\psi\pi^0\pi^0$	$J/\psi\eta$
e^+e^-	0.9328±0.0007	0.0019±0.0001	0.0020±0.0001	0.00116±0.0001
$J/\psi X$	0.0193±0.0004	0.9629±0.0005	0.9582±0.0006	0.9593±0.0005
$J/\psi\pi^+\pi^-$	$< 10^{-5}$	0.2375±0.0012	0.0029±0.0002	0.0016±0.0001
$J/\psi\pi^0\pi^0$	$< 10^{-5}$	0.0003±0.0001	0.1965±0.0011	0.0034±0.0002
$J/\psi\eta$	$< 10^{-5}$	$< 10^{-5}$	0.0010±0.0001	0.4104±0.0012

Table 4.3: Fraction of simulated events classified in each channel, normalized to the number of events passing the trigger and preliminary selection.

taking period we calculated the ratio of the number of events in each channel to the number of candidates, after preliminary cuts for each stack. The results are reported in table 4.5; the ratios are stable, and most of them fall within their respective statistical errors. One case is noticeably different: the $J/\psi\pi^+\pi^-$ selection for stack 50 shows a N_{ch}/N_{cand} ratio which is 35% lower than the average of the other stacks. The data from stack 50 is kept, since we could not find any indications of data taking condition changes, or detector hardware problems that could justify such deviation.

4.4 Branching ratio measurement: efficiencies and acceptances

The method described in section 4.2 requires an accurate measurement of the ratio of efficiencies in equation 4.5. The efficiencies contributing to this ratio are the acceptance α, the trigger efficiency ϵ_{trig}, the preselection efficiency ϵ_{pres} and the final selection efficiency ϵ_{sel}; with the notation introduced in 4.5:

$$\frac{\varepsilon_{J/\psi X}}{\varepsilon_A} = \left(\frac{\alpha_{J/\psi X}}{\alpha_A}\right)\left(\frac{\varepsilon_{J/\psi X}}{\varepsilon_A}\right)_{trig}\left(\frac{\varepsilon_{J/\psi X}}{\varepsilon_A}\right)_{pres}\left(\frac{\varepsilon_{J/\psi X}}{\varepsilon_A}\right)_{sel} \tag{4.22}$$

Stack	e^+e^-	$J/\psi\pi^+\pi^-$	$J/\psi\pi^0\pi^0$	$J/\psi\eta$	$J/\psi X$	$Preselected$
1	140	77	23	10	531	710
2	592	359	149	39	2545	3342
14	381	234	99	17	1669	2184
29	309	229	86	10	1544	2016
30	148	96	42	7	708	926
49	899	587	245	51	4454	5736
50	543	230	136	32	2507	3302
51	400	296	102	20	2062	2634
54	1088	729	265	65	5131	6742
All	4500±67	2837±53	1147±34	251±16	21151±140	27592±170
Ext. bkg	16	11	2	<1	197	360
Int. bkg	37	24	11	18	64	-
All-bkg	4447±67	2802±53	1134±34	233±16	20890±140	27232±170

Table 4.4: Number of signal and background events, with statistical errors. For each stack the number of raw selected events is reported, for each channel. The background subtracted number of signal events is at the bottom.

The error contributed to the total detection efficiency by the acceptance is due to the uncertainty in the angular distribution parameter $\lambda(\psi')$. The preliminary selection efficiency is subject to two sources of systematic error: accidental low-energy clusters in CCAL and noisy detector channels. These effects depend on the instantaneous luminosity, and they are accounted for by using data collected with a special random trigger called *random gate* (RG). Once an MC event is converted to ADC and TDC counts, the information from one RG event is superimposed to the MC event; the accidental hits in CCAL present in real data taking are simulated in this manner. The systematic error in the final selection efficiency is due to the mismatch between the kinematical fit probability distribution for data and GEANT events.

Stack	e^+e^-	$J/\psi X$	$J/\psi\pi^+\pi^-$	$J/\psi\pi^0\pi^0$	$J/\psi\eta$
1	0.197±0.015	0.748±0.016	0.108±0.012	0.032±0.007	0.014±0.004
2	0.177±0.007	0.762±0.007	0.107±0.005	0.045±0.004	0.012±0.002
14	0.174±0.008	0.764±0.009	0.107±0.007	0.045±0.004	0.008±0.002
29	0.153±0.008	0.766±0.009	0.114±0.007	0.043±0.005	0.005±0.002
30	0.160±0.012	0.765±0.014	0.104±0.010	0.045±0.007	0.008±0.003
49	0.157±0.005	0.776±0.006	0.102±0.004	0.043±0.003	0.009±0.001
50	0.164±0.006	0.759±0.007	0.070±0.004	0.041±0.003	0.010±0.002
51	0.152±0.007	0.783±0.008	0.112±0.006	0.039±0.004	0.008±0.002
54	0.161±0.004	0.761±0.005	0.108±0.004	0.039±0.002	0.010±0.001

Table 4.5: Ratio N_{ch}/N_{cand} in stack by stack order. The errors are statistical.

4.4.1 Acceptances

Electron/positron tracks are considered within the acceptance if:

$$15^\circ < \theta_e < 60^\circ. \tag{4.23}$$

Charged pions are considered within the acceptance if:

$$15^\circ < \theta_e < 55^\circ. \tag{4.24}$$

These polar regions are defined by the efficiency zone of the Čerenkov counter and the hodoscopes for e^+e^-, plus scintillating fibers for the $\pi^+\pi^-$.
The neutral track acceptance is:

$$11.2^\circ < \gamma < 67.4^\circ, \tag{4.25}$$

which corresponds to the CCAL physical boundaries (including the 2 outer rings).

MC simulation

A simulation, to which we will refer here as fMC, is used to determine the acceptances and their dependence on the angular decay distribution parameter $\lambda(\psi')$.

The fMC includes the geometry of the detector and a CCAL shower profile extracted from experimental data [44]. The fMC was designed primarily to estimate the probability for $\pi^0\pi^0$ and $\pi^0\gamma$ events to be detected as *twog* events; it does not perform particle transport, unlike simulations based on GEANT or EGS [52]. Given the shorter event processing times we use the fMC instead of GEANT to estimate the acceptance of ψ' decay channels.

As we have seen in chapter 2, the angular distribution of the electrons for the decay $\psi' \to e^+e^-$ is:

$$w(\lambda, \theta_e^*) = 1 + \lambda cos^2(\theta_e^*) \tag{4.26}$$

$\lambda(\psi')$ is a parameter between -1 and 1, and θ_e^* is the angle between the electron and the momentum of the incoming antiproton in the ψ' rest frame.

The decay $\psi' \to J/\psi\pi\pi$ is generated according to the following approximations:

- the orbital angular momentum between the dipion system and the J/ψ is equal to zero;
- the dipion and the J/ψ are uniformly distributed in the ψ' rest frame;
- the pions are uniformly distributed in $cos\theta_\pi$, where θ_π is the direction of the pion and the J/ψ direction in the dipion rest frame;
- the J/ψ carries away the ψ' polarization. The angular distribution for $J/\psi \to e^+e^-$ in $\psi' \to J/\psi X$ decays is $1 + \lambda(\psi')cos^2(\theta_e)$, where θ_e is the angle between the electron and the $\overline{p}$ direction, in the J/ψ reference frame.

The decay $\psi' \to J/\psi\eta$ is a small (5%) fraction of the inclusive J/ψ decays; it can be shown that the angular distribution for the electrons in the center of mass frame

is [84]:

$$w(\lambda, \theta_e) = 5\lambda(\psi') + 4 - 4\lambda(\psi')cos^2(\theta_e) \tag{4.27}$$

and that the J/ψ is emitted in the ψ' rest frame with distribution:

$$w(\lambda, \theta^*) = 1 + \lambda(\psi')cos^2(\theta^*) \tag{4.28}$$

where θ^* is the angle with respect to the antiproton direction. In this simulation we take $\lambda(J/\psi) = \lambda(\psi') = 0.69$. The MC event generator does not take into account the Wigner rotation implicit in the two Lorentz transformations from the J/ψ rest frame to the ψ' to the laboratory system. This approximation introduces an error $< 0.3\%$ on the $J/\psi \to e^+e^-$ acceptance; the systematic error due to the uncertainty in the angular distribution parameter is an order of magnitude larger, therefore the effect of the Wigner rotation has been neglected.

$J/\psi X$ inclusive and exclusive channels acceptance

A large number (3000000) of events is generated with the MC for each of the exclusive decays of interest, with the appropriate angular distribution. The ratio of the number of events completely within acceptance divided by the total number of events generated gives the efficiency α.

The J/ψ inclusive channel is a mixture of several different decay channels; we consider only the following, which make up 95% of the total $J/\psi X$ events:

- $B(\psi' \to J/\psi\pi^+\pi^-) \simeq 0.305 \sim 0.55\ B(\psi' \to J/\psi X)$
- $B(\psi' \to J/\psi\pi^0\pi^0) \simeq 0.182 \sim 0.33\ B(\psi' \to J/\psi X)$
- $B(\psi' \to J/\psi\eta) \simeq 0.031 \sim 0.056\ B(\psi' \to J/\psi X)$

Acceptances ($\alpha \pm \sigma^{stat}$)				
Channel:	λ=0.45	λ=0.69	λ=0.93	σ_λ^{syst} / α
e^+e^-	0.5746±0.0003	0.5530±0.0003	0.5341±0.0003	0.039
$J/\psi\pi^+\pi^-$	0.2656±0.0003	0.2542±0.0003	0.2453±0.0002	0.045
$J/\psi\pi^0\pi^0$	0.1618±0.0002	0.1550±0.0002	0.1501±0.0002	0.044
$J/\psi\eta$	0.3984±0.0003	0.4029±0.0003	0.4106±0.0003	0.018
$J/\psi X$	0.5467±0.0002	0.5219±0.0002	0.5057±0.0002	0.047
Ratios $\alpha_{\psi X}/\alpha_{channel}$				
Channel:	λ=0.45	λ=0.69	λ=0.93	σ_λ^{syst} / R_λ
e^+e^-	0.9514±0.0006	0.9438±0.0006	0.9469±0.0007	0.0079
$J/\psi\pi^+\pi^-$	2.0580±0.0024	2.0534±0.0025	2.0614±0.0019	0.0038
$J/\psi\pi^0\pi^0$	3.3796±0.0044	3.3673±0.0045	3.3688±0.0047	0.0036
$J/\psi\eta$	1.3723±0.0011	1.2861±0.0011	1.2316±0.0010	0.067

Table 4.6: Geometrical acceptance α and ratio $\alpha_{\psi X}/\alpha_{channel}$, for each channel.

Since the majority of the $J/\psi X$ events are $J/\psi\pi^+\pi^-$ and $J/\psi\pi^0\pi^0$ ($J/\psi\eta$ and $\chi\gamma$ in smaller measure), we can estimate the number of $J/\psi X$ events in the acceptance as the weighted average of the two $J/\psi\pi\pi$ channels plus $J/\psi\eta$:

$$N_{J/\psi X} = \frac{\sum_{i=1}^{3} B_i \times N_i^{acc}}{\sum_{i=1}^{3} B_i} \tag{4.29}$$

where N_i^{acc} is the number of events of type i with e^+e^- from J/ψ in acceptance, and:

$$B_i = B(\psi' \to J/\psi\pi^+\pi^-, \pi^0\pi^0, \eta) \tag{4.30}$$

The experimental value of λ is affected by a large error, of the order of 35%. It is necessary to study how the acceptances vary with λ, since this is the largest source of error in the acceptance calculation. However, the error on the acceptance ratio is considerably smaller, as shown in table 4.6; this is due to the fact that all channels, with the exception of $J/\psi\eta$, have the same angular distribution. The systematic error on the acceptances is chosen as the maximum difference between the ones calculated with the central λ value and the ones at the boundaries.

4.4.2 Trigger efficiency

Trigger efficiencies are evaluated by GEANT simulation by reproducing via software the hardware trigger logic. The charged trigger (e^+e^-X) requirement is:

$$TRG(e^+e^-X) = (CMLU1) * (PBG3) + CMLU2 \tag{4.31}$$

where:

$$\begin{aligned} CMLU1 = (2e) * (H2 < 6) + (1e) * (2h) * (H2 = 2) * (COPL) + \\ +(2e_{new}) * (H2 < 6) + (1e_{new}) * (2h_{new}) * (H2 = 2) * (COPL_{new}) \end{aligned} \tag{4.32}$$

$$\begin{aligned} CMLU2 = (2e) * (H2 = 2) * (COPL) * \overline{(FCH)} + \\ +(2e_{new}) * (H2 = 2) * (COPL_{new}) * \overline{(FCH)} \end{aligned} \tag{4.33}$$

Here CMLUx is the output of the memory lookup unit that combines the single detector logics, and PBG3 is the requirement of 2 back-to-back energy deposits in the CCAL. The *new* subscript indicates a logic implemented on a trigger card used as a backup, to improve the reconstruction of charged tracks and to add a new logic for the $\phi\phi$ channel. Refer to par. 3.8.1 and fig. 3.12 for a description of the logic signals.

An RG event is superimposed to each of the 10^5 GEANT simulated events. The efficiency for the $J/\psi X$ channel is the weighted average of the $J/\psi\pi\pi$ and $J/\psi\eta$ channels. The results are presented in table 4.7. The MC estimate for the charged trigger efficiency can be compared to the measurement performed on a data sample: in June 2000, a short running period ($\mathcal{L} = 0.99\ nb^{-1}$) in stack 29 was dedicated to a special trigger run at the ψ' energy with the purpose of measuring the charged trigger efficiency. The special trigger selects events with at least $1e$:

$$TRG = (1e + 1e_{new}) * (PBG3) + CMLU2 + (2e_{new}) * (H2 < 6) * (PBG3) \tag{4.34}$$

Decay mode	ϵ_{tr}(mode)	$\epsilon_{tr}(\ J/\psi X)/\ \epsilon_{tr}$(mode)
e^+e^-	0.9074±0.0006	0.974±0.002
$J/\psi\pi^0\pi^0$	0.903±0.001	0.978±0.002
$J/\psi\pi^+\pi^-$	0.871±0.001	1.015±0.002
$J/\psi\eta$	0.9036±0.0008	0.978±0.002

Table 4.7: Trigger efficiencies and efficiency ratios for each channel; note that the angular acceptances are not included.

The sample, consisting of 216 events, is selected with cuts on GM(e^+e^-)[4], $M_{e^+e^-}$, number of CCAL clusters, number of Čerenkov photoelectrons.

The total CMLU1 efficiency was estimated to be:

$$\epsilon(e^+e^- + \ neutrals) = 0.92 \pm 0.02 \tag{4.35}$$

For events e^+e^-+*charged tracks* the efficiency is lower, since the only contribution to the trigger comes from the 1st branch in 4.32:

$$\epsilon(e^+e^- + \ charged) = 0.86 \pm 0.02 \tag{4.36}$$

The efficiencies estimated with data are in good agreement with the software-evaluated efficiencies.

4.4.3 Preselection efficiency

Electron weight cut efficiency

The preselection efficiency is determined by GEANT simulation for all the applied cuts but the *ew*. The efficency ϵ_{ew} for the *ew* cut must be estimated from the data sample. For the purpose of cut efficiency evaluation some of the distributions used

[4]The *gatemaster* (GM) is a module that does a logic OR of all the triggers of the experiment and generates *gates* to the electronics.

by the ew are not reproduced well enough by the GEANT Monte Carlo; the GEANT transverse shower size is smaller than the actual size, therefore the ew distributions for shower containment and cluster mass show a less-than-perfect agreement between data and simulation, as shown in fig. 4.6. The e^+e^- electron weight distributions (especially hodoscope *mips* and CCAL shower confinement) are perturbed by nearby tracks and CCAL clusters not belonging to e^+e^-. For this reason, each ψ' decay channel has a different ew cut efficiency. In order to estimate the ew cut efficency for the various channels we selected a clean sample of events for each channel without using the ew. This procedure does not present particular problems; it consists of applying final selection cuts stricter than the ones described in section 4.3. In the case of $J/\psi\pi^0\pi^0$ and $J/\psi\eta$ we also check that the extra (non electron/positron) tracks do not pair with the e^+e^- from the J/ψ to yield a π^0 or an η. However, for $\psi' \to J/\psi\pi^+\pi^-$ the background rejection without using the ew is a laborious task; π^0 Dalitz decays and γ conversions from the large number of $\overline{p}p \to \pi^0\pi^0$ events simulate hits in the hodoscopes that cause them to be mistaken for $J/\psi\pi^+\pi^-$ events. The efficiencies of the ew cut are reported on the first row of table 4.8 The cut on $OpAng$ reduces

ϵ_{ew}, no $OpAng$ cut			
e^+e^-	$J/\psi\pi^+\pi^-$	$J/\psi\pi^0\pi^0$	$J/\psi\eta$
0.922±0.006	0.891±0.005	0.91±0.01	0.90±0.02
ϵ_{ew}, $OpAng(e^{\pm}, extra\ track) > 100\ mrad$			
e^+e^-	$J/\psi\pi^+\pi^-$	$J/\psi\pi^0\pi^0$	$J/\psi\eta$
0.932±0.006	0.924±0.005	0.93±0.01	0.92±0.02

Table 4.8: Efficiency of the $ew(e^{\pm}) > 1.5$ cut; the channel dependence is reduced by using the opening angle cut.

the dependence of ϵ_{ew} on the decay channel, so that in the ratio between channels the ew efficiencies cancel.

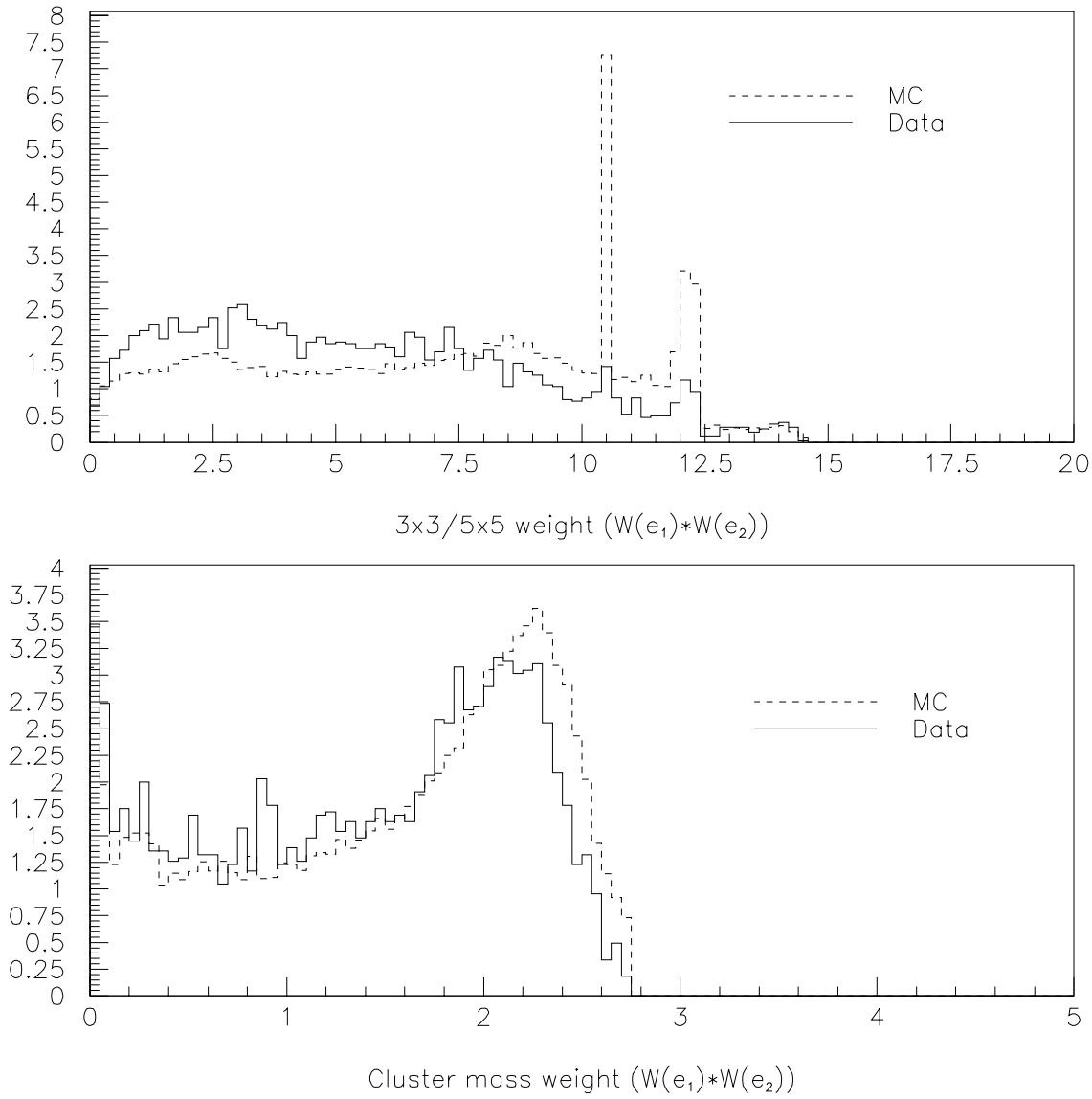

Figure 4.6: Product of shower containment (above) and cluster mass (below) electron weight. The events are from data selected and GEANT simulated $\psi' \to e^+e^-$.

e^+e^- invariant mass and electron isolation cut efficiencies

The preselection cuts are designed to reduce the background to events with e^+e^- coming either from the ψ' or the J/ψ in inclusive $\psi' \to J/\psi X$ decays. The invariant mass $m_{e^+e^-}$ distribution is centered on the ψ' mass for $\psi' \to e^+e^-$ events, and on the J/ψ mass for $\psi' \to J/\psi X$. The lower mass tail for the $J/\psi X$ m_{ee} distribution is higher than for the exclusive e^+e^-, therefore the cut on m_{ee} has influence only on the ratio $\epsilon_{J/\psi X}/\epsilon_{e^+e^-}$ for $m_{ee} > 2.6$ GeV. This efficiency ratio is estimated with the GEANT Monte Carlo and is equal to:

$$\left[\frac{\epsilon_{J/\psi X}}{\epsilon_{e^+e^-}}\right]_{m_{ee}>2.6\ \mathrm{GeV}} = 0.9928 \pm 0.0004$$

Obviously the same efficiency ratio for the inclusive J/ψ channels is equal to 1.

The e^+e^- isolation cut efficiency is estimated with the GEANT Monte Carlo. The results are shown in table 4.9.

Mode	ϵ_{opang}
e^+e^-	0.921±0.001
$J/\psi\pi^+\pi^-$	0.888±0.001
$J/\psi\pi^0\pi^0$	0.878± 0.001
$J/\psi\eta$	0.895± 0.001

Table 4.9: *OpAng* cut efficiency MC estimate for each channel.

4.4.4 Final selection efficiency

The final selection efficiency is estimated by GEANT Monte Carlo, where for each channel we generate 10^5 events. Besides including in the GEANT simulated events the real data from the RG trigger, as mentioned previously in section 4.4, we analyzed the MC events with calibration constants (and RG events) from three different runs

Channel	ϵ_{sel}
$\psi' \to e^+e^-$	0.933±0.038
$\psi' \to J/\psi\pi^+\pi^-$	0.491±0.018
$\psi' \to J/\psi\pi^0\pi^0$	0.583±0.026
$\psi' \to J/\psi\eta$	0.656±0.046
$\psi' \to J/\psi X$	0.961±0.021

Table 4.10: Final selection efficiences.

and averaged the results. To estimate the efficiency ϵ_{sel} we select MC events that pass the software trigger requirement for e^+e^- events, have $m_{ee} > 2.2$ GeV and have all the particles in the final state within acceptance; the fraction of this sample that passes the final selection cuts is ϵ_{sel}. The efficiency $[\epsilon_{sel}]_{J/\psi X}$ for $\psi' \to J/\psi X$ is obtained separately from $J/\psi\pi^+\pi^-$, $J/\psi\pi^+\pi^-$ and $J/\psi\eta$ events; the final number is the BR-weighted average of the three estimates. The results are reported in table 4.10. The systematic error on ϵ_{sel} has been evaluated by changing the fit probability cut value and taking the largest difference in the final result as the error.

4.5 Measurement of $\lambda(\psi')$

The selection used for the $\psi' \to e^+e^-$ angular distribution sample is different from the one applied in the branching ratio analysis. It is important to apply cuts that do not introduce artificial non-uniformities with respect to θ; the ew cut value is lowered to 0.1, and the $J/\psi X$ fit (1C) probability cut is rather loose, compared to the branching ratio analysis. We also cut on the acceptance of the e^+e^-, on the e^+e^- invariant mass and on the error $\sigma(cos(\theta^*))$ propagated from the laboratory error on θ; θ^* is the polar angle in the CM reference frame. An additional requirement is placed on the back-to-back kinematics of the e^+e^-; to this purpose, the following two

quantities are defined for each event:

$$\Delta\phi \equiv \mid \pi - \mid \phi_1 - \phi_2 \mid\mid$$
$$\Delta\theta \equiv \mid \pi - \mid \theta_1^* + \theta_2^* \mid\mid$$

where the indexes 1,2 indicate either the electron or the positron, since our detector cannot distinguish between e^+ and e^-. There is no requirement on the number of clusters. A summary of the cuts applied is the following:

- $m_{ee} > 3.3$ GeV
- $ew_1 * ew_2 > 0.1$
- $Prob(J/\psi X) < 0.001$
- $\sigma(cos(\theta^*_{1,2})) < 0.012$
- $\mid cos(\theta^*_{1,2}) \mid < 0.45$
- $\sqrt{(\Delta\phi)^2 + (\Delta\theta)^2} < 40\ mrad$

The e^+e^- invariant mass distribution after all cuts is shown in fig.4.7. The $\Delta\theta$ and $\Delta\phi$ distributions are shown in fig. 4.8, with all the cuts on the other variables applied.

The event distribution in $cos(\theta^*)$, with all but the acceptance cut applied is shown in fig. 4.9. The fit result depends critically on the number of events at the edges of the $cos(\theta^*)$ distribution, so the cut on $\mid cos(\theta^*) \mid$ has been chosen to select a region with no loss of events due to one of the two particles falling out of the detector acceptance.

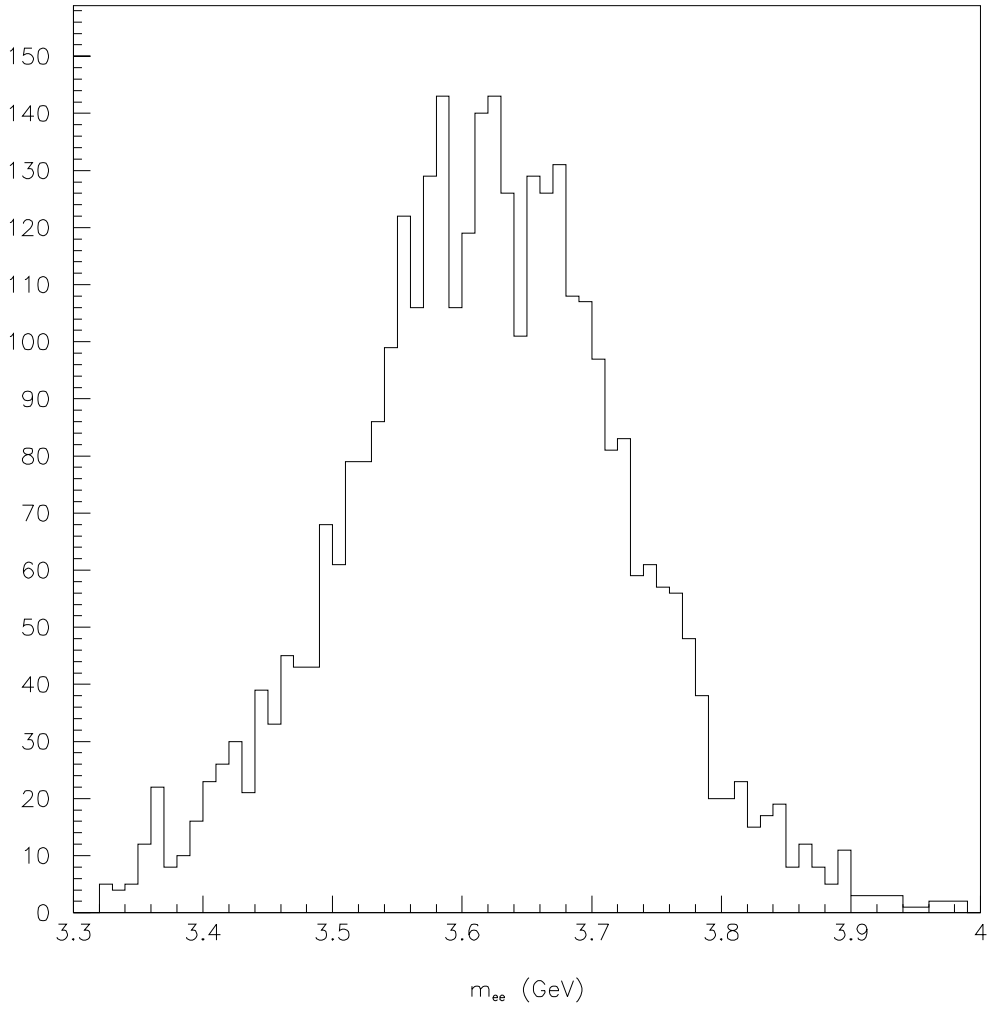

Figure 4.7: e^+e^- invariant mass after the selection cuts for $\lambda(\psi')$ measurement.

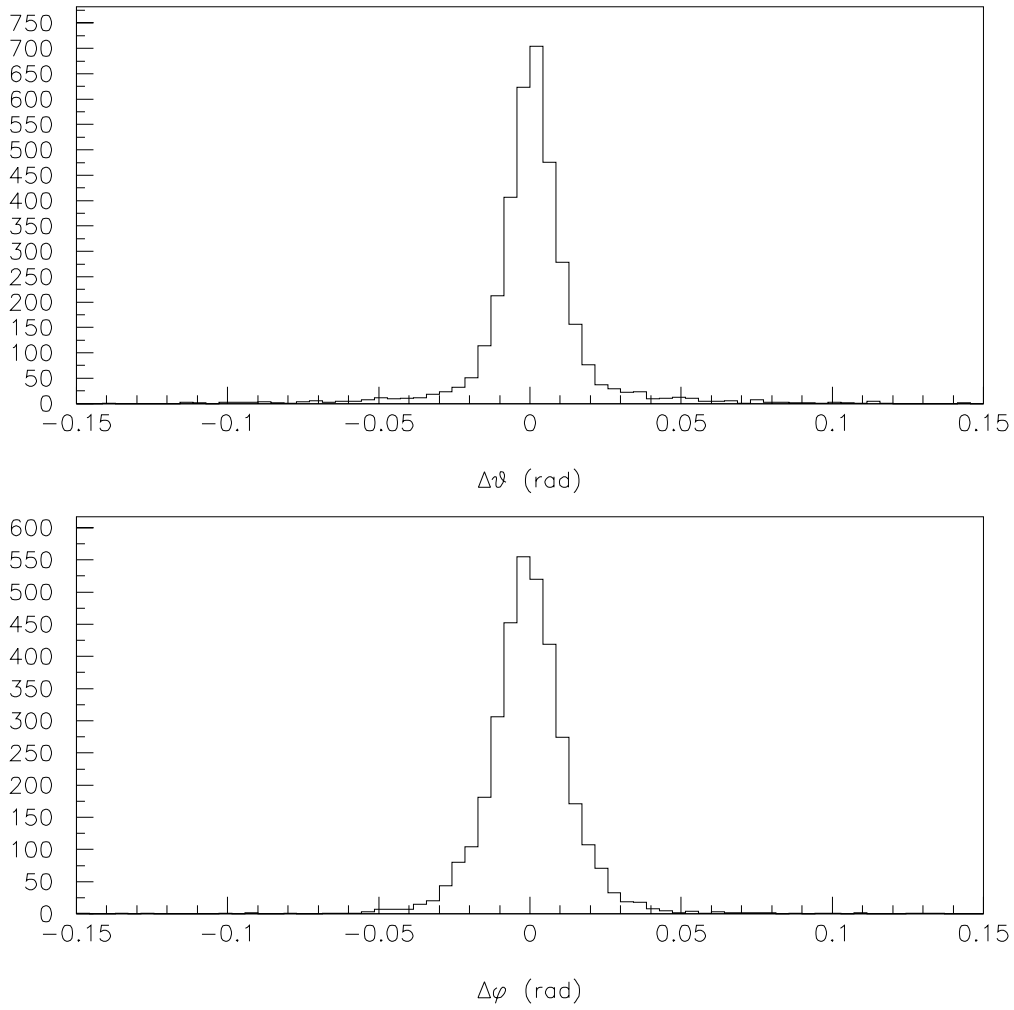

Figure 4.8: Collinearity distributions for the e^+e^- in the CM reference frame, with all other cuts applied.

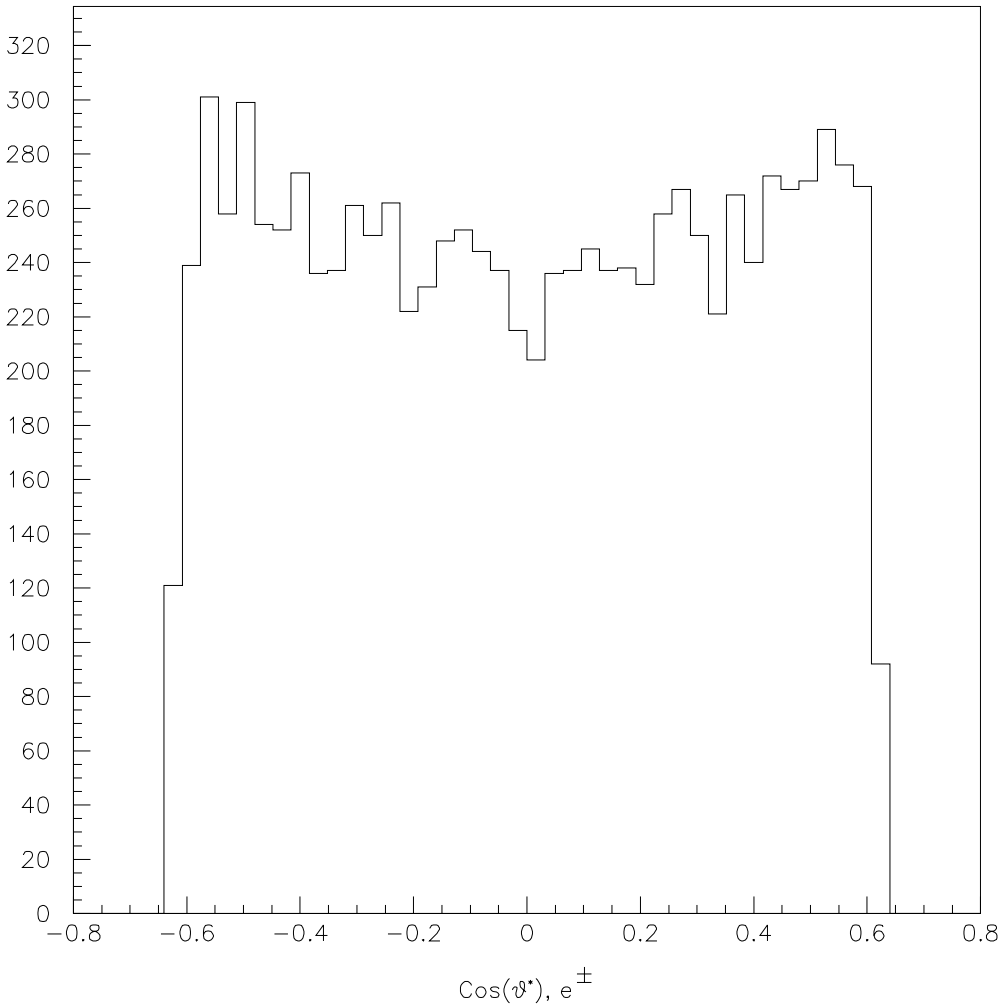

Figure 4.9: Angular distribution before detection efficiency correction and application of $\mid cos(\theta^*_{1,2}) \mid < 0.45$.

The best estimate of the parameter $\lambda(\psi')$ has been obtained by maximizing[5] the likelihood function defined as:

$$ln\ \mathcal{L}(\lambda) = \sum_{i=1}^{M} ln\ \frac{\epsilon(cos\theta_i^*)(1+\lambda\ cos^2\theta_i^*)}{\int_0^1 \epsilon(cos\theta')(1+\lambda\ cos^2\theta')d(cos\theta')} \tag{4.37}$$

where $\epsilon(cos\theta_i^*)$ is the total detection efficiency as a function of the CM polar angle and M is the number of electron/positron tracks (i.e. the number of events is $N = M/2$). The efficiency as a function of the polar angle has been evaluated with GEANT for all the cuts but the ew, for which we used a clean sample of $\psi' \to e^+e^-$ selected without using the ew, as described in section 4.4.3. The detection efficiency shows a negligible dependence on the polar angle and is almost flat at $\sim$78%. This is due to the fact that the inner detectors calibration is designed to take into account the dependence of the signal on the polar angle of the particle. The GEANT simulation has also been used to test the maximum likelihood fit to the data; a fit to simulated events generated with $\lambda = 0.69$ returned the same value. The results of the maximization are shown in table 4.11. The final number of events selected is 3314. The background is evaluated with a data sample of $\mathcal{L}_{int} = 1.9\ pb^{-1}$, taken around the ψ' peak. Only 1 event passes the selection, therefore the background is negligible. No limits on the parameter have been set in the maximization[6]. The errors are estimated by calculating the full second-derivative matrix by finite differences and inverting it.

[5]We chose to perform an *unbinned* fit. We verified that the *binned* fit gives equivalent results.

[6]In some cases it is necessary to prevent the parameters from taking on unphysical values by setting limits in the maximization process; however, bound parameters introduce numerical inaccuracy in addition to what is required to estimate the value of the likelihood function.

Stack	$\lambda(\psi')$	$N_{e^+} + N_{e^-}$
1	0.36±1.2	206
2	0.47±0.61	860
14	0.80±0.81	576
29	0.50±0.83	456
30	0.81±1.3	218
49	0.77±0.54	1288
50	0.71±0.66	798
51	1.07±0.82	586
54	0.78±0.46	1640

Table 4.11: Stack-by-stack maximum likelihood fit to the e^+e^- angular distribution data sample.

Chapter 5

Results

In this chapter we will show the final results for the measurement of the branching ratios $\psi' \to e^+e^-$, $\psi' \to J/\psi\pi^+\pi^-$, $\psi' \to J/\psi\pi^0\pi^0$ and $\psi' \to J/\psi\eta$. We will give the final result for the measurement of the $\psi' \to e^+e^-$ angular distribution parameter $\lambda(\psi')$. We will compare the results obtained to previous measurements.

5.1 ψ' branching ratios

As we have shown in section 4.2, the branching ratios for the four channels we analyzed can be estimated using their ratios to $B(\psi' \to J/\psi X)$ through equation 4.5. We used the following values from the PDG 2002 [27]:

$$B(\psi' \to J/\psi X) = 0.557 \pm 0.026 \tag{5.1}$$

$$B(J/\psi \to e^+e^-) = 0.0593 \pm 0.0010 \tag{5.2}$$

$$B(\eta \to \gamma\gamma) = 0.3943 \pm 0.0026 \tag{5.3}$$

$$B(\pi^0 \to \gamma\gamma) = (98.798 \pm 0.032)\% \tag{5.4}$$

From the analysis in the previous chapter we obtain the efficiency ratios and the number of events ratios, summarized in table 5.1. Our final result for $B(\psi' \to e^+e^-)$

Decay mode	e^+e^-	$J/\psi\pi^0\pi^0$	$J/\psi\pi^+\pi^-$	$J/\psi\eta$
$\epsilon_{tr}(_{J/\psi X})/\epsilon_{tr}(mode)$	0.974±0.002	0.978±0.002	1.015±0.002	0.978±0.002
$\epsilon_{pr}(_{J/\psi X})/\epsilon_{pr}(mode)$	0.953±0.005	1.008±0.004	0.996±0.004	0.987±0.003
$\epsilon_{sel}(_{J/\psi X})/\epsilon_{sel}(mode)$	1.030±0.042	1.648±0.074	1.956±0.072	1.46±0.10
$N(mode)/N(_{J/\psi X})$	0.213±0.003	0.054±0.002	0.134±0.002	0.0112±0.0008

Table 5.1: Trigger, preliminary and final selection efficiencies; the last row shows the ratio of background subtracted number of events. For the acceptance ratios refer to table 4.6.

is:

$$\frac{B(\psi' \to e^+e^-)}{B(\psi' \to J/\psi X)} = (1.14 \pm 0.02 \pm 0.05) \times 10^{-2} \tag{5.5}$$

$$B(\psi' \to e^+e^-) = (6.3 \pm 0.1 \pm 0.4) \times 10^{-3} \tag{5.6}$$

where in 5.6 we use eq. 5.1. This result is an improvement with respect to the measurement published by E835 with data from the 1996-97 run; it improves statistical and systematic errors by a factor of 2. The main contributions to the 6.3% systematic error are from $B(\psi' \to J/\psi X)$ and from the final selection efficiency. For $B(\psi' \to J/\psi\pi^+\pi^-)$ we find:

$$\frac{B(\psi' \to J/\psi\pi^+\pi^-)}{B(\psi' \to J/\psi X)} = (54.5 \pm 1.0 \pm 2.0) \times 10^{-2} \tag{5.7}$$

$$B(\psi' \to J/\psi\pi^+\pi^-) = (30.3 \pm 0.5 \pm 1.8) \times 10^{-2} \tag{5.8}$$

This result is in good agreement with the PDG 2002 fit, and the errors are significantly reduced with respect to E760. The branching ratio for the channel $\psi' \to J/\psi\pi^0\pi^0$ is:

$$\frac{B(\psi' \to J/\psi\pi^0\pi^0)}{B(\psi' \to J/\psi X)} = (30.7 \pm 0.9 \pm 1.4) \times 10^{-2} \tag{5.9}$$

$$B(\psi' \to J/\psi\pi^0\pi^0) = (17.1 \pm 0.5 \pm 1.1) \times 10^{-2} \tag{5.10}$$

which shows only a slight improvement over the 1996-97 run. If isospin is conserved in $J/\psi\pi\pi$ decays, the ratio $B(\psi' \to J/\psi\pi^0\pi^0)/B(\psi' \to J/\psi\pi^+\pi^-)$ is equal to 0.5;

Decay mode	e^+e^-	$J/\psi\pi^0\pi^0$	$J/\psi\pi^+\pi^-$	$J/\psi\eta$
$\delta R(\alpha)$	0.8%	0.1%	0.2%	6.3%
$\delta R(\epsilon_{tr})$	0.2%	0.2%	0.2%	0.2%
$\delta R(\epsilon_{pr})$	0.3%	0.4%	0.4%	0.3%
$\delta R(\epsilon_{sel})$	4.1%	4.5%	3.7%	7.0%
Statistical	1.3%	2.9%	1.8%	6.7%
Total	4.4%	5.4%	4.1%	11%

Table 5.2: Systematic error and statistical error contributions to the total error, in percent, for the ratio $B(\psi' \to f)/B(\psi' \to J/\psi X)$. $\delta R(\epsilon)$ indicates the fractional error from the efficiency ratio $\epsilon(_{J/\psi X})/\epsilon(mode)$.

taking the ratio of our results 5.8 and 5.10 we obtain:

$$\frac{\Gamma(\psi' \to J/\psi\pi^0\pi^0)}{\Gamma(\psi' \to J/\psi\pi^+\pi^-)} = 0.56 \pm 0.05 \tag{5.11}$$

It is evident that 5.11 does not constitute a strong statement either way. It is compatible with isospin conservation, but also with isospin violation at the percent level. Finally, for $B(\psi' \to J/\psi\eta)$ we measured:

$$\frac{B(\psi' \to J/\psi\eta)}{B(\psi' \to J/\psi X)} = (4.9 \pm 0.3 \pm 0.4) \times 10^{-2} \tag{5.12}$$

$$B(\psi' \to J/\psi\eta) = (2.7 \pm 0.2 \pm 0.3) \times 10^{-2} \tag{5.13}$$

Table 5.2 reports the contributions of the sources of error to the total error. Table 5.3 and figures 5.1, 5.2, 5.3 and 5.4 show how our results compare to previous measurements and to the Particle Data Group 2002 fit. The PDG 2002 estimate is a maximum likelihood fit to determine 23 parameters, from a set of 79 measurements. The parameters include ψ', χ_0 and χ_1 branching ratios and total widths. This is done to avoid correlations that arise when an experiment uses previously reported measurements to extract a branching ratio; as it is the case with our results, for example, which depend on $B(\psi' \to J/\psi X)$ measured elsewhere. Further details about the PDG treatment of ψ' and χ_c branching ratios can be found in ref. [27][71][50].

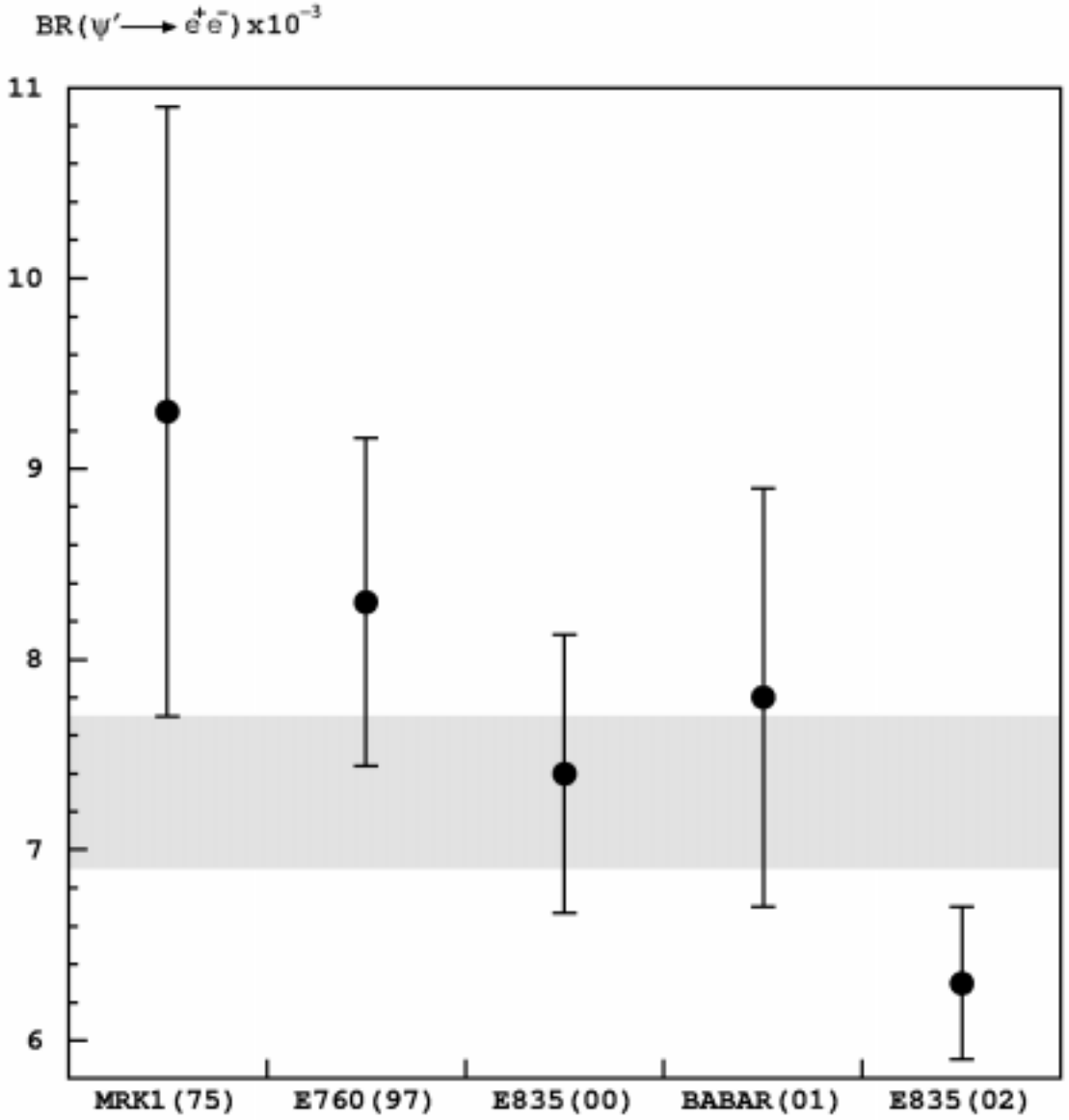

Figure 5.1: E835 measurements of $B(\psi' \to e^+e^-)$ compared to the results of previous experiments. The gray band indicates the 1σ region around the fit value from the PDG2002. References: MRK1(75) [37], E760(97) [35], E835(00) [29], BABAR(01) [18].

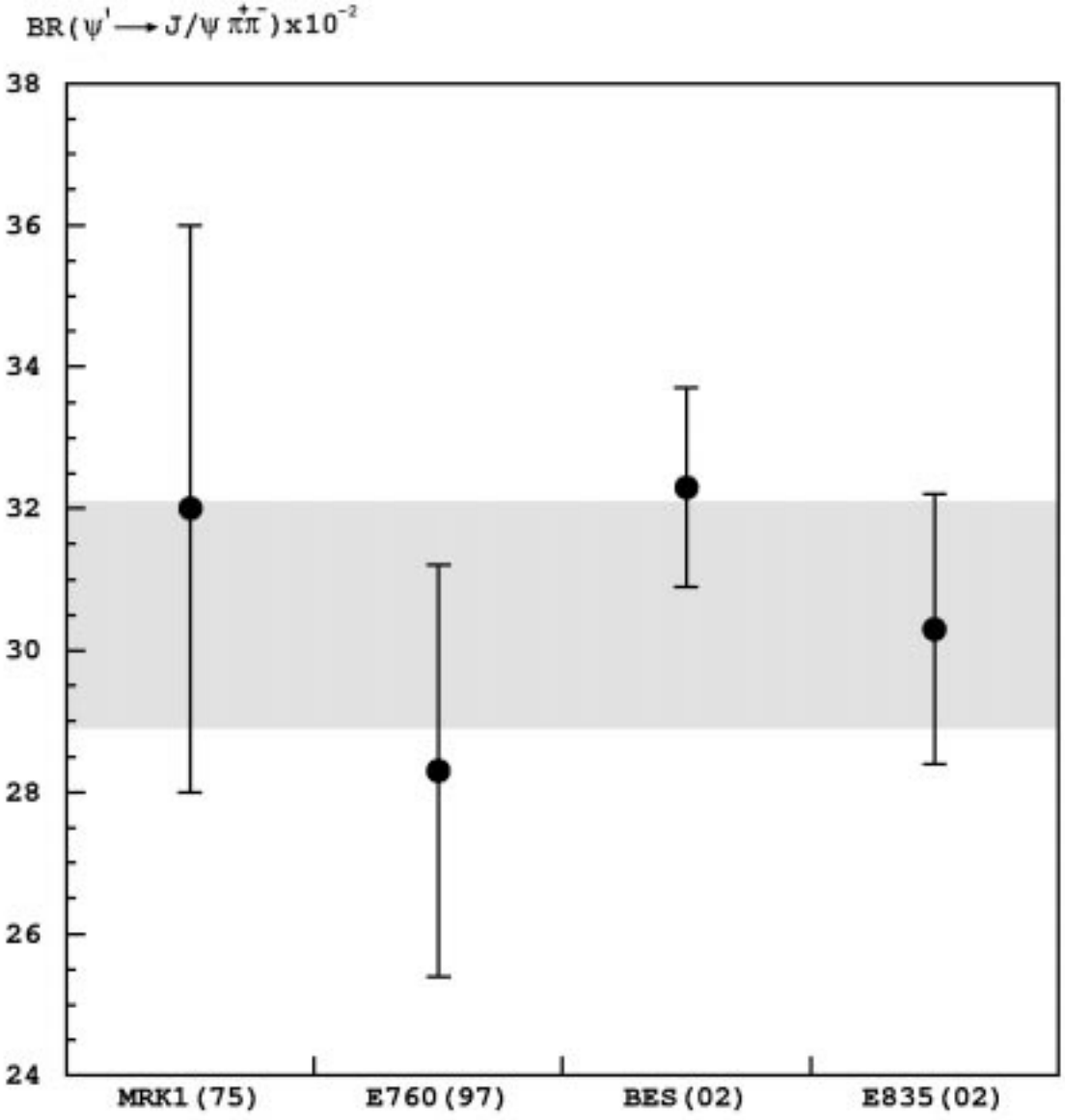

Figure 5.2: E835 measurements of $B(\psi' \to J/\psi\pi^+\pi^-)$ compared to the results of previous experiments. The gray band indicates the 1σ region around the fit value from the PDG2002. References: MRK1(75) [23], E760(97) [35], BES(02) [26].

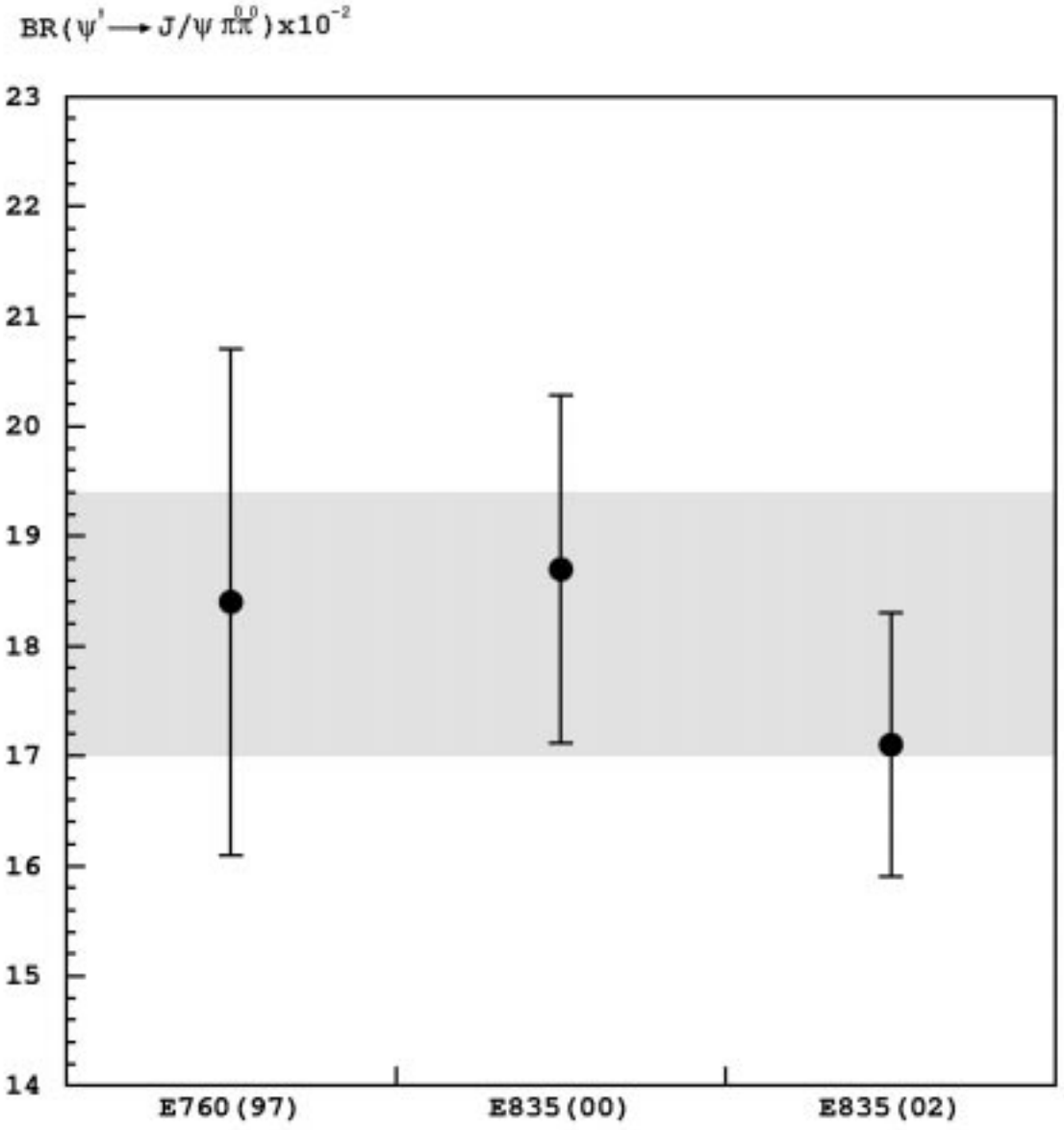

Figure 5.3: E835 measurements of $B(\psi' \to J/\psi\pi^0\pi^0)$ compared to the results of E760 and the previous run of E835. The gray band indicates the 1σ region around the fit value from the PDG2002. References: E760(97) [35], E835(00) [29].

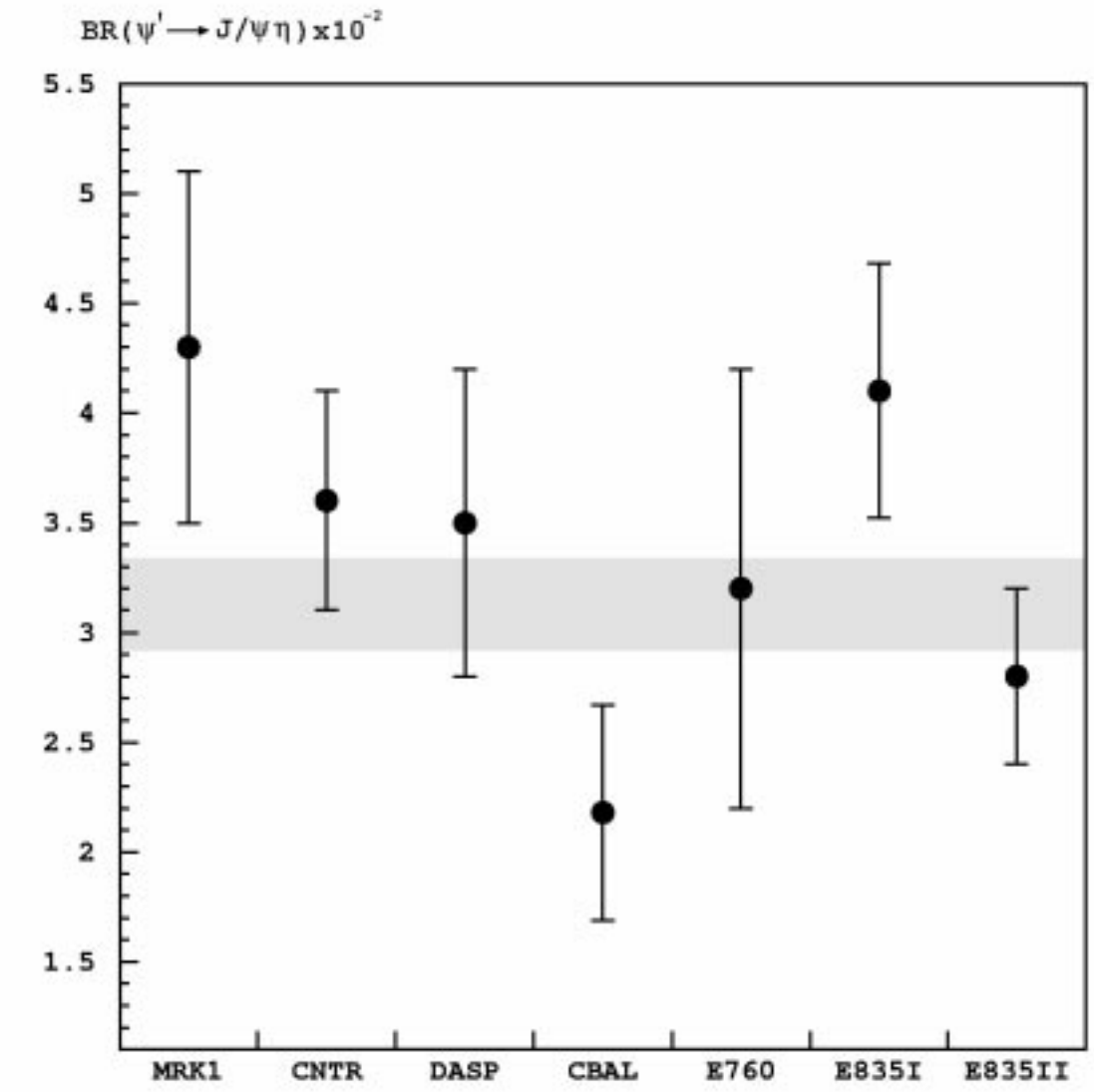

Figure 5.4: E835 measurements of $B(\psi' \to J/\psi\eta)$ compared to the results of previous experiments. The gray band indicates the 1σ region around the fit value from the PDG2002. References: MRK1 [39], CNTR [38], DASP [31], CBAL [30], E760 [35], E835I [29].

Channel	E835 2000
$\mathcal{B}(\psi' \to e^+e^-) \times 10^{-3}$	6.3±0.1±0.4
$\mathcal{B}(\psi' \to J/\psi\pi^+\pi^-) \times 10^{-2}$	30.3±0.5±1.8
$\mathcal{B}(\psi' \to J/\psi\pi^0\pi^0) \times 10^{-2}$	17.1±0.5±1.1
$\mathcal{B}(\psi' \to J/\psi\eta) \times 10^{-2}$	2.7±0.2±0.3

Channel	E835 96-97	E760	PDG 2002
$\mathcal{B}(\psi' \to e^+e^-) \times 10^{-3}$	7.4±0.2±0.7	8.3±0.5 ±0.7	7.3±0.4
$\mathcal{B}(\psi' \to J/\psi\pi^+\pi^-) \times 10^{-2}$	not published	28.3±2.1±2.0	30.5±1.6
$\mathcal{B}(\psi' \to J/\psi\pi^0\pi^0) \times 10^{-2}$	18.7±0.9±1.3	18.4±1.9±1.3	18.2±1.2
$\mathcal{B}(\psi' \to J/\psi\eta) \times 10^{-2}$	4.1±0.3±0.5	3.2±1.0±0.2	3.13±0.21

Table 5.3: Results of this analysis, compared to E835 '97, E760 and PDG02 fit.

5.2 The $\lambda(\psi')$ parameter

Table 4.11 shows the maximum likelihood best fit stack by stack; averaging over all stacks gives:

$$\lambda(\psi') = 0.71 \pm 0.23 \tag{5.14}$$

The best fit function is shown in fig 5.5, superimposed on the $cos(\theta^*)$ distribution. Using the result 5.14 in eq. 2.44, we find:

$$\left|\frac{G_E}{G_M}\right| = 0.81 \pm 0.37 \tag{5.15}$$

The only previous measurement of $\lambda(\psi')$ was made by E760, unlike $\lambda(J/\psi)$, which was measured by several other experiments with the process $e^+e^- \to J/\psi \to \overline{p}p$. There is only a slight improvement on the E760 result $\lambda(\psi') = 0.69 \pm 0.26$. Our mesurement agrees with all the theoretical predictions for $\lambda(\psi')$ presented in section 2.1.5, except for Brodsky and Lepage [4], where $\lambda(\psi') = 1$ is predicted with a perturbative approach.

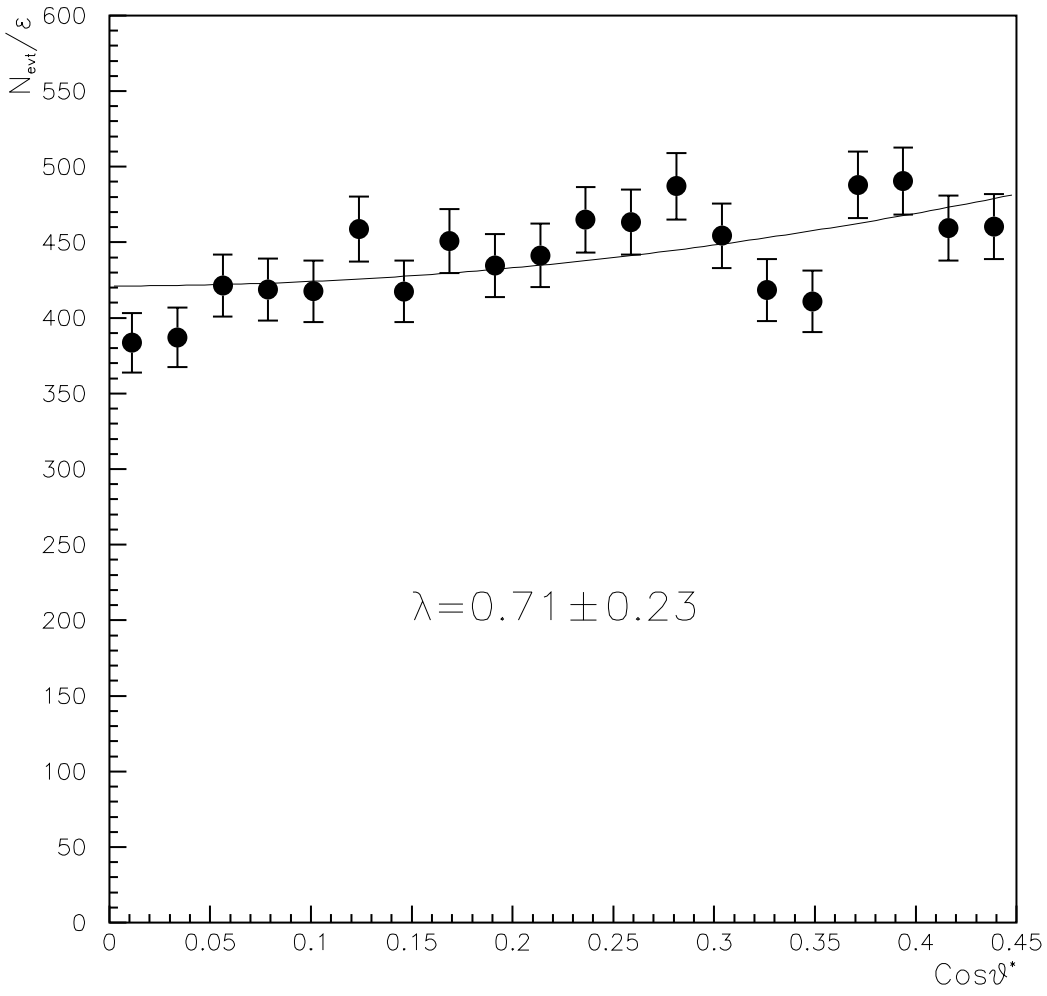

Figure 5.5: Distribution of the number of events corrected for detection efficiency as a function of $cos(\theta^*)$; the best fit function is superimposed on the data points. The error bars are statistical.

5.3 Conclusion

We have measured the branching ratios $B(\psi' \to e^+e^-)$, $B(\psi' \to J/\psi\pi^+\pi^-)$, $B(\psi' \to J/\psi\pi^0\pi^0)$ and $B(\psi' \to J/\psi\eta)$, obtaining:

$$\begin{aligned} B(\psi' \to e^+e^-) &= (6.3 \pm 0.1 \pm 0.4) \times 10^{-3} \\ B(\psi' \to J/\psi\pi^+\pi^-) &= (30.3 \pm 0.5 \pm 1.8) \times 10^{-2} \\ B(\psi' \to J/\psi\pi^0\pi^0) &= (17.1 \pm 0.5 \pm 1.1) \times 10^{-2} \\ B(\psi' \to J/\psi\eta) &= (2.7 \pm 0.2 \pm 0.3) \times 10^{-2} \end{aligned}$$

Our measurements are in general agreement with previous measurements and in particular with the PDG02 fit values. An exception is the $\psi' \to e^+e^-$ channel, which shows a deviation larger than 2σ from the PDG02 estimate.

We measured the angular distribution parameter $\lambda(\psi')$ for the ψ' formed in $\overline{p}p$ annihilations and we obtained:

$$\lambda(\psi') = 0.71 \pm 0.23$$

This result confirms the measurement of the same parameter previously made by E760.

Appendix A

The electron weight index

A.1 Introduction

The electron weight ew is a test variable used to identify $e^{\pm}$ from charmonium decays. The background to $\overline{c}c \rightarrow e^+e^-X$ comes from coalescing e^+e^- pairs from photon conversions and π^0 Dalitz decays, and from charged hadrons. The probabilities of a π^0 Dalitz decay and a γ conversion before the innermost hodoscope $H1$ are about 1.2% and 1.5% respectively [67]; such events are produced primarily from the relatively abundant processes $\overline{p}p \rightarrow \pi^0\pi^0 \rightarrow 4\gamma$ and $\overline{p}p \rightarrow \pi^0\gamma \rightarrow 3\gamma$. The background e^+e^- pairs generate a larger signal in the hodoscopes and in the Čerenkov counter, with respect to a single $e^{\pm}$ track from $\overline{c}c$; the CCAL shower profile is wider, for coalescing e^+e^-. A final state with two hadrons can simulate a e^+e^- event if a Čerenkov signal is present and a CCAL shower is produced. The process $\overline{p}p \rightarrow \pi^+\pi^-$ is the largest source of such events. Since the CCAL shower shapes, the pulse heights in the hodoscopes and the pulse heights in the Čerenkov counter differ between background and e^+e^- from charmonium, it is possible to build a test variable for background rejection using the appropriate quantities.

A.2 The Neyman-Pearson test

Given a random variable $\vec{x} = (x_1, x_2, \ldots, x_n)$ with probability distribution function $f_n(\vec{x}, \vec{\xi})$ and a parameter space $\vec{\xi} = (\xi_0, \xi_1)$ with only two points, the significance α for a test of the null hypothesis H_0 against an alternative hypothesis H_1 is:

$$\int_{w_\alpha} f_n(\vec{x}, \xi_0) d\vec{x} = \alpha \tag{A.1}$$

The power of the test is defined as:

$$\int_{w_\alpha} f_n(\vec{x}, \xi_1) d\vec{x} = 1 - \beta \tag{A.2}$$

Once we choose α, the critical region w_α[1] which maximizes the power of the test is given by the observation points which satisfy:

$$\rho_n(\vec{x}, \xi_0, \xi_1) \equiv \frac{f_n(\vec{x}, \xi_1)}{f_n(\vec{x}, \xi_0)} \geq \eta_\alpha \tag{A.3}$$

where η_α is chosen so as to satisfy eq. A.1. $\rho(\vec{x}, \xi_0, \xi_1)$ is the ratio between the likelihoods for the two hypotheses. The procedure for the choice between H_0 and H_1 is:

$$Choose \begin{cases} H_1 & : \quad \rho_n(\vec{x}, \xi_0, \xi_1) > \eta_\alpha \\ H_0 & : \quad \rho_n(\vec{x}, \xi_0, \xi_1) \leq \eta_\alpha \end{cases}$$

If $f_n(\vec{x}, \xi)$ is known, the optimal discrimination criterion is $\rho_n(\vec{x}, \xi_0, \xi_1) > 1$.
If $H_{0,1}$ are verified conditionally with unknown probabilities $P_{H_0}(\epsilon_0)$ and $P_{H_1}(\epsilon_1)$ it is still possible to discriminate between H_0 and H_1 using the modified classifier:

$$\rho'_n(\vec{x}, \xi_0, \xi_1) \equiv \frac{g_n(\vec{x}, \xi_1)}{g_n(\vec{x}, \xi_0)} \tag{A.4}$$

where $f_n(\vec{x}, \xi_{0,1}) = g_n(\vec{x}, \xi_{0,1}) P_{H_{0,1}}(\epsilon_{0,1})$. In this case one needs to choose empirically a suitable minimum value for ρ'. In E835 H_0 is the background hypothesis and H_1

[1]The region of the observation space where H_0 is rejected

the electron signal hypothesis, therefore we change the notation as $g_n(\vec{x}, \xi_0) \equiv g_b(\vec{x})$ and $g_n(\vec{x}, \xi_1) \equiv g_e(\vec{x})$.

A.3 Building the ew index

The measured quantities $\vec{x}$ used in the ew are:

- $H1$, $H2'$ and $H2$ pulse heights[2]

- Čerenkov pulse height[3]

- CCAL cluster 2^{nd} moments along rings and wedges:

$$s_r = \frac{\sum_{r,w=1}^{3} E(r,w) * (w - w_0)^2}{\sum_{r,w=1}^{3} E(r,w)}$$
$$s_w = \frac{\sum_{r,w=1}^{3} E(r,w) * (r - r_0)^2}{\sum_{r,w=1}^{3} E(r,w)}$$

- $S_{35} \equiv E_{3\times3}/E_{5\times5}$, where $E_{n\times n}$ is the energy deposited in a CCAL cluster formed with $n \times n$ blocks around the maximum energy block.
- S_{24}, same as above with 2×2 and 4×4 clusters.
- *Cluster mass*, defined as $M_{cl} \equiv \sqrt{(\sum_{i=1}^{2} 5E_i)^2 - (\sum_{i=1}^{2} 5\vec{p}_i)^2}$, where E_i is the energy deposited in the i^{th} CCAL block of a 5×5 cluster, $\vec{p}_i \equiv E_i \hat{r}_i$ and $\hat{r}_i$ is a unit vector pointing from the interaction vertex to the center of the i^{th} block.

[2]The hodoscopes' response is calibrated to compensate for the dependence on the polar angle θ.

[3]Corrected for the dependence on θ and on the photoelectron yield of different mirrors

Assuming that all these variables are uncorrelated, $g_{e,b}$ are defined as the product of the normalized measured distributions of each variable, for signal and for background tracks. The ew is defined as:

$$ew = \prod_{i=1}^{N_v} \frac{g_e^i(x_i)}{g_b^i(x_i)} \tag{A.5}$$

The probability distribution functions $g(x_i)$ are determined from data analysis; a clean sample of ψ and χ_2 is selected to determine $g_e^i(x_i)$, while for $g_b^i(x_i)$ we use data taken in the CM energy region $3590 \div 3660$ MeV.

A.4 Use of the ew in E835

The events on which we want to operate the background rejection with the ew have a e^+e^- pair in the final state. We usually cut on the product of the ew indexes of the electron and positron. The cut value is determined case by case looking at the background vs signal distribution; the cut is chosen so as to maximize the signal-to-background ratio. Fig. A.1 shows the logarithm of the product of electron weights for background and e^+e^- from charmonium decay events. The background events are from 50.5 pb^{-1} of integrated luminosity in the CM energy region $3523 \div 3529$ MeV. The signal is a clean sample of $\psi' \to e^+e^-$ selected without ew cuts. The efficiency of the ew cut gets lower at higher cut values; in the range of cut values used in E835 analysis the efficiency is above 90%. Plots of the pdfs, cut efficiency, rejection curves and additional information about the ew can be found in ref. [70].

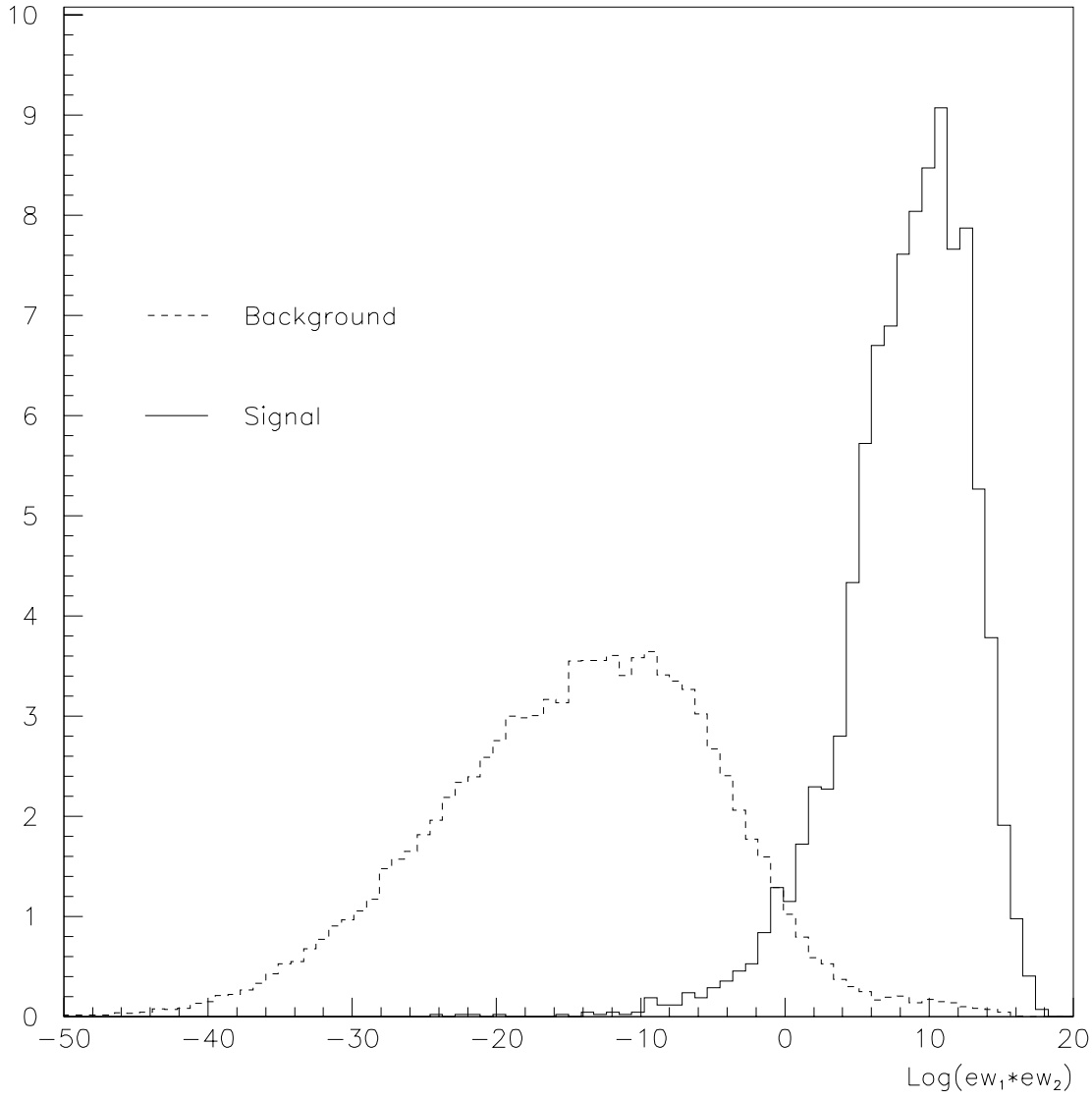

Figure A.1: Logarithm of the product of electron weigths, for signal e^+e^- and for background.

Appendix B

The GEANT Monte Carlo

This appendix contains a comparison between the GEANT Monte Carlo and the data for some variable distributions of interest for this analysis.

The GEANT [12] package simulates the passage of elementary particles through the matter; it is widely used in high energy physics. The detector medium is defined through its geometry and the material filling the various parts of the detector structure. The interactions of the particle with matter are taken into account according to the geometry, the material and the physical characteristics (such as magnetic fields, for example) of the detector region they are passing through. The trajectories of the particle are recorded, as well as the response of the active material to the interaction with the particle.

The plots included in this appendix show events after final selection. The distributions are presented as data variable histograms (solid line) with superimposed Monte Carlo histograms (dashed line). Fig. B.1 shows the invariant mass of the e^+e^- from ψ' and from J/ψ. The $M_{e^+e^-}$ shows a shift towards lower values with respect to the expected *psip* and J/ψ masses. This effect is not completely understood yet, but it does not affect in any dangerous way this analysis. This shift is most likely due to the fact that in E835 the CCAL calibration is optimized for neutral final states, and

charged final states are not used in the calibration procedure. Fig. B.2 shows the sum of the energies of the e^+e^-; the data distributions show a little shift towards lower energies with respect to the Monte Carlo. A slight shift between data and MC can be appreciated also in the cluster mass distributions, in fig. B.3. The top two plots in fig. B.4 show the π^0 and η mass from $J/\psi\pi^0\pi^0$ and $J/\psi\eta$ events; the two lower plots compare the photon energies. Figg. B.5, B.6, B.7 and B.8 show the χ^2 probability distributions for the kinematical fits. A test statistic often used to perform compatibility checks of a parameter among independent estimates from different experiments is the *pull*. Details about this test variable can be found in [80]. We define it as:

$$Pull(x) = \frac{x - \xi}{\sqrt{\mid \sigma_x^2 - \sigma_\xi^2 \mid}} \tag{B.1}$$

where x is a measured variable, ξ the fitted value, σ_x is the error on x, and σ_ξ the error on ξ. The statistic B.1 is normally distributed (by assumption), with variance 1 (by construction). Figg.B.9, B.10, B.11, B.12 and B.13 show the pulls for the quantities used in the kinematical fits, i.e. energies, polar and azimuthal angles.

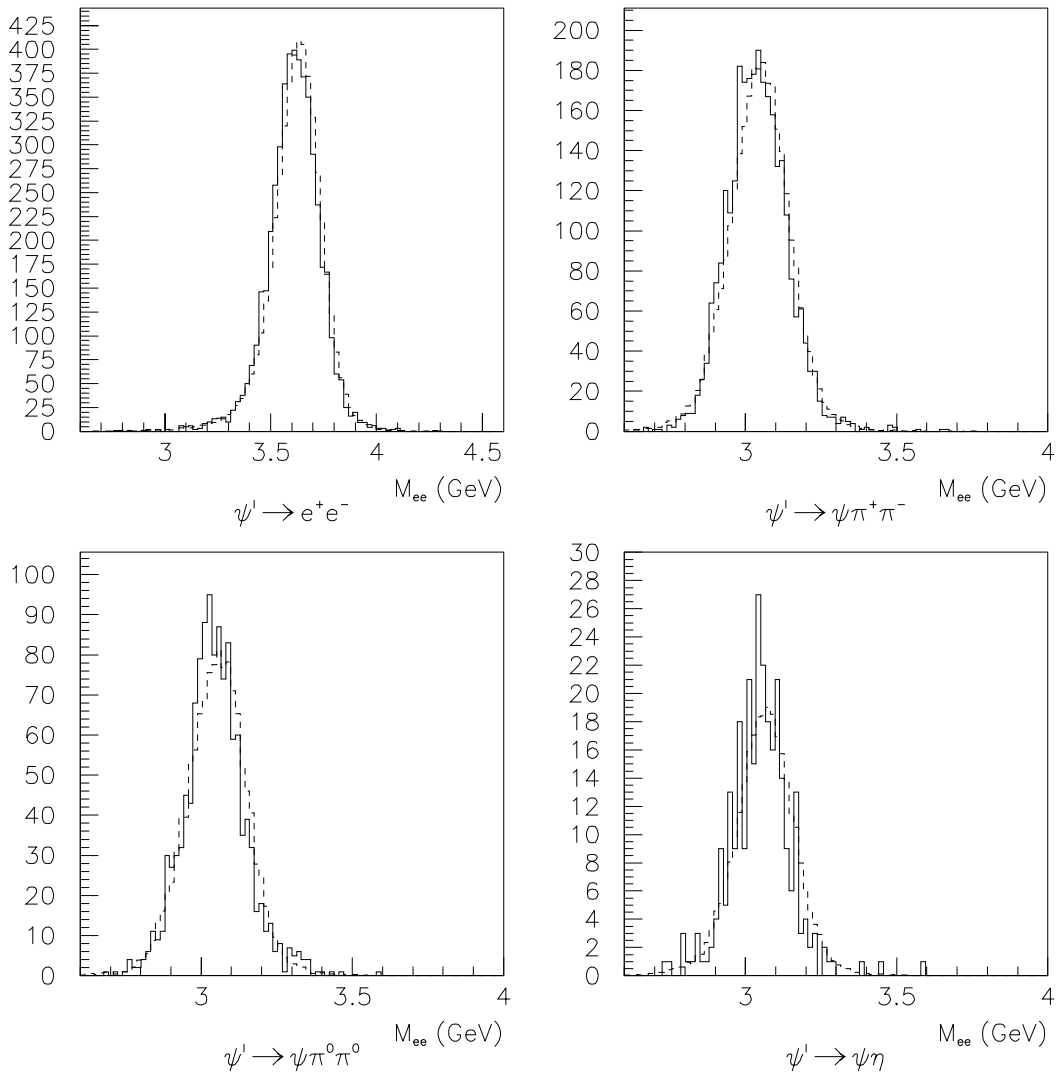

Figure B.1: Invariant mass of the e^+e^- for each decay channel, after final selection. The dashed histogram contains MC events; data events are in the solid histogram. The number of events in the MC histogram is normalized to the number of data events.

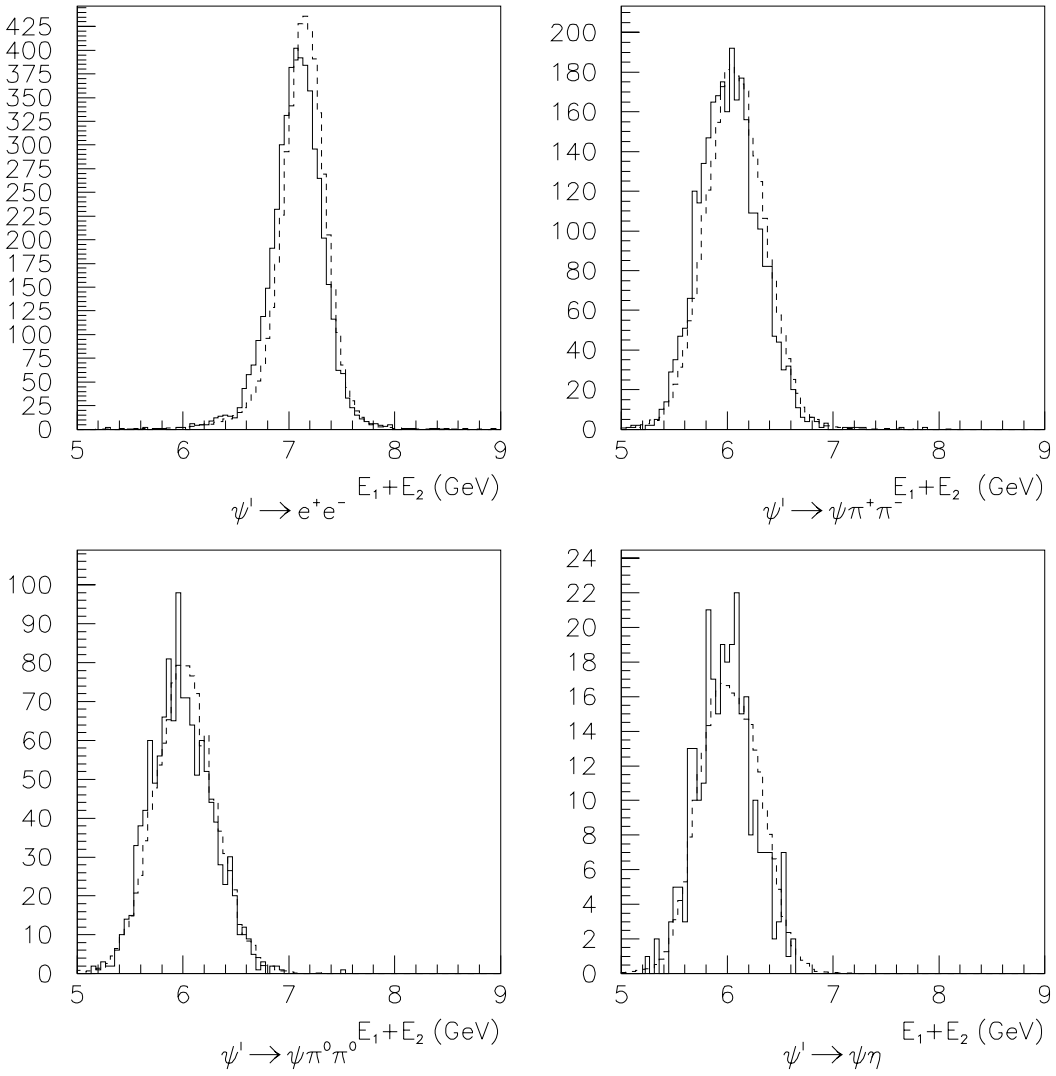

Figure B.2: Sum of the CCAL measured energies of the e^+e^- for each decay channel, after final selection. The dashed histogram contains MC events; data events are in the solid histogram. The number of events in the MC histogram is normalized to the number of data events.

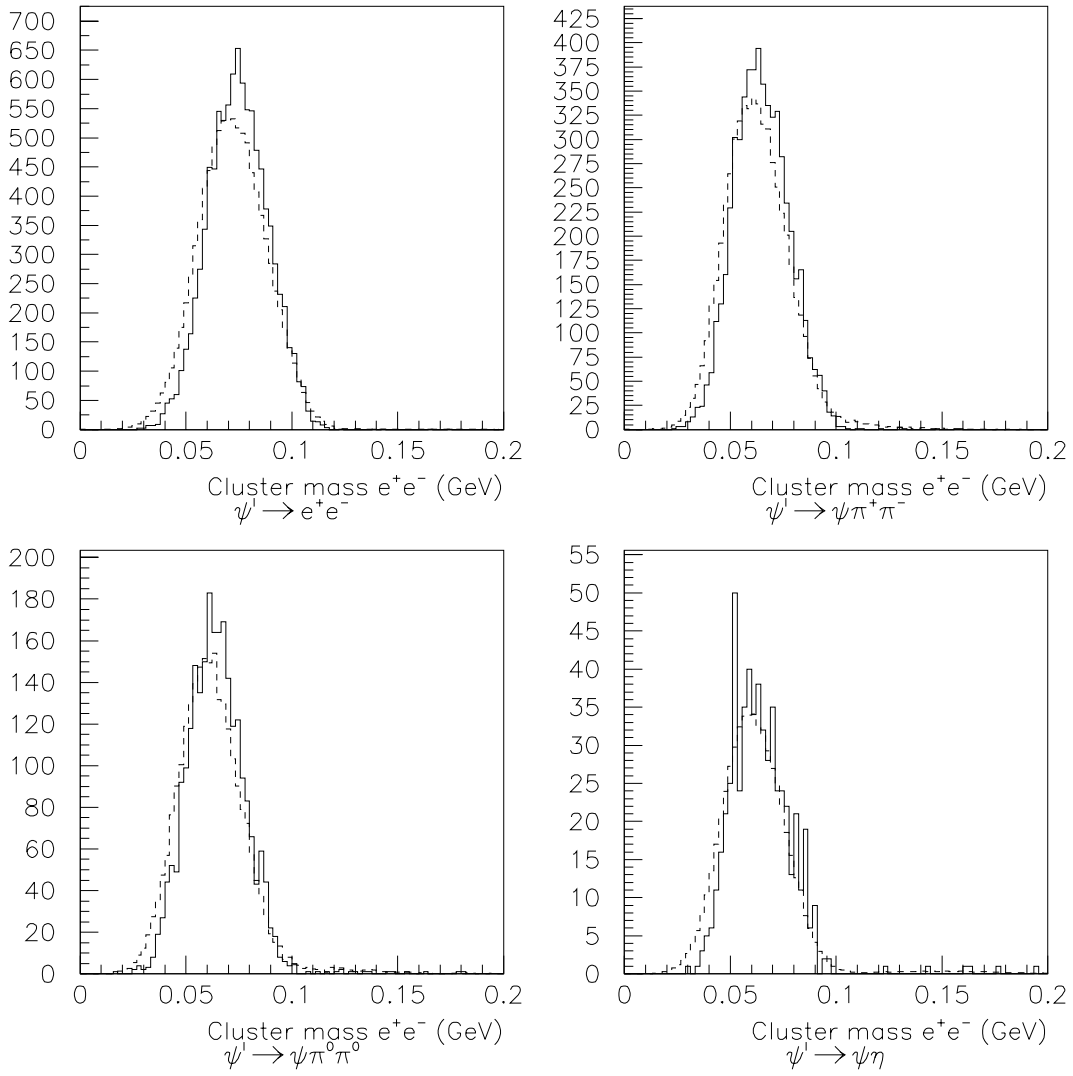

Figure B.3: Cluster mass of the e^+e^- for each decay channel, after final selection. The dashed histogram contains MC events; data events are in the solid histogram. The number of events in the MC histogram is normalized to the number of data events.

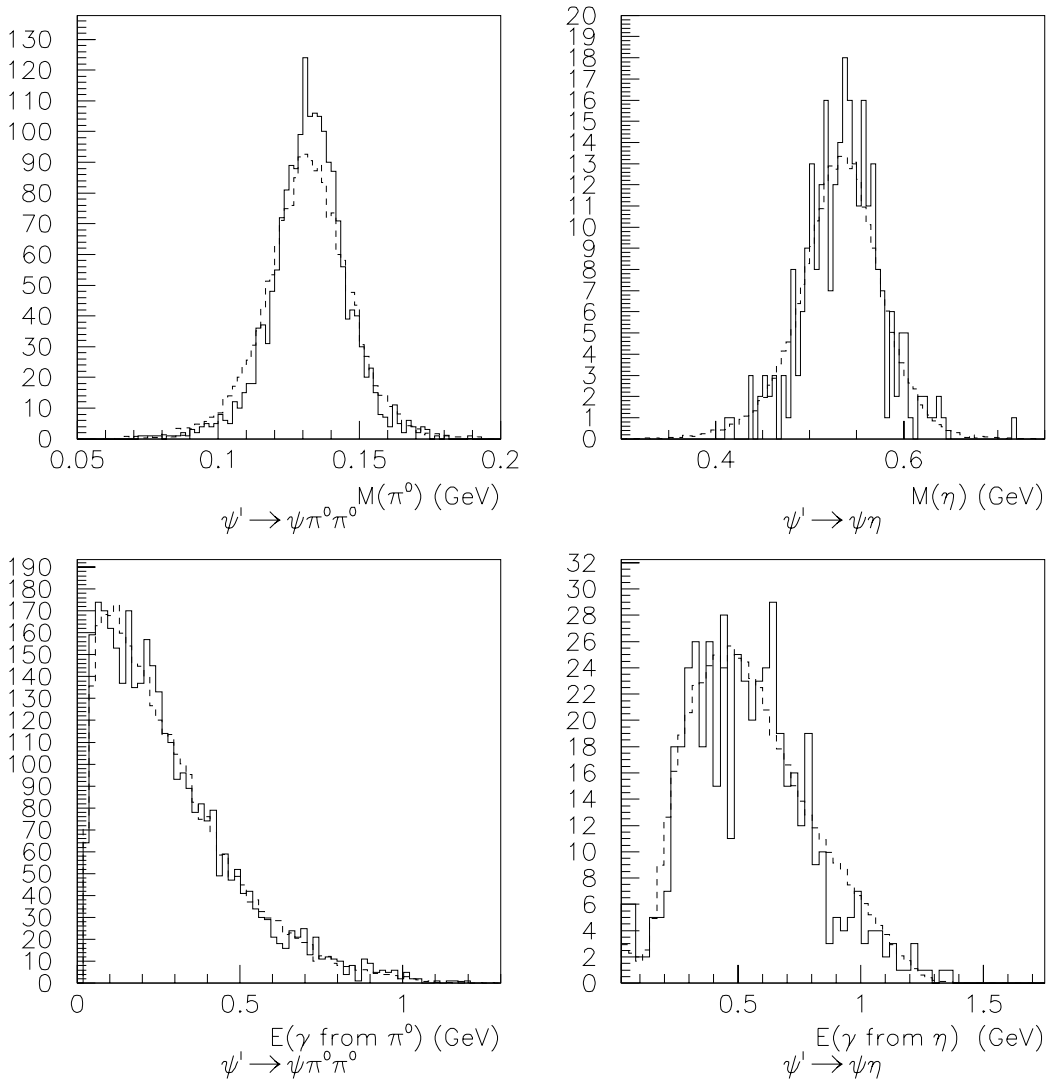

Figure B.4: The top two plots show the mass of the π^0 from $\psi' \to J/\psi\pi^0\pi^0$ and the mass of the η from $\psi' \to J/\psi\eta$ events after final selection. The two bottom plots show the energies of the gammas from the π^0s and ηs in the top plots. The dashed histogram contains MC events; data events are in the solid histogram. The number of events in the MC histogram is normalized to the number of data events.

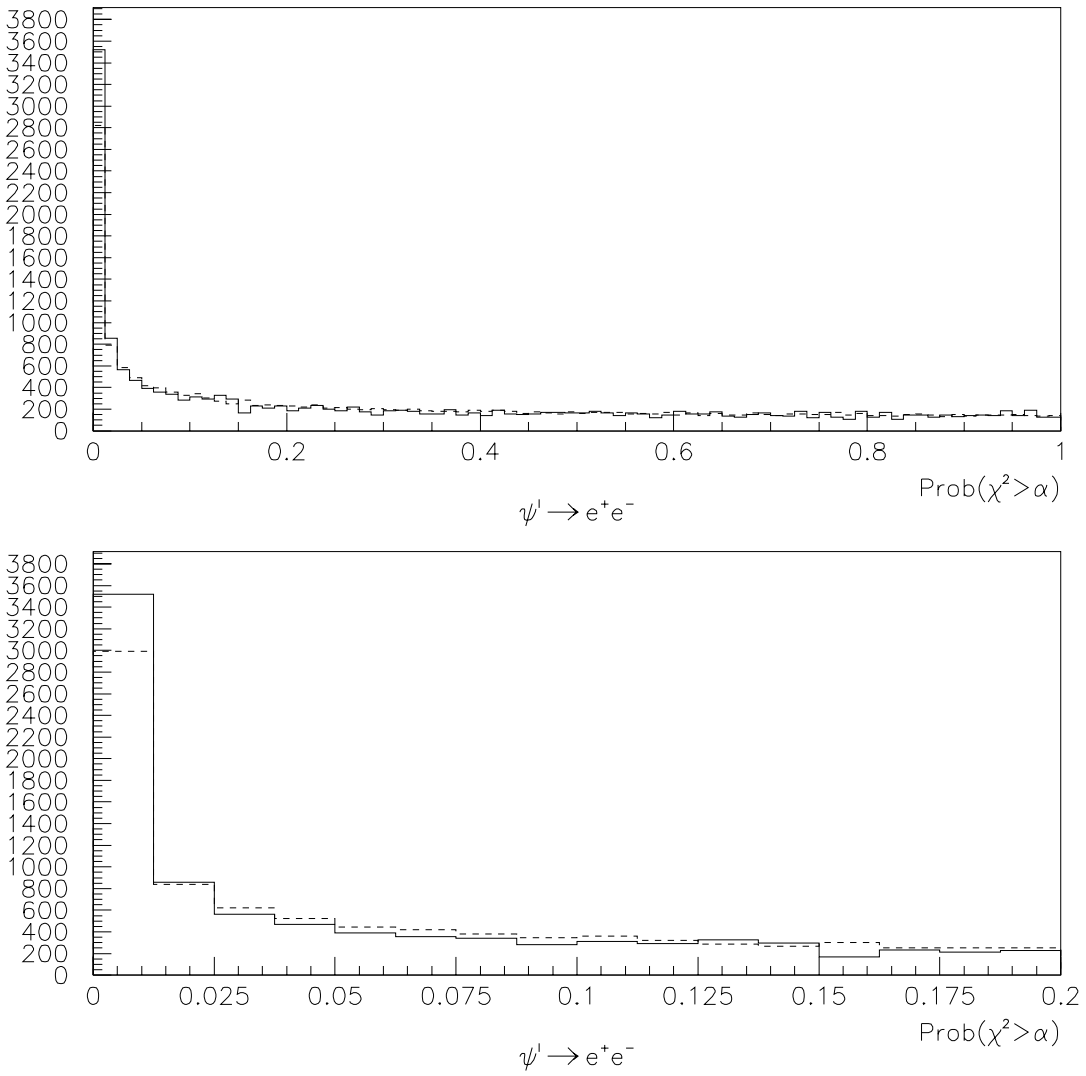

Figure B.5: Probability of the χ^2 for the kinematical fit to the channel $\psi' \rightarrow e^+e^-$. The bottom plot shows an enlargement of the lower $Prob(\chi^2)$ region from the top plot. The dashed histogram contains MC events; data events are in the solid histogram. The number of events in the MC histogram is normalized to the number of data events.

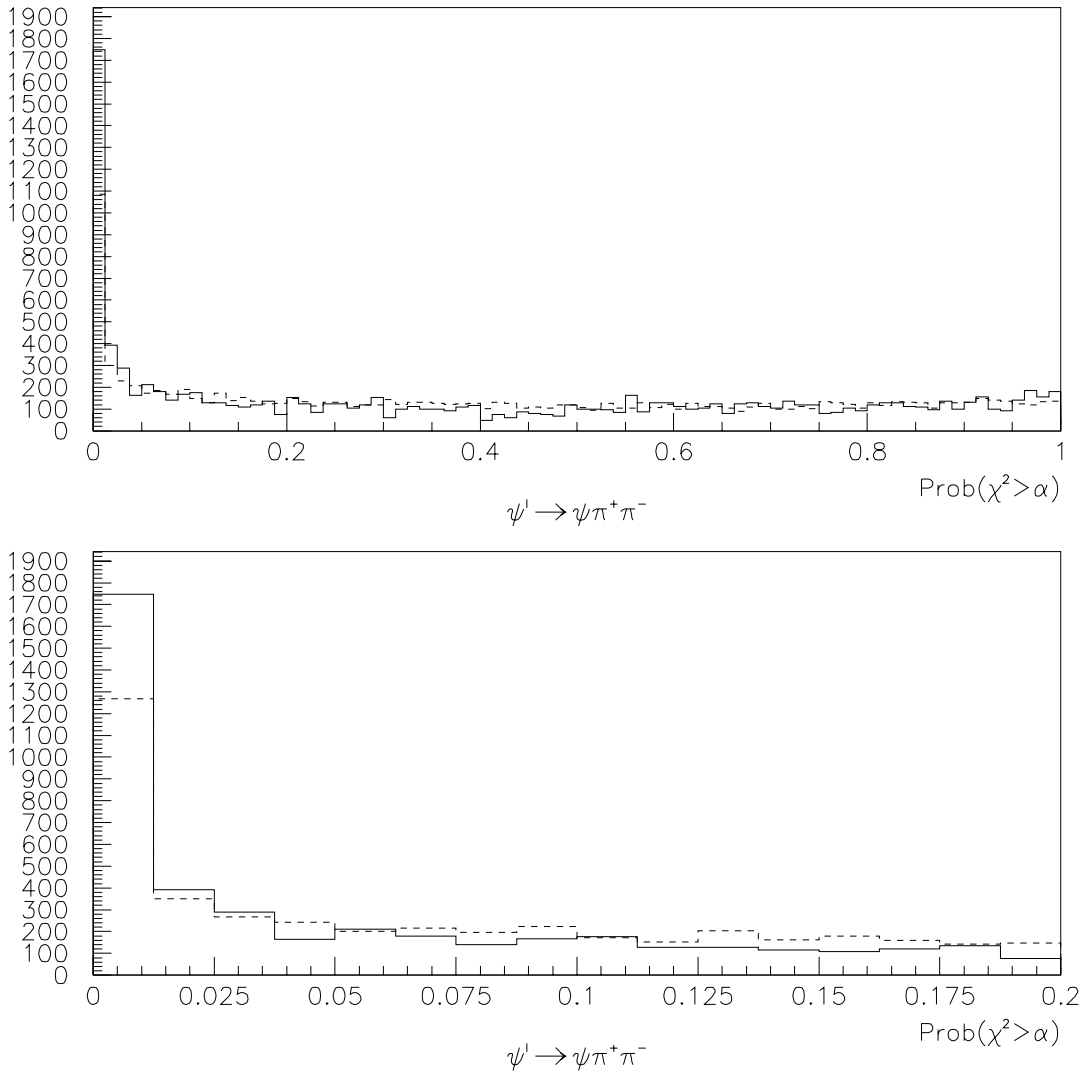

Figure B.6: Probability of the χ^2 for the kinematical fit to the channel $\psi' \to J/\psi\pi^+\pi^-$. The bottom plot shows an enlargement of the lower $Prob(\chi^2)$ region from the top plot. The dashed histogram contains MC events; data events are in the solid histogram. The number of events in the MC histogram is normalized to the number of data events.

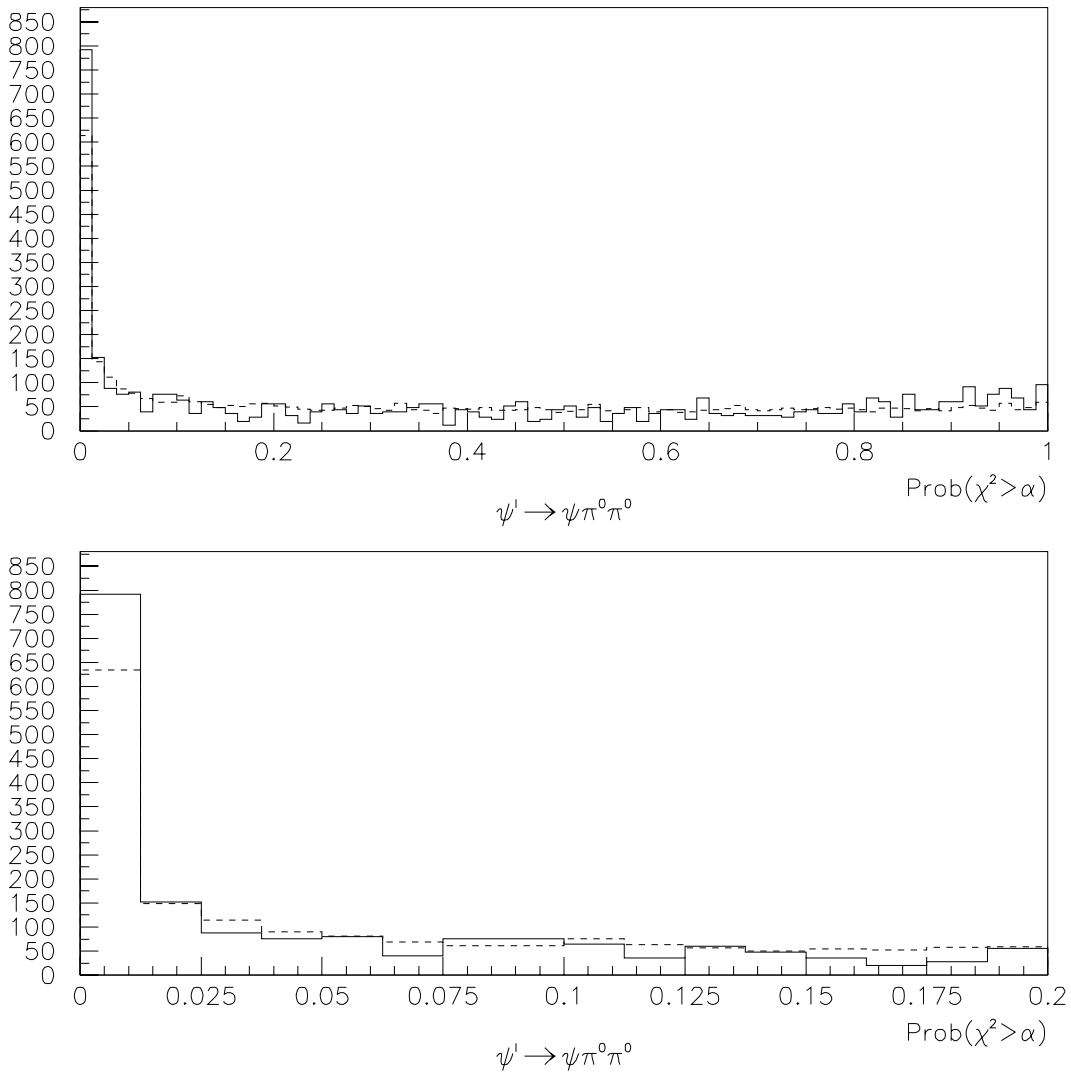

Figure B.7: Probability of the χ^2 for the kinematical fit to the channel $\psi' \to J/\psi\pi^0\pi^0$. The bottom plot shows an enlargement of the lower $Prob(\chi^2)$ region from the top plot. The dashed histogram contains MC events; data events are in the solid histogram. The number of events in the MC histogram is normalized to the number of data events.

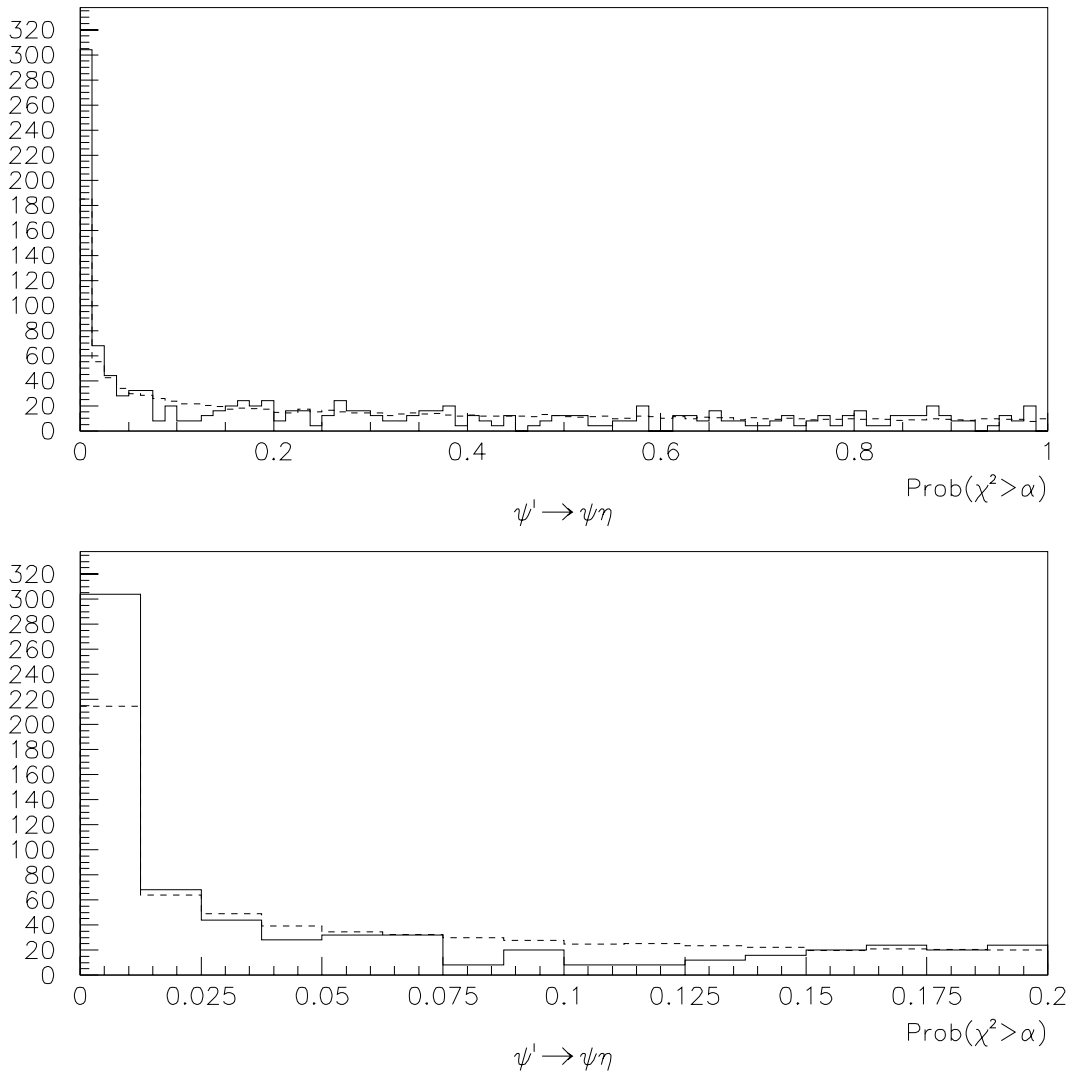

Figure B.8: Probability of the χ^2 for the kinematical fit to the channel $\psi' \to J/\psi\eta$. The bottom plot shows an enlargement of the lower $Prob(\chi^2)$ region from the top plot. The dashed histogram contains MC events; data events are in the solid histogram. The number of events in the MC histogram is normalized to the number of data events.

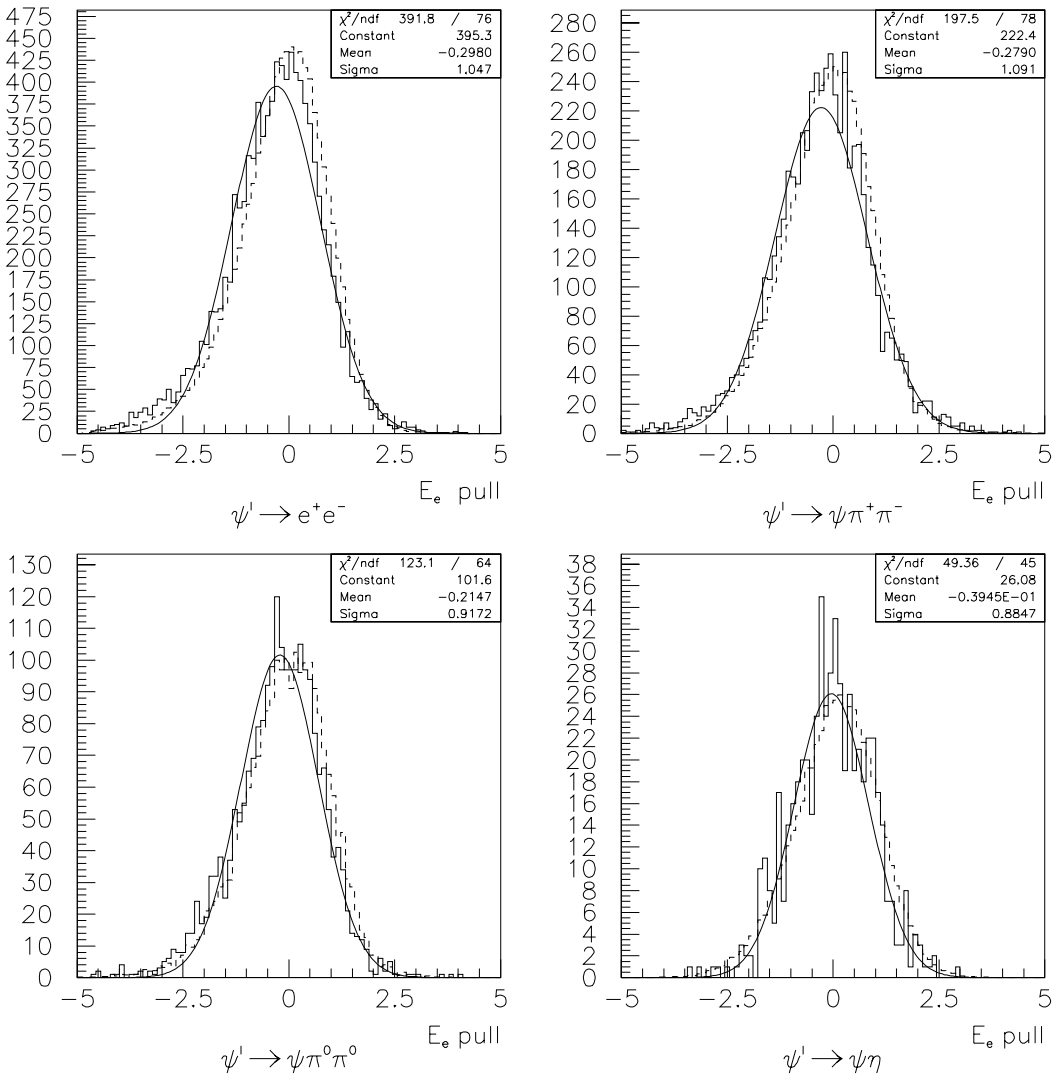

Figure B.9: Pulls for the energy of the e^+e^- in each of the channels. The gaussian fit to the data distribution is included in each plot. The dashed histogram contains MC events; data events are in the solid histogram. The number of events in the MC histogram is normalized to the number of data events.

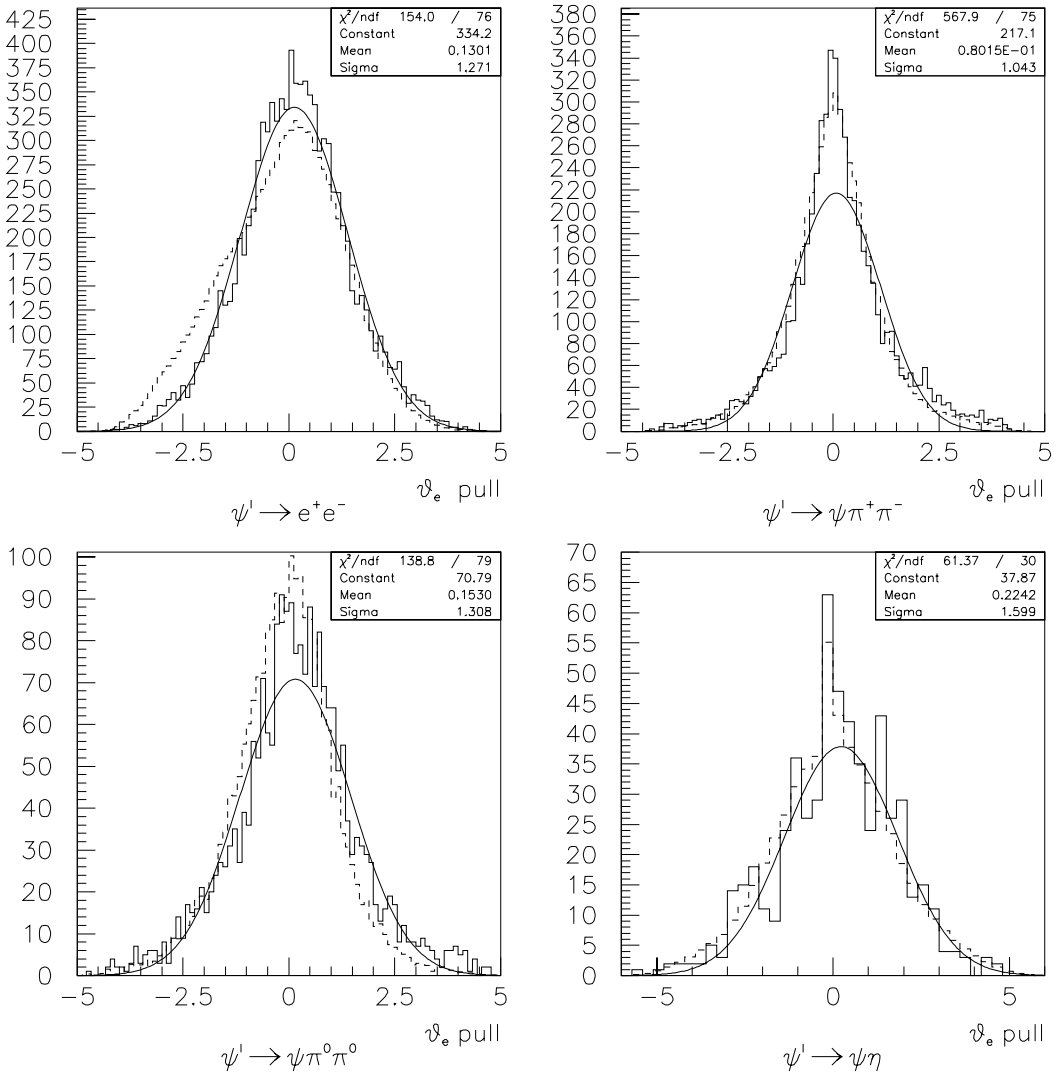

Figure B.10: Pulls for the θ angle of the e^+e^- in each of the channels. The gaussian fit to the data distribution is included in each plot. The dashed histogram contains MC events; data events are in the solid histogram. The number of events in the MC histogram is normalized to the number of data events.

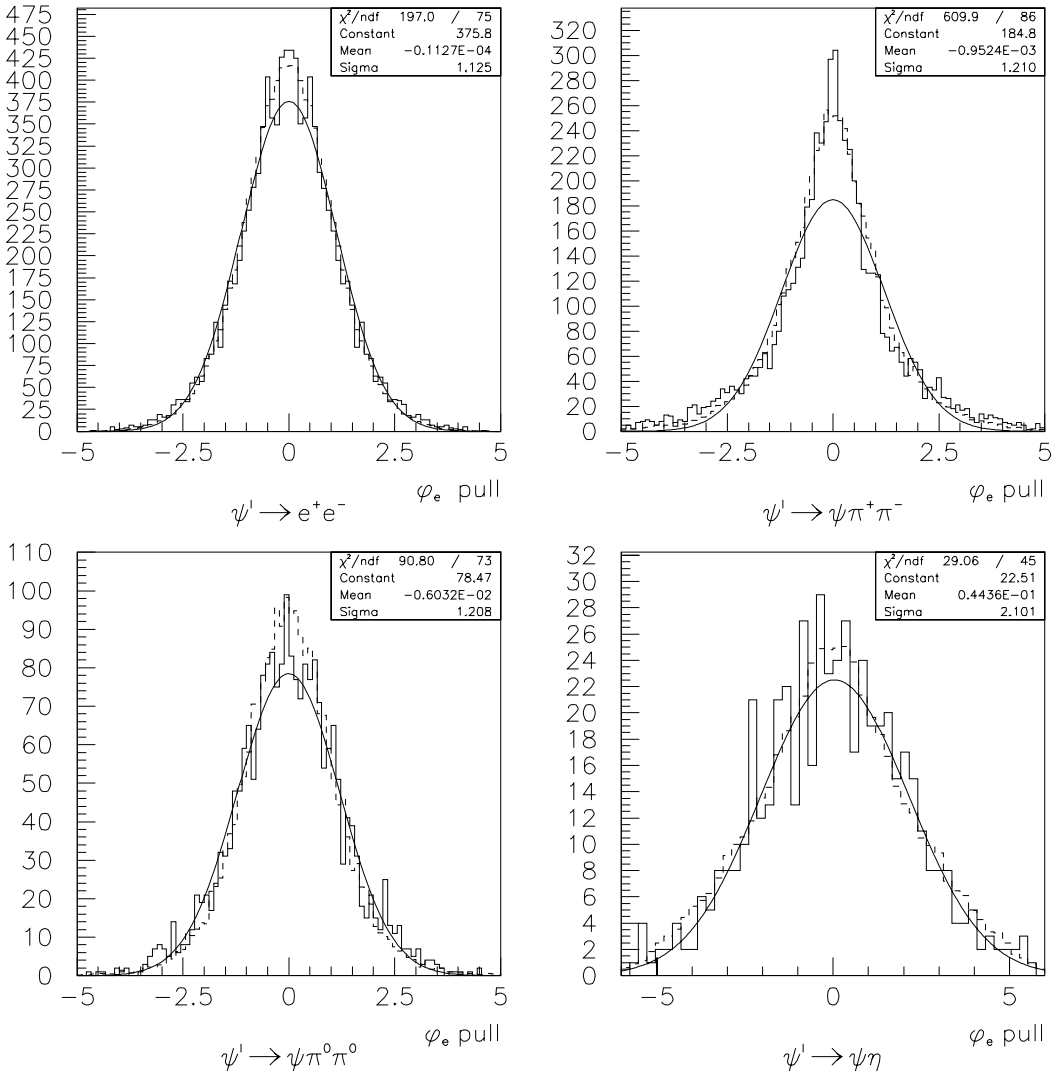

Figure B.11: Pulls for the ϕ angle of the e^+e^- in each of the channels. The gaussian fit to the data distribution is included in each plot. The dashed histogram contains MC events; data events are in the solid histogram. The number of events in the MC histogram is normalized to the number of data events.

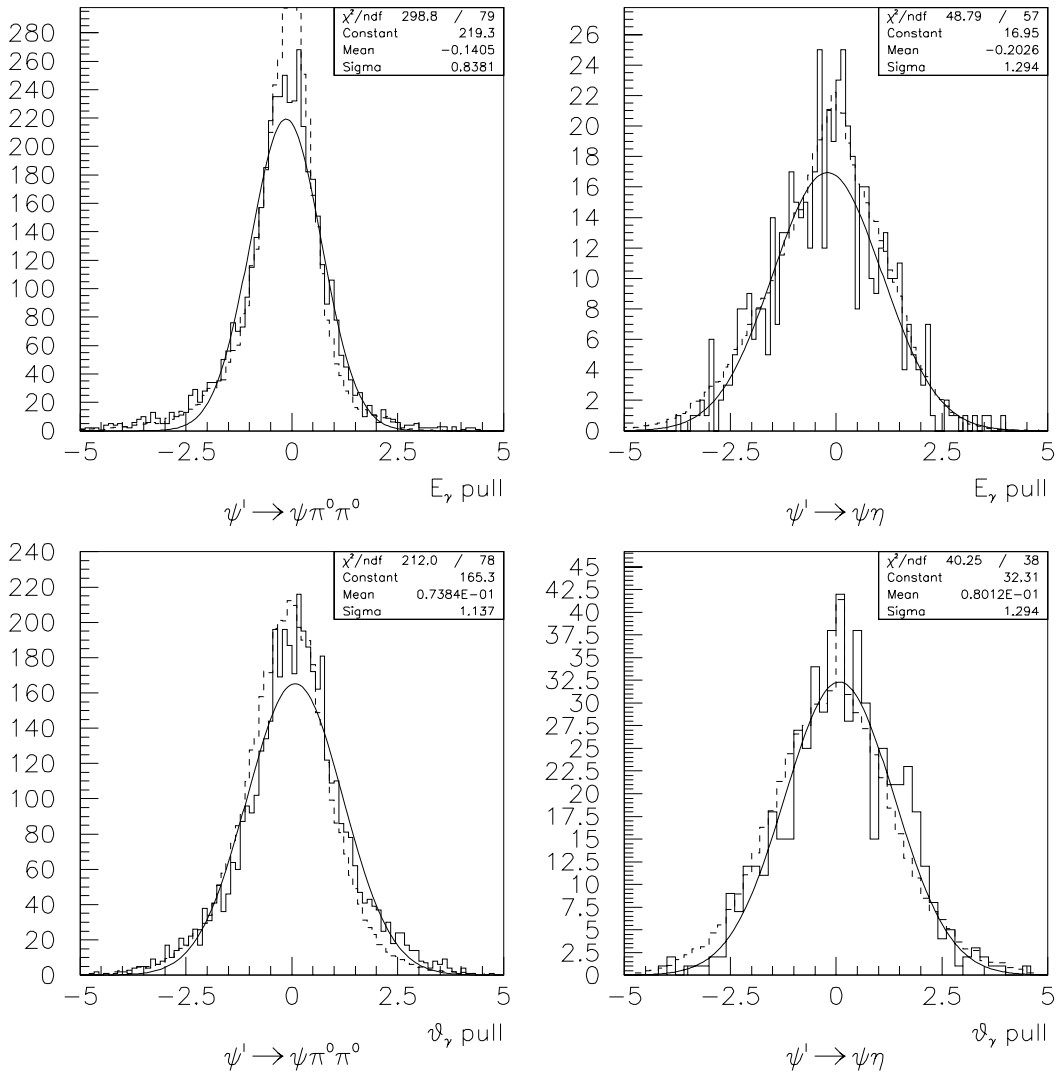

Figure B.12: Pulls for the energy and θ angle of the γs in the channels $\psi' \to J/\psi\pi^0\pi^0$ and $\psi' \to J/\psi\eta$. The gaussian fit to the data distribution is included in each plot. The dashed histogram contains MC events; data events are in the solid histogram. The number of events in the MC histogram is normalized to the number of data events.

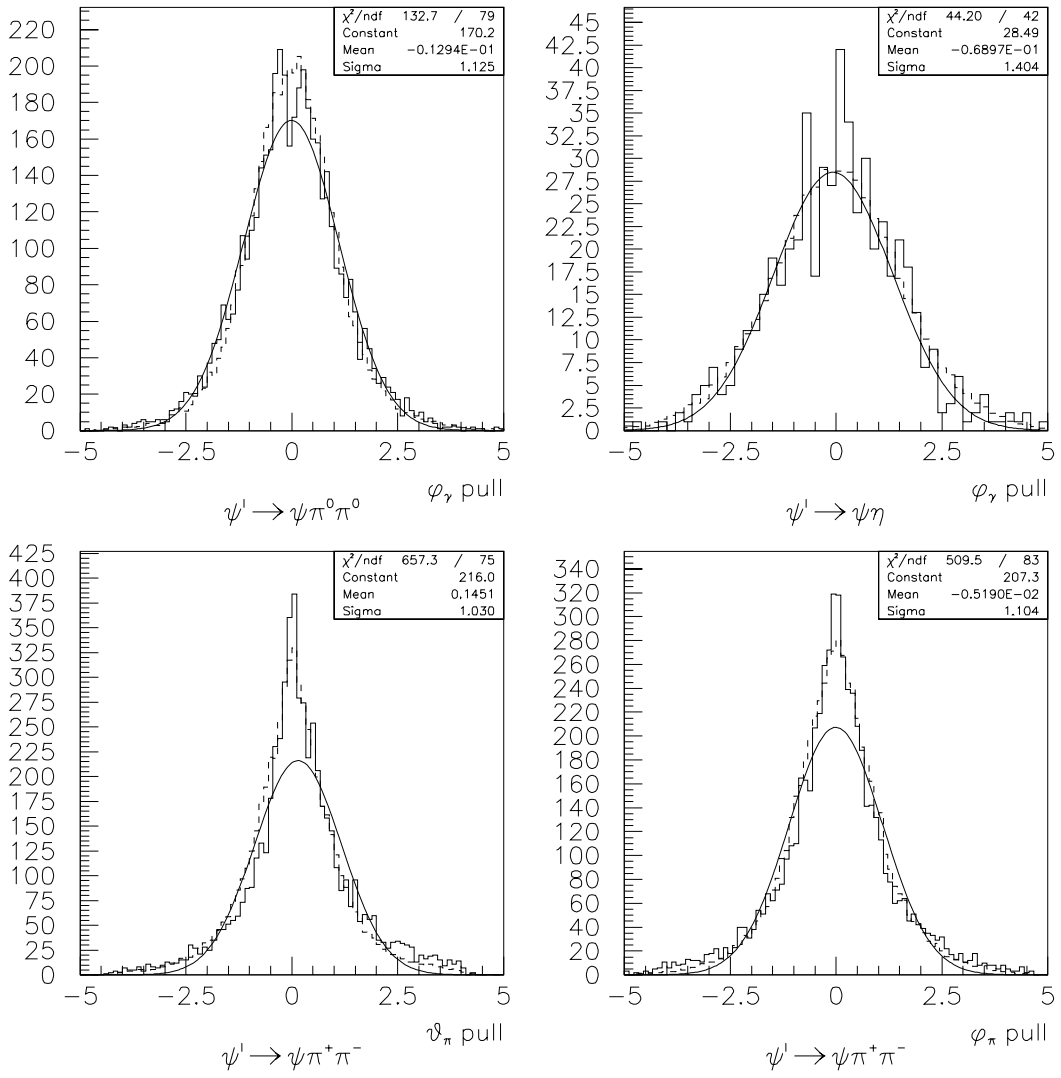

Figure B.13: The top plots show the pulls for the ϕ angle of the γs in the channels $\psi' \to J/\psi\pi^0\pi^0$ and $\psi' \to J/\psi\eta$; the bottom two show the pulls for the θ and ϕ angles in $\psi' \to J/\psi\pi^+\pi^-$. The gaussian fit to the data distribution is included in each plot. The dashed histogram contains MC events; data events are in the solid histogram. The number of events in the MC histogram is normalized to the number of data events.

Appendix C

Event reconstruction in CCAL

C.1 CCAL clustering

The energy released by a particle in the CCAL is measured from the signals generated in a group (*cluster*) of lead-glass counters. The $e.m.$ shower generated when an $e^{\pm}$ or a γ hits the CCAL is usually contained within a box of 3x3 counters, centered on the block with the highest energy deposit. The *clusterizer* is the algorithm that builds clusters generated by a single particle. The first step is to find the blocks with the local maxima, or *seed* blocks; these are the counters with energy deposit higher than the 8 nearest neighboring blocks. At this stage the seeds are considered the cluster centers. The distance between the cluster centers is calculated, and depending on how close two seeds are, they are sent to different routines to form a cluster, depending on the energy deposition configuration; these routines implement the *isolated shower*, the *energy sharing* and the *cluster splitting* algorithms. The isolated shower routine is used to measure the energy and the position in θ and ϕ of a particle using a 3x3 box around the seed, provided there is no overlap with another cluster, i.e. there are no blocks in common. Sometimes two clusters do overlap, usually in the case of symmetric π^0 decays. In this case the energy contained in the blocks common

to the two clusters must be shared; this operation is carried out by the energy sharing routine. In some cases it happens that the photons from a symmetric π^0 decay hit two neighboring blocks, and the energy of the two gammas is merged into a single cluster. For such events, the *e.m.* shower extends beyond the 3x3 box; this feature can be used to tag these events and send them to the cluster splitting routine.

Isolated showers

The position of a cluster is calculated in two steps. First the track position is expressed as the energy weighted average in units of number of blocks with respect to the seed block, in a 3x3 grid around the center block:

$$x = \frac{\sum_{i=1}^{9} E_i x_i}{\sum_{i=1}^{9} E_i},\ y = \frac{\sum_{i=1}^{9} E_i y_i}{\sum_{i=1}^{9} E_i} \tag{C.1}$$

where E_i is the energy deposited in the i^{th} block and $x_i, y_i = (-1, 0, 1)$. The second step involves correcting the cluster centroid coordinates (x, y) using a parametrization of the transverse shower profile:

$$x' = N_x \left[A_w a_w (1 - e^{-x/a_w}) + B_w b_w (1 - e^{-x/b_w})\right] \tag{C.2}$$

$$y' = N_y \left[A_r a_r (1 - e^{-y/a_r}) + B_r b_r (1 - e^{-y/b_r})\right] \tag{C.3}$$

$$N_x = 0.5 \left[A_w a_w (1 - e^{-0.5/a_w}) + B_w b_w (1 - e^{-0.5/b_w})\right] \tag{C.4}$$

$$N_y = 0.5 \left[A_r a_r (1 - e^{-0.5/a_r}) + B_r b_r (1 - e^{-0.5/b_r})\right] \tag{C.5}$$

where x' and y' are the distances in block units in the wedge and ring directions respectively, from the center of the seed block. The constants $A_{w,r}, B_{w,r}, a_{w,r}, b_{w,r}$ are measured with $J/\psi \rightarrow e^+e^-$ events. The energy of an isolated cluster is the sum of the energy deposited in the seed block and the 8 nearest neighboring blocks. The CCAL counters are separated by septa of passive material (steel partitions); this causes some energy to be lost, so that it is necessary to apply a correction depending

A_r	724.4	a_r	0.03208
A_w	706.5	a_w	0.03969
B_r	123.6	b_r	0.1860
B_w	102.6	b_w	0.1715
C_l	0.0614	X_l	7.367
C_h	0.0857	X_h	19.690
D_1	0.14736	Y_1	48.908
D_2	0.15935	Y_2	12.761

Table C.1: Constants used in calculating the position and energy of CCAL showers.

on the distance of the incident track from the edge of the block. The corrected energy is given by:

$$E_{corr} = \frac{E_{meas}}{(1 - C_{h(l)} e^{-|x''|/X_{h(l)}})(1 - D_1 e^{-|y''|/Y_1} - D_2 e^{-|y''|/Y_2})} \tag{C.6}$$

where (x'', y'') is the position of the track measured from the edge of the block, in block units. $C_{h(l)}$[1] and $D_{1,2}$ are empirically determined parameters (see table C.1).

Cluster energy sharing

When two clusters share one or more blocks, the energy in the shared blocks must be assigned to each cluster according to an appropriate weight, determined iteratively. The sum of the weights for a given block has to be equal to 1. The iteration evaluates the weights each time new positions and energies are calculated with new weights; the iteration is terminated when stable values of position and energy of the two clusters are reached[2]. The iteration proceeds as follows:

[1]The index h is chosen when the particle hits the upper half of the block (higher θ); l is chosen in the lower half (lower θ).

[2]Convergence is defined as $\Delta E < 30$ MeV and $\Delta\theta(\phi) < 30\ mrad$; in most cases convergence is reached after 2 to 4 iterations.

- the cluster energy is calculated with C.6 and the position is determined with:

$$x_j = \frac{\sum_{i=1}^{9} f_j^i E_i x_i}{\sum_{i=1}^{9} f_j^i E_i},\ y_j = \frac{\sum_{i=1}^{9} f_j^i E_i y_i}{\sum_{i=1}^{9} f_j^i E_i} \tag{C.7}$$

  where f_j^i is the weight assigned to the i^{th} block of cluster j. The initial weights are set to 1.

- the energy and position from the initial estimate are used to evaluate the weights with:

$$f_j^i = \frac{E_j e^{-(|\delta x_{ij}|+|\delta y_{ij}|)/0.17}}{E_1 e^{-(|\delta x_{i1}|+|\delta y_{i1}|)/0.17} + E_2 e^{-(|\delta x_{i2}|+|\delta y_{i2}|)/0.17}} \tag{C.8}$$

  where $j = 1, 2$ is the cluster index, i is the block index in the 5x5 box, $\delta x_{ij}(y_{ij})$ is the distance of the center of the i^{th} block from the j^{th} cluster center block, and E_j is the energy of the j^{th} cluster. The energy of the cluster centers is never shared. With the new weights the process goes back to the first step, where position and energy are recalculated and the steps repeated until convergence is reached.

The decay length in C.8 is due to the negative exponential form of the shower profile; the value of 0.17 is empirically estimated with a sample of $J/\psi \to e^+e^-$ events.

Cluster splitting

The photons coming from a symmetric $\pi^0 \to \gamma\gamma$ decay can hit two diagonally neighboring blocks. In this case one of the two seed blocks will not be recognized as such by the main clusterizing algorithm, and the two $e.m.$ showers will be merged into one cluster. However, the energy deposition for such events is such that the cluster mass[3] is greater than 120 MeV; therefore all the events with cluster mass higher than

[3]The cluster mass is defined in A.3.

120 MeV are split into two clusters. The splitting algorithm identifies as the first cluster center the block with the largest energy deposit; the second cluster center is the block with the largest energy deposit among the four diagonal nearest neighbors. After determining the centers of the two clusters the procedure follows the same steps as in the energy sharing routine, with the following distinctions: a 5x5 box is used instead of a 3x3, to improve energy and position resolution, and the the center blocks are not double counted.

There are three energy thresholds used by the clusterizing algorithms; they can be changed by the user depending on the type of analysis being performed. These thresholds are the *seed threshold*, the *cluster* threshold and the *split cluster* threshold. The seed threshold is the minimum energy required for a block to be considered a local maximum; typically this threshold is chosen between $5 \div 25$ MeV. The sum of the energies of a seed block and the 8 neighboring blocks must exceed the cluster threshold; the range for this threshold is usually $20 \div 50$ MeV. The split cluster threshold is the value of the cluster mass above which a cluster is split into two. The thresholds used in this analysis are: seed 25 MeV, cluster 25 MeV and split cluster 120 MeV.

C.2 CCAL calibration

We describe the details and the procedures of this calibration method in ref. [62], so we will present here just the general idea behind the *in situ* CCAL calibration procedure.

The method uses the abundant $\overline{p}p \to \pi^0\pi^0$ events recorded along with charmonium decays; the high statistics available with $\pi^0\pi^0$ events allows independent calibration of each stack. The calibration procedure consists of finding a set of *gain constants*

that take into account counter-to-counter variations in the energy response and gain drift over time.The gain constant of a CCAL channel is the conversion factor from ADC counts to energy.

The energy of each π^0 in the reaction $\overline{p}p \rightarrow \pi^0\pi^0$ can be calculated from its direction and two-body kinematics. For selected $\pi^0\pi^0$ events in the data, the predicted value of the π^0's energy and the measured ADC counts are used to construct a χ^2, which is minimized to find the best values for the gain constants.

All the counters belonging to the clusters of both decay photons are summed to obtain the measured π^0 energy, M_j

$$M_j = \sum_{i=1}^{n} g_i A_{ij} \tag{C.9}$$

where n is the number of blocks associated with the j^{th} π^0 and A_{ij} is the ADC counts recorded for the i^{th} block in the j^{th} π^0.

The χ^2 is defined as follows:

$$\chi^2 \equiv \sum_{j=1}^{N} \frac{\left(M_j - E_j\right)^2}{\sigma_j^2} \tag{C.10}$$

where E_j is the predicted energy of the π^0, calculated from the θ of the π^0, σ_j is the estimated $r.m.s.$ uncertainty in the predicted energy E_j and N is the number of π^0s.

The set of g_k that minimizes χ^2 can be obtained from the 1280 equations:

$$g_k = \frac{\sum_{j=1}^{N} \left(\frac{A_{kj}}{\sigma_j^2}\right) \left[E_j - \sum_{i=1, i\neq k}^{n} A_{ij} g_i\right]}{\sum_{j=1}^{N} \frac{A_{kj}^2}{\sigma_j^2}}. \tag{C.11}$$

The error on the gain constants is given by:

$$\sigma^2(g_k) = (\mathbf{V}^{-1})_{kk} = \sum_j \frac{A_{kj}^2}{\sigma_j^2} \tag{C.12}$$

and the correlation between gain constants is:

$$(\mathbf{V}^{-1})_{km} = \sum_j \frac{A_{kj} A_{mj}}{\sigma_j^2}. \tag{C.13}$$

Bibliography

[1] T. Appelquist and H. D. Politzer. Heavy quarks and e+e- annihilation. *Physical Review Letters*, 34:43, 1975.

[2] J. D. Bjorken and E. A. Paschos. Inelastic electron-proton and γ-proton scattering and the structure of the nucleon. *Physical Review*, 185:1975, 1969.

[3] G.T. Bodwin, E. Braaten and G.P. Lepage. Rigorous QCD analysis of inclusive annihilation and production of heavy quarkonium. *Physical Review D*, 51(3):1125, 1995.

[4] S. Brodsky and G. Lepage. Exclusive processes in perturbative quantum chromodynamics. *Physical Review D*, 22 (9):2157, 1980.

[5] S. Brodsky and G. Lepage. Helicity selection rules and test of gluon spin in exclusive QCD processes. *Physical Review D*, 24 (11):2848, 1981.

[6] W. Buchmüller and S.-H. H. Tye. Quarkonia and quantum chromodynamics. *Physical Review D*, 24(1):132, 1981.

[7] Andrzej J. Buras. Asymptotic freedom in deep inelastic processes in the leading order and beyond. *Reviews of Modern Physics*, 52:199, 1980.

[8] R. Barbieri, M. Caffo and E. Remiddi. *Nucl. Phys.*, B162:220, 1980.

[9] C. Carimalo. Quark mass effects in ψ to $B\overline{B}$ decays. *Int. J. Mod. Physics*, A2:249, 1987.

[10] E.G. Cazzoli et al. Evidence for $\Delta S{=}-\Delta Q$ currents or charmed-baryon production by neutrinos. *Physical Review Letters*, 34:1125, 1975.

[11] W. Celmaster. Lepton-width suppression of vector-meson decays. *Physical Review D*, 19(5):1517, 1979.

[12] CERN writeup W5013. *GEANT, Detector Description and Simulation Tool*, 1995.

[13] J.W. Chen and M.J. Savage. Hadronic and electromagnetic interactions of quarkonia. *Physical Review D*, 57:2837, 1998.

[14] William A. Bardeen, A. J. Buras, D. W. Duke and T. Muta. Deep-inelastic scattering beyond the leading order in asymptotically free gauge theories. *Physical Review D*, 18:3998, 1978.

[15] E. Eichten et al. Spectrum of charmed quark-antiquark bound states. *Physical Review Letters*, 34:369, 1975.

[16] A. S. Artamonov et al. *Physics Letters*, B474:427, 2000.

[17] Aguilar-Benitez et al. Review of particle properties. *Physics Letters*, 204B:1, 1988.

[18] B. Aubert et al. Measurement of the branching fractions for $\psi(2s) \to e^+e^-$ and $\psi(2s) \to \mu^+\mu^-$. *Physical Review D*, 65:031101, 2001.

[19] D. Allspach et al. *Nuclear Instruments and Methods*, 410A:195, 1998.

[20] E. Hilger et al. Measurement of selected $\psi(3684)$ branching ratios from a study of secondary lepton pairs. *Physical Review Letters*, 35(10):625, 1975.

[21] G. Oleynik et al. *IEEE Trans. Nucl. Sci.*, 41:45, 1994.

[22] G. S. Abrams et al. Discovery of a second narrow resonance in e^+e^- annihilation. *Physical Review Letters*, 33:1453–1455, 1974.

[23] G. S. Abrams et al. Decay of $\psi(3684)$ into $\psi(3095)^*$. *Physical Review Letters*, 34(18):1181, 1975.

[24] J. E. Augustin et al. Discovery of a narrow resonance in e^+e^- annihilation. *Physical Review Letters*, 33:1406–1408, 1974.

[25] J. J. Aubert et al. Experimental observation of a heavy particle J. *Physical Review Letters*, 33:1404–1406, 1974.

[26] J. Z. Bai et al. A measurement of $\psi(2s)$ resonance parameters. *Physics Letters*, B550:24, 2002.

[27] K. Hagiwara et al. Particles and fields. *Physical Review D*, 66:1:730, 2002.

[28] M. Ambrogiani et al. *Nucl. Phys. Proc. Suppl.*, 61B:384, 1998.

[29] M. Ambrogiani et al. Measurement of the branching ratios $\psi' \to e^+e^-$, $\psi' \to J/\psi\pi^0\pi^0$ and $\psi' \to J/\psi\eta$. *Physical Review D*, 62:032004–1/8, 2000.

[30] M. Oreglia et al. Measurement of the decays $\psi' \to J/\psi\eta$ and $\psi' \to J/\psi\pi^0$. *Physical Review Letters*, 45(12):959, 1980.

[31] R. Brandelik et al. Results from dasp on e^+e^- annihilation between 3.1 and 5.2 gev. *Zeit. Phys.*, 1C:233, 1979.

[32] S. Bagnasco et al. *Nuclear Instruments and Methods*, 424A:304–320, 1999.

[33] T. A. Armstrong et al. Measurement of the J/ψ and ψ' resonance parameters in $p\overline{p}$ annihilation. *Physical Review D*, 47(3):772, 1993.

[34] T. A. Armstrong et al. Study of the $\eta_c(1^1S_0)$ state of charmonium formed in $\overline{p}p$ annihilations and a search for the $\eta_c'(2^1S_0)$. *Physical Review D*, 52(9):4839, 1995.

[35] T. A. Armstrong et al. Measurement of the branching ratios $\psi' \to e^+e^-$, $\psi' \to J/\psi\pi\pi$ and $\psi' \to J/\psi\eta$. *Physical Review D*, 55(3):1153, 1997.

[36] T. Appelquist et al. Spectroscopy of the new mesons. *Physical Review Letters*, 34:365, 1975.

[37] V. Lüth et al. Quantum numbers and decay widths of the $\psi'(3684)^*$. *Physical Review Letters*, 35(17):1124, 1975.

[38] W. Bartel et al. Cascade radiative decays of $\psi'(3684)$ and evidence for a new intermediate state of even c-parity. *Physics Letters*, 79B(4):492, 1978.

[39] W. Tanenbaum et al. Observation of the decay $\psi(3684) \to \psi(3095)\eta$. *Physical Review Letters*, 36(8):402, 1976.

[40] T. Armstrong et al. (Fermilab E760 Collaboration). Precision measurements of antiproton-proton forward elastic scattering parameters in the 3.7 to 6.2 gev/c region. *Physics Letters*, B385:479, 1996.

[41] Richard P. Feynman. Very high-energy collisions of hadrons. *Physical Review Letters*, 23:1415, 1969.

[42] Stephen Gasiorowicz and Jonathan L. Rosner. Hadron spectra and quarks. *American Journal of Physics*, 49:954, 1981.

[43] M. Claudson, S. Glashow and M. Wise. Isospin violation in J/ψ to baryon-antibaryon processes. *Physical Review D*, 25 (5):1345, 1982.

[44] Keith Gollwitzer. The CCAL shower Monte Carlo. E835 memo 312, U.C. Irvine, 1994.

[45] K. Gottfried. Hadronic transitions between quark-antiquark bound states. *Physical Review Letters*, 40(10):598, 1978.

[46] W. Greiner and J. Reinhardt. *Quantum Electrodynamics*. Springer Verlag, 1994.

[47] W. Greiner and A. Schaefer. *Quantum Chromodynamics*. Springer Verlag, 1995.

[48] David J. Gross and Frank Wilczek. Ultraviolet behavior of non-abelian gauge theories. *Physical Review Letters*, 30:1343, 1973.

[49] X. Zhang, H. Grotch and K.J. Sebastian. M1 decay rates of heavy quarkonia with a nonsingular potential. *Physical Review D*, 44(5):1606, 1991.

[50] Y.F. Gu and X.H. Li. *Physics Letters*, B449:361, 1999.

[51] S. N. Gupta. Nonsingular quarkonium potential. *Physical Review D*, 35(5):1736, 1987.

[52] W.R. Nelson, H. Hirayama and D.W.O. Rogers. The EGS4 Code System. Technical report, SLAC, 1985. SLAC-265.

[53] H.W. Huang and K.T. Chao. *Physical Review D*, 54:3065–6850, 1996.

[54] H.W. Huang and K.T. Chao. *Physical Review D*, 56:1821, 1997.

[55] J. Iizuka. *Suppl. Prog. Theor. Phys.*, 37:21, 1966.

[56] S.L. Glashow, J. Iliopoulos and L. Maiani. Weak interactions with lepton-hadron symmetry. *Physical Review D*, 2:1285, 1970.

[57] R. Karplus and A. Klein. *Phys. Rev.*, 87:848, 1952.

[58] K. Hagiwara, C.B. Kim and T. Yoshino. *Nucl. Phys.*, B177:461, 1981.

[59] T. A. Lähde and D. O. Riska. Pion rescattering in two-pion decay of heavy quarkonia. *Nucl. Phys.*, A693:755, 2001.

[60] T.A. Lähde. Exchange current operators and electromagnetic dipole transitions in heavy quarkonia. *Nucl. Phys.*, A714:183, 2003.

[61] P. Langacker and H. Pagels. Light-quark mass spectrum in quantum chromodynamics. *Physical Review D*, 19:2070, 1979.

[62] Giovanni Lasio and Michelle Stancari. Calibration of the Central Calorimeter in E835. E835 memo, University of California at Irvine, March 25, 2001.

[63] P.B. Mackenzie and G.P. Lepage. *Physical Review Letters*, 47:1244, 1981.

[64] R. McClary and N. Byers. Relativistic effects in heavy quarkonium spectroscopy. *Physical Review D*, 28(7):1692, 1983.

[65] P. Moxhay and J.L. Rosner. Relativistic corrections in quarkonium. *Physical Review D*, 28(5):1132, 1983.

[66] V.A. Novikov and M.A. Shifman. *Z. Phys.*, C8:43, 1981.

[67] M. M. Obertino. *Study of the decays of the state ${}^3P_0(\chi_{c0})$ of Charmonium: $\chi_{c0} \to J/\psi\gamma \to e^+e^-\gamma$; $\chi_{c0} \to \gamma\gamma$ for the experiment E835 at Fermilab.* PhD thesis, University of Torino, Italy, 2001.

[68] S. Okubo. *Physics Letters*, 5:165, 1963.

[69] H. Grotch, D.A. Owen and K.J. Sebastian. Relativistic corrections to radiative transitions and spectra of quarkonia. *Physical Review D*, 30(9):1924, 1984.

[70] Claudia Patrignani. J/ψ inclusive selection using the Electron Weight. E835 memo 395, University of Genova, 1997.

[71] Claudia Patrignani. *Physical Review D*, 64:034017, 2001.

[72] T. K. Pedlar. *A study of two photon decays of charmonium resonances formed in proton-antiproton annihilations.* PhD thesis, Northwestern University, June 1999.

[73] M. E. Peskin and D. V. Schroeder. *An introduction to quantum field theory.* Perseus Books, 1995.

[74] A. Petrelli. *Physics Letters*, B380:159, 1996.

[75] E. C. Poggio and H. J. Schnitzer. Hadronic corrections to the annihilation rate of heavy vector mesons to lepton pairs. *Physical Review D*, 20(5):1175, 1979.

[76] H. D. Politzer. Reliable perturbative results for strong interactions? *Physical Review Letters*, 30:1346, 1973.

[77] C. Quigg and J. Rosner. Quantum mechanics with applications to quarkonium. *Physics Reports*, 56:167, 1979.

[78] W. Kwong, C. Quigg and J. L. Rosner. Heavy quark systems. *Annu. Rev. Nucl. Part. Sci.*, 37:325–382, 1987.

[79] S. N. Gupta, W. W. Repko and C. J. Suchyta. Nonsingular potential model for heavy quarkonia. *Physical Review D*, 39(3):974, 1989.

[80] W. T. Eadie, D. Drijard, F. E. James, M. Roos and B. Sadoulet. *Statistical methods in experimental physics.* North-Holland, 1982.

[81] R. Van Royen and V. F. Weisskopf. *Nuovo Cimento*, 50:617, 1967.

[82] H. Georgi, A. De Rujula and S. L. Glashow. Hadron masses in a gauge theory. *Physical Review D*, 12:147, 1975.

[83] H. Grotch, K. J. Sebastian and F. L. Ridener Jr. Leptonic decay rates of charmonium S and D states. *Physical Review D*, 56(9):5885, 1997.

[84] A. J. Smith. *A study of select decays of J/ψ and ψ' states produced in antiproton-proton annihilations.* PhD thesis, U.C. Irvine, 1996.

[85] M.A. Shifman, A. Vanishtein and V. Zakharov. *Nucl. Phys.*, B147:385, 1979.

[86] M. Voloshin and V. Zakharov. Measuring quantum-chromodynamic anomalies in hadronic transitions between quarkonium states. *Physical Review Letters*, 45:688, 1980.

[87] Frank Wilczek. Quantum chromodynamics: the modern theory of strong interaction. *Ann. Rev. Nucl. Part. Sci.*, 32:177, 1982.

[88] J. F. Willemsen. The beginner's string. In M. C. Zipf, editor, *The Strong Interactions Vols I and II*, volume I of *Proc. Summer Inst. Part. Phys.*, page 445. SLAC Stanford Univ., 1974.

[89] Kenneth G. Wilson. Confinement of quarks. *Physical Review D*, 10:2445, 1974.

[90] G. Zweig. *CERN preprint 8182/TH401*, 1964.